Nanomagnetism and high frequency experiments. Basic science and technological applications

Víctor López Domínguez

Universitat de Barcelona

Nanomagnetism and high frequency experiments. Basic science and technological applications

Author: Víctor López Domínguez

Departament de Fisica Fonamental

Facultat de Física, Universitat de Barcelona

Doctorate Program:
Nanociències

Supervised by:
Javier Tejada Palacios

Tutor:
Javier Tejada Palacios

March, 2014

Contents

Resumen Castellano

La interacción de nanopartículas con radiaciones de alta frecuencia como las microondas o las ondas de terahercio son en la actualidad un campo de gran interés científico [1], [2] y tecnológico [3], [4], [5]. Por ejemplo algunos fenómenos y aplicaciones emergentes con nanopartículas magnéticas son la absorción de campos electromagnéticos (con frecuencias en la banda de las microondas) en circuitos electrónicos [6], o para la hipertermia magnética, además de otras aplicaciones médicas como el suministro de fármacos de manera local [7] o contraste en resonancias magnéticas [8]. Para estas aplicaciones es muy importante tener en cuenta los efectos de tamaño ya que modifican el comportamiento magnético de estos sistemas como su temperatura de bloqueo o de Curie. Estas propiedades tienen un papel muy importante en su interacción con radiaciones, como las microondas, ya que determinan la frecuencia máxima con la que se pueden acoplar al campo alterno o su frecuencia de resonancia, por ejemplo la resonancia ferromagnética. Como interesante avance en la unión de los campos de la electrónica, la medicina o la farmacia y las nanopartículas magnéticas, nos encontramos con materiales biocompatibles, como son las nanopartículas de oro [9], con un comportamiento de nanopartícula magnética a través de la modificación de su superficie mediante diferentes moléculas como los thioles y efectos de tamaño finito. Estos nuevos sistemas combinados con el potencial que presentan las radiaciones de microondas y teraherzio en medicina (son no invasivas y en el caso del teraherzio su sensibilidad con diferentes principios activos presentes en fármacos) , abren un interesante periodo de nuevos fenómenos científicos, técnicas experimentales y nuevas aplicaciones tecnológicas seguras, sin contacto y no invasivas.

Esta tesis versa sobre esta búsqueda de nuevos fenómenos en nanomagnetismo (ya sean por efectos de tamaño o por modificación superficial), su papel en la interacción de nanopartículas magnéticas con radiación de microondas, y nuevas aplicaciones tecnológicas y biotecnológicas basadas en la radiación de teraherzio. En este resumen se recoge los resultados más significativos durante los cuatro años que he pertenecido al Grup de Magnètisme i Microones de la Universtitat de Barcelona (UB), liderado por el Catedrático Javier Tejada. Los cuatro capítulos en los que esta tesis compuesta se pueden dividir en dos bloques fundamentales: el

primero, compuesto de tres capítulos, consiste en un exhaustivo estudio sobre sistemas de nanopartículas magnéticas; desde su caracterización estructural, química y magnética, a su dinámica magnética a altas frecuencias (microondas). En el segundo bloque (formado únicamente por el cuarto capítulo), se introduce la radiación de teraherzio y las distintas aplicaciones desarrolladas en los campos de ciencias de materiales, farmacia y medicina.

Debido a las temáticas expuestas, esta tesis puede ser descrita por las siguientes palabras claves: bajas temperaturas, nanomagnetismo, dinámica de spin, nanopartículas de oro, electromagnetismo, espectroscopia, farmacocinética, teraherzio y gigaherzio. Es importante mencionar que el desarrollo de esta tesis doctoral ha involucrado el uso de un amplio número de técnicas y metodologías experimentales para poder estudiar los distintos fenómenos físicos descritos a lo largo de este proyecto. A continuación se desarrollan los distintos capítulos.

Capitulo 1: Reducción colosal de la temperatura de Curie en nanopartículas de $CoFe_2O_4$

En el primer capítulo se exponen los fundamentos teóricos de los sistemas nanomagnéticos haciendo hincapié en la anisótropia magnética y el superparamagnetismo, conceptos también usados en los capítulos 2 y 3. Asimismo se introducen la interacción de intercambio responsable del ferromagnetismo, antiferromagnetismo y ferrimagnetismo, además del paramagnetismo atómico puro. Al final de la introducción también se introducen los fundamentos de las distintas técnicas de caracterización usadas en el primer bloque.

En el primer capítulo, todos estos conceptos se aplican en el estudio de tres muestras de nanopartículas de $CoFe_2O_4$ con una distribución bimodal de tamaños, centradas en 3 y 6 nm respectivamente. La caracterización química, estructural y magnética mostraron que las partículas de mayor tamaño presentaban el comportamiento esperado para este tipo de material: una temperatura de bloqueo entre 90 y 120 K, según la muestra. Sin embargo las partículas más pequeñas (menores de 3 nm) presentaban una deformación en su red cristalina, provocando una disminución de su temperatura de Curie (temperatura de transición entre un estado ordenado al paramagnetismo atómico) del 90 % (10 K) respecto al valor típico para el $CoFe_2O_4$. Este hecho fue confirmado a través de la medición de isotermas de la magnetización en función del campo aplicado. Para $T < 3$ K se observó un comportamiento puramente ferromagnético, mientras que en el intervalo 3 K$< T <$ 90 K, la magnetización en función del campo se corresponden con la suma de un paramagneto (partículas pequeñas) y otra ferromagnetica (partículas grandes).

En conclusión, por primera vez se ha observado una reducción de la temperatura de Curie del 90 % respecto a su valor nominal, 700 K para el caso del $CoFe_2O_4$, debido a efectos de tamaño. Además nos encontramos en el interesante caso donde

las temperaturas de bloqueo y de Curie de un sistema de nanopartículas son muy cercanas (13 y 10 K, en nuestro caso).

Capitulo 2: Dinámica de spin y resonancias magnéticas a frecuencias de microondas

En el segundo capítulo se explica los estudios de la dinámica de spin y la interacción con radiación de microondas de nanoparticulas de Fe_3O_4 y $La_{0,6}Sr_{0,3}MnO_3$, de 44 nm y 1 μm de tamaño medio de partícula, respectivamente. El interés en estos estudios reside en las diferentes aplicaciones tecnológicas que existen con partículas nanomagnéticas y su interacción con microondas: utilización en memorias magnéticas, hyperthermia o en capas aislantes para apantallar microondas. Además desde un punto de vista fundamental, los fenómenos resonantes cómo la resonancia ferromagnética, son de una gran importancia ya que son una manera eficiente de caracterizar materiales magnéticos. Una de las aportaciones más importantes en este capitulo reside en la utilización alternativa de lineas de transmisión coplanares para caracterizar la interacción de microondas en nanopartículas magnéticas. Este tipo de lineas no presentan fenómenos resonantes y son capaces de caracterizar el comportamiento de un conjunto de nanopartículas de manera rápida y eficaz.

En estos experimentos se observaron dos tipos de resonancias distintas, la resonancia ferromagnética, y una resonancia a campo cero para las partículas de magnetita y manganita. En el caso de las partículas de magnetita debido a su tamaño esta resonancia se asoció a la dinámica de spin de las partículas superparamagnéticas presentes en la distribución. En cambio, para las partículas de manganita esta interpretación no es posible, ya que debido a su tamaño no son monodominio. La interpretación más plausible para la resonancia a campo cero es el acoplamiento de las paredes de dominio con el campo alterno.

En resumen, en los dos casos fue posible detectar tanto resonancias ferromagnéticas de una manera simple y rápida, cómo la susceptibilidad ac de las dos muestras a frecuencias de Gigaherzio. Este estudio y metodología abre importantes futuras aplicaciones, cómo la capacidad de detectar partículas superparamagnéticas con una gran precisión, o otros fenómenos cómo el movimiento de paredes de dominio. Su relevancia tecnológica en poder codificar de una manera rápida, eficiente e inequívoca información, así cómo la aparición de futuras memorias magnéticas que pueden trabajar a velocidades de decenas de gigahercios, o en aplicaciones médicas, hacen de este estudio aun más prometedor.

Capitulo 3: Partículas de oro magnéticas

En este capítulo se exponen nuestros estudios sobre tres conjuntos de nanopartículas de oro sintetizadas en la presencia de precursores distintos (dos moléculas con las misma parte flexible pero distinta complejidad y la molécula TOAB), en el grupo del doctor Ron Ziolo en el Centro de Investigación Química de Mejico. La caracterización estructural de las partículas fue llevada acabo por el grupo del doctor Ziolo, mostrando que las partículas sintetizadas en la presencia de TOAB presentaban la distribución de tamaños más pequeña, 3,5 nm de tamaño medio. En los otros dos casos menor tamaño se consiguió un tamaño de partícula de 4 nm.

La caracterización magnética, llevada acabo en esta tesis, consistió en medir las curvas ZFC-FC, evolución de la remanencia magnética con la temperatura (TRM) y estudios de la magnetización en función del campo magnético a temperatura constante, 5, 100, 200 y 300 K. Los resultados mostraron para los tres casos un comportamiento de partículas ferromagnéticas (difiriendo sus propiedades según el tamaño de partícula y la molécula enlazada en la superficie), con una componente positiva e independiente a la temperatura. Esta contribución positiva a su susceptibilidad magnética es debida al paramagnétismo de Pauli, intrínseco de materiales conductores.

En conclusión el comportamiento magnético observado para cada uno del conjunto de partículas depende del tipo de molécula enlazada en la superficie. Todas estas propiedades descritas son muy interesantes para su aplicación en campos cómo la fotónica, células solares o aplicaciones biotecnologías debido a la unión de las propiedades magnéticas de estas nanopartículas (expuestas en los capítulos anteriores) y la ventaja de que el oro es un material biocompatible.

Capitulo 4: Radiación no invasiva de Teraherzio y su aplicación en la medida de la permeación de medicamentos de uso tópico.

En este capitulo se muestran a modo ilustrativo diferentes aplicaciones basadas en la radiación de terahercio en ciencia de materiales, seguridad y farmacia. Por ejemplo, en el ámbito de la espectroscopia se estudiaron las resonancias características en la banda de terahercio, de diferentes moléculas activas presente en formulaciones de uso tópico. De esta manera es posible determinar y caracterizar los distintos compuestos de forma inequívoca. Otras de las aplicaciones desarrolladas, a nivel espectroscópico, fue el diseño y detección de códigos de seguridad basado en antenas dipolares de longitud y ancho menor del milímetro. De esta manera se obtiene una miniaturización del código y a su vez un incremento de la seguridad ya que el código puede ir escondido detrás de tejidos u otros materiales dieléctricos (transparentes para frecuencias de terahercio).

Finalmente, la aplicación de la permeación de sustancias de uso tópico en piel (proceso de difusión) fue realizada usando la información que provee el tiempo de vuelo de la señal de teraherzio entre el emisor y la superficie de la muestra en la que incide. Para esta prueba de concepto se caracterizaron cuatro excipientes (base en forma liquida que transporta el principio activo) de uso común. Con estas sustancias se llevaron a cabo tres ensayos: permeación debido a 1) un gradiente de presión, 2) la existencia de un gradiente de concentración en membranas artificiales 3) existencia de un gradiente de concentración en muestras de piel humana. Los dos primeros ensayos sirvieron para testear y calibrar el sistema teniendo en cuenta los dos mecanismos que inducen el proceso de difusión: un gradiente de presión o concentración entre ambos lados de una membrana. El tercer ensayo consistió en la prueba de concepto in vitro sobre muestras reales de piel.

En los ensayos con membranas artificiales, tanto en la permeación causada por gradiente de presión cómo por gradiente de concentración, se obtuvieron los resultados típicos para dichos procesos de acuerdo con los descritos en la literatura. Por último en los ensayos con piel humana se obtuvo una curva de permeación del solvente esperable para dicho proceso. Sin embargo durante los primeros instantes del experimento se detecto un incremento global del sistema formado por el excipiente y la piel. Este resultado inesperado se interpretó cómo la saturación del estrato corneo por parte del solvente. Para demostrar este echo se repitió el experimento con una muestra de piel previamente saturada por el excipiente. En este caso se detecto otra vez esta fase de saturación pero menos prolongada en el tiempo.

En este último bloque hemos realizado nuevas aplicaciones tecnológicas en ámbitos cómo la seguridad, y aplicaciones biomedicas. Además de la demostración conceptual de la capacidad de la radiación de teraherzio para estudiar este tipo de problemáticas, hemos encontrado, nuevos resultados para la saturación de la piel durante el proceso de permeación, abriendo una nueva vía de investigación en todo estos campos.

Preface

The interaction among magnetic nanoparticles and high frequency radiations, such as microwaves and terahertz waves, is of a great interest on science [1], [2] and technology [3], [4], [5]. For example, magnetic nanoparticles can be used to screen electromagnetic fields in electronic circuits [6], or can be combined with radiofrequencies for medical applications such as magnetic hyperthermia, drug delivery [7] using microwaves or as a contrast in Nuclear Magnetic Imaging [8]. All these applications take into account size effects on magnetic nanoparticles because they modify the fundamental properties of the nanoparticles such as their blocking and Curie temperature. Furthermore, these properties are crucial in the interaction with electromagnetic radiation, for example the blocking temperature of a magnetic nanoparticle determines the maximum frequency that the magnetization of a magnetic nanoparticle can follow an oscillating magnetic field. Another interesting field of research is the study of new biocompatibles materials having magnetic properties by finite size effects, such as is the case of gold nanoparticles decorate with thiol groups or other molecules that are bond to the surface of the nanoparticle by a covalent bond [9]. These different systems of magnetic nanoparticles combined with the potential on medicine that represent microwave and the emerging terahertz technology opens the study of new scientific phenomena due to finite size effects or surface modification, and non-invasive and contactless technological applications in the inspection of materials or in medicine.

The main aims and results of this Thesis are related to this research of new phenomena in nanomagnetism and new terahertz technological and biotechnological applications in material sciences, pharmaceutical products, and biotechnology. This document is composed by the most relevant results during the four years I was working in the group of Magnetism and Microwaves of the University of Barcelona (UB), directed by Professor Tejada. The thesis is divided in two fundamental parts depending on the different objectives and materials. The first part is composed by the chapters 1, 2 and 3, and described in detail the study and characterization of very peculiar systems made of magnetic nanoparticles. The first chapter is dedicated to the colossal reduction of the Curie temperature due to finite size effects in $CoFe_2O_4$ nanoparticles, where an exhaustive structural, chemical, and magnetic

characterization was carried out. Chapter 2 expose the magnetization dynamics and resonance phenomena at microwaves frequencies in Fe_3O_4 and $La_{0.6}Sr_{0.3}MnO$ magnetic nanoparticles. Finally in chapter 3, it is discussed the magnetic behavior of magnetic gold nanoparticles when their surface is modified by different capping molecules.

The second part only consist in the fourth chapter, in which is presented the part of the electromagnetic spectra known as the terahertz band and its technological and biotechnological applications. Particularly the study of the permeation process of different topical excipients onto artificial membranes and human skin.

Based on the two parts that form this Phd thesis, it may be described by the following key words: nanomagnetism, low temperatures, spin dynamics, gold nanoparticles, topic drugs, electromganetism, microwaves, spectroscopy and terahertz radiation. Finally, the development of my Phd has involved a wide range of experimental techniques and methodologies in order to study the different physic phenomena described in this thesis.

Chapter 1

Colossal Reduction in the Curie Temperature of $CoFe_2O_4$ Nanoparticles

Magnetic nanoparticles are of great interest in many different fields of physics, chemistry and engineering due to their unique properties, which are due to the different interactions among atoms forming the particles, the exchange, the anisotropy energy, and the dipole-dipole force between particles. They also show magnetic relaxation phenomena [10] and quantum properties, such as under barrier quantum tunneling of the magnetization [11], [12], [13], [14]. At room temperature many technological applications can be found in fields such as data storage [11], [15], magnetic resonance imaging [16] , magnetic fluids [17], and biomedicine [16], [18]. Therefore, understanding the fundamental behavior of the magnetic properties of these nanoscale objects is very important.

Regarding the basis in magnetic nanoparticles, their total energy depends on the exchange interaction, the crystal field anisotropy, dipolar forces, and on the shape of the particle. In general, fully description of single domain particles is difficult because, for example, the exchange interactions at the surface are different from those in the bulk. In addition, the magnetic anisotropy at the surface differs from the anisotropy at bulk as a consequence of the different symmetry in the local arrangement of the atoms [10], [19]. For these reasons, magnetic properties of nanoparticles are very much influenced by finite-size and surface effects [20], producing a large variety of anomalous properties [21] , such as a reduction in the Curie temperature (or more general the order temperature) and the appearance of magnetic disorder on the surface of the particles.

An interesting new problem in single-domain particles is the study of their properties when the number of spins on the surface is of the order of the number of spins forming the core of the particle: it does not exist any clear answer to the

size dependence of the exchange energy of the particle, and how it affect to the Curie temperature.

Another important feature of magnetic nanoparticles is the control of their size and shape distributions because both the Curie temperature and the height of the anisotropy barriers are strongly affected by the shape and size of particles [20], [22]. Particularly, ferrite nanomaterials such as ferrimagnetic cobalt ferrite nanoparticles are of high interest due to their easy synthesis via chemical methods [23], [24], remarkable chemical stability, very high magnetocrystalline anisotropy, and moderate saturation magnetization.

In this chapter three interesting and novel systems made of magnetic cobalt ferrite nanoparticles will be described, presenting a colossal reduction in its Curie temperature due to finite-size effects. Moreover, we may enter in the very interesting regime of sizes, for which reduction in the value of the Curie temperature is such that the magnetic moment of the particle is blocked due to the magnetic anisotropy, with a blocking temperature similar to the Curie temperature.

The chapter is structured as follows: In the first section a theoretical background will be introduced, where the fundamental interactions in magnetic systems and magnetic nanoparticles (common for chapters 2 and 3) are described. Afterwards, $CoFe_2O_4$ nanoparticles will be presented. In the next two sections, the synthesis, the structure and chemical characterization of the particles will be described. In the central section of the chapter, the magnetic characterization, as well as the performed and obtained experiments are explained. At the end of the chapter all the conclusions will be summarized.

1.1. Introduction

In this section magnetic interactions are introduced as well as the existence of different magnetic order states. Because the system considered here present a phase transition at low temperatures, paramagnetism, and the ferromagnetic, antiferromagnetic and ferrimagnetic order states are presented first. Moreover, anisotropy energy will be discussed as well. Finally, the basis of the used experimental techniques will be described, which will also be used in chapters 2 and 3.

1.1.1. Magnetic order states

Pure paramagnetism is observed in systems where atoms or molecules have a non-zero spin and do not interact between them. For instance, an atom with a total momentum $\vec{J} = \vec{L} + \vec{S}$ (where $\vec{L}$ is the orbital angular momentum and $\vec{S}$ is the spin) in presence of a magnetic field $\vec{B}$ has $2J+1$ quantum states separated in

energy by $g\mu_B B$, with g being the Lande factor, and μ_B being the Bohr magneton. Using the partition function formalism for a canonical ensemble, the magnetization per volume unit of an ensemble of N spins is:

$$M = \frac{N}{V} g\mu_B \frac{\sum_{-J}^{J} -m_J e^{\frac{-g\mu_B m_J B}{k_B T}}}{\sum_{-J}^{J} e^{\frac{-g\mu_B m_J B}{k_B T}}} \tag{1.1}$$

where V is the volume of the ensemble, k_B is the Boltzman constant, m_J is the projection of the total angular momentum J on the z-axes, and T is the temperature. Defining $x \equiv \frac{g\mu_B B}{k_B T}$ and using the limit of moderate temperatures and low fields ($x \to 0$), equation 1.1 turns into:

$$M \simeq \frac{N}{V} g\mu_B \frac{\sum_{-J}^{J} -m\,(1 - mx)}{\sum_{-J}^{J} (1 - mx)} = \frac{N}{V} g\mu_B \frac{g\mu_B B J\,(J+1)}{3k_B T} \tag{1.2}$$

Hence the magnetic susceptibility is:

$$\chi = \frac{\mu_o M}{B} = \frac{\mu_o N^2 p^2 \mu_B^2}{3k_B T V} \tag{1.3}$$

being $p = g\sqrt{J\,(J+1)}$ the effective number of Bohr magnetons. The result on equation 1.1 is the known Curie law for paramagnetism : $\chi = \frac{C}{T}$, where C is the Curie constant that is defined as:

$$C \equiv \frac{\mu_o N p^2 \mu_B^2}{3k_B V} \tag{1.4}$$

In conclusion, the susceptibility of a paramagnetic system follows a $\frac{1}{T}$ law at low temperatures, shown in figure 1.1. Furthermore, many experiments revealed materials with susceptibilities that can be fitted to $\frac{C}{T-\theta}$ called the Curie-Weiss law; where θ is the Curie temperature of the material.

The general response to an external magnetic field, however, is given by the Brillouin function (figure 1.2) and all the different spins of the system tend to be aligned with the magnetic field. The general expression of the magnetization is represented by equation 1.5:

$$M = \frac{N}{V} g m_J \mu_B B_J\,(x) \tag{1.5}$$

with $x = \mu_o \mu_B g m_J \frac{H}{k_B T}$, and the Brillouin function $B_J\,(x) = \frac{2J+1}{J} \coth\left(\frac{2J+1}{2J} x\right) - \frac{1}{2J} \coth\left(\frac{x}{2J}\right)$, represented in figure 1.2.

Systems with interacting spins can be modeled by the exchange hamiltonian. This fact is based on the hydrogen molecule model, where the interaction between the electron spins is given by:

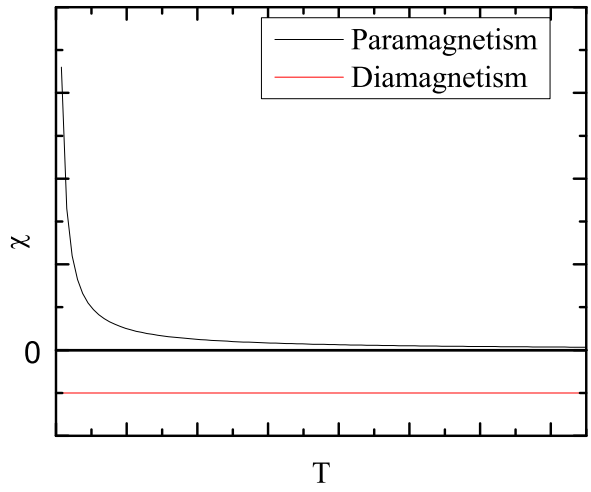

Figure 1.1: Dependence of the magnetization on temperature in the case of paramagnetism (where Curie law is observed) and diamagnetism (susceptibility being negative and constant with temperature.)

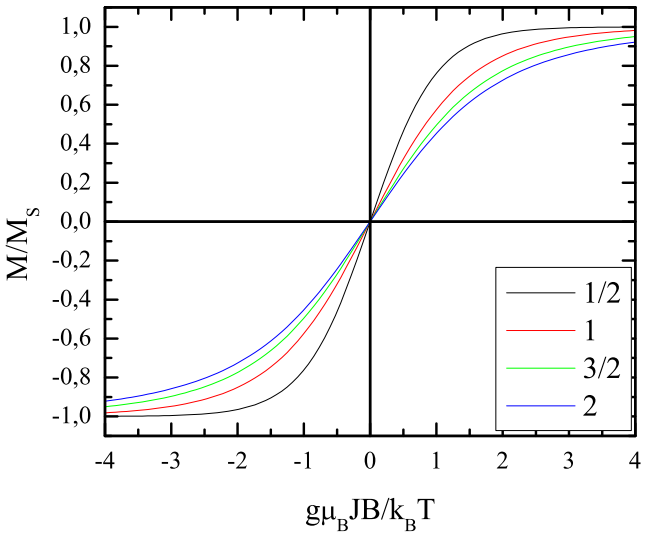

Figure 1.2: Brillouin functions for different spins value: 1/2, 1, 3/2, and 2.

$$-J\left(r\right)\vec{s_1}\cdot\vec{s_2} \tag{1.6}$$

where r is the distance between atoms, and $\vec{s}_1$ and $\vec{s}_2$ are the spins of both electrons. Equation 1.6 is called the exchange interaction and the constant J is the so called exchange constant. Taking into account equation 1.6 for a system of N atoms, the exchange hamiltonian for a ensemble of spins is:

$$H_{ex} = -\sum_{i<j} J\left(r_{ij}\right) \vec{s}_i \cdot \vec{s}_j \tag{1.7}$$

where $\vec{s}_i$ is the spin of the i-th atom, $J\left(r_{ij}\right)$ is the exchange constant for the i-th and j-th atoms, r_{ij} is the distance between them, and $i, j = 1, 2, ..., N$. Coefficients $J\left(r_{ij}\right)$ depend on the electrostatic forces and the overlap of the wave functions of electrons belonging to atoms i and j, represented in figure 1.3. Typically, some simplifications can be done in equation 1.7, for example, taking into account that the wave functions decreases exponentially with the distance between atoms, as represented in figure 1.3. Consequently, for many systems only the neighbor spins contribute to the exchange hamiltonian making the relevant terms to scale as N, that is the Heisenberg Hamiltonian:

$$H_H = -\sum_{\langle i<j \rangle} J_{ij} \vec{s}_i \cdot \vec{s}_j \tag{1.8}$$

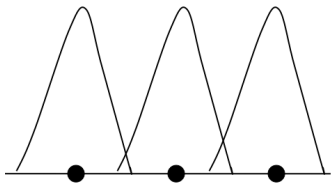

Figure 1.3: Overlap of the wave functions of magnetic electrons belonging to neighbor atoms.

being $J_{ij} = J_{ji}$ and $\langle ... \rangle$ means summation over the nearest neighbors only. Despite the simplifications in equation 1.8 respect equation 1.7, the computation of the exchange interaction is not easy. Therefore, it turns out that both positive and negative values of J_{ij} are possible, where their signs and absolute values determine the type of spin order as well as the temperature above that it disappears (it commonly know as the order temperature). Above the order temperature only individual magnetic atoms are observed: atomic paramagnetism. The value of the order temperature depends on the overlap of the electron wave functions; for

example, for large overlaps one can assume that this temperature may have the same order of magnitude as the melting temperature. In many materials, on the other hand, the temperature at which magnetic order disappears is much lower than the melting temperature, due to a small overlap of the electrons responsible for magnetism.

Besides, Heisenberg hamiltonian can explain the different type of order arrangements only taking into account the sign of J_{ij}, assuming that its value is constant in all the lattice positions. For classical spins, if the exchange constant is positive the energy that represents Heisenberg Hamiltonian is minimized by the parallel alignment of all spins, known as ferromagnetism (figure 1.4(a)). On the other hand, if the value of the exchange constant is negative, and only in the case of classical spins, the arrangement occurs in the antiparallel orientation, that is the antiferromangetism order (figure 1.4(b)). It is important remark that such antiferromagnetic arrangement can only be interpreted in a classical picture of spins, and, hence, it can be studied in terms of two uncompensated sublattices (spin-up and spin-down crystal sites). Nevertheless, in the case of quantum spin it is not possible to assign a spin direction to a lattice site. Consequently, the problem should be study using antiferromagnetic correlations along the crystallographic axis of the solid, with the absolute value of $\langle s_z \rangle$ at each site less than s, where s_z is the z-component of the spin.

Finally, a rather common type is ferrimagnetism shown in figure 1.4(c). In first approximation it can be studied in terms of two non-compensated ferromagnetic sublattices of unequal up and down spins.

1.1.2. Anisotropy energy

In general, nanomagnets or magnetic systems exhibits "easy" and "hard" directions of the magnetization [25]. The easy direction corresponds to the minimum of the energy when a magnetic field is not applied, and the hard direction to the maximum of the energy. Then, to magnetize the system in other direction than the easy one, it is necessary to apply a finite magnetic field. This phenomena is called magnetic anisotropy and relies upon, in solids, the orbital motion of electrons makes them feel a magnetic field $\vec{B} = \vec{v} \times \vec{E}\,(\vec{r})$, where $\vec{E}\,(\vec{r})$ is the local electric field inside the crystal. This magnetic field interacts with the spin of the electrons aligning their spins with the cristolographic axes of the solid. In fact, the exchange and the anisotropy are originated by the electrostatic crystal field, but the anisotropy has a relativistic origin proportional to $(v/c)^p$, where p is an arbitrary power. Consequently, the exchange interaction in magnetic systems is larger than anisotropy, but it is not invariant under rotations of spins.

The general form of the anisotropy Hamiltonian is in a tensorial form:

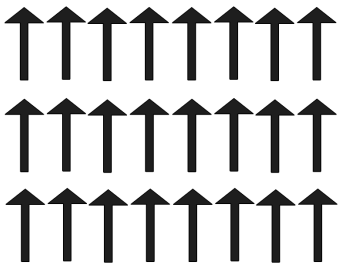

(a) Ferromagnetic arrangement.

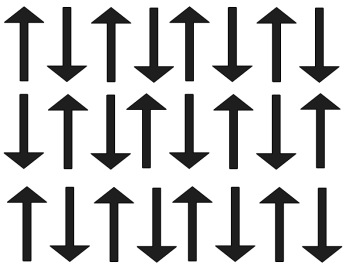

(b) Antiferromagnetic arrangement.

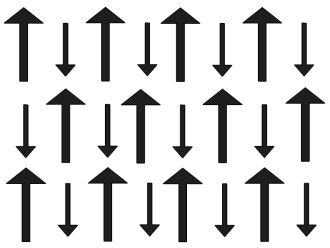

(c) Ferrimagnetic arrangement.

Figure 1.4: Different magnetic orders depending in the exchange interaction.

$$H_A = \frac{1}{2} b_{\alpha\beta} \sum_n S_{n\alpha} S_{n\beta} + \frac{1}{4} c_{\alpha\beta\gamma\delta} \sum_n S_{n\alpha} S_{n\beta} S_{n\gamma} S_{n\delta} + ... \tag{1.9}$$

where $b_{\alpha\beta}$, $c_{\alpha\beta\gamma\delta}$,... are tensors of the second rank, fourth rank, etc, and α, β, γ, $\delta = x, y, z$. Since the magnetic anisotropy has its origin in the spin-orbit interaction, equation 1.9 is a series expansion of the anisotropy energy in powers of $(v/c)^2$. Therefore, the terms of the second-, fourth- and so on, power on $\vec{S}_n$ have the the second, fourth,... order smallness on v/c respectively. Moreover, the use of even power in the magnetic anisotropy has its origin in the reversal of the spins at zero magnetic field, thus any state of the magnet has the same energy as the obtained reversing all the spins.

1.1.3. Magnetic nanoparticles

A macroscopic magnet breaks into different domains in order to reduce its magnetostatic energy due to the demagnetizing field present in the magnet, as seen in figure 1.1.3. Each domain is separated by domain walls, which are zones where the different spins rotate from one domain to the next, and changing the orientation of the different spins. The domain wall thickness is given by $\delta \sim (J/D)^{\frac{1}{2}} a$, where Js^2 and Ds^2 are the exchange and anisotropy energies respectively (where the form Ds^2 refers to an uniaxial magnetic anisotropy), and a is the lattice spacing. Then

the formation of a domain wall is a balance between the exchange energy and the anisotropy energy of the system. For example a nanoparticle of spherical shape that has a radius $R > \delta$, the formation of domains is possible, but if the radius verifies the relation $R < \delta$, the particle becomes single domain (the formation of the domain wall is not possible). In the monodomain case, the magnetization of the particle is represented by a unique macrospin, composed of the sum of all the spins forming the nanoparticle. Since typical values of the order temperature are of several hundred of Kelvins, rotation of the macrospin is carried out by coherent uniform rotation of all the spins forming the particle [25].

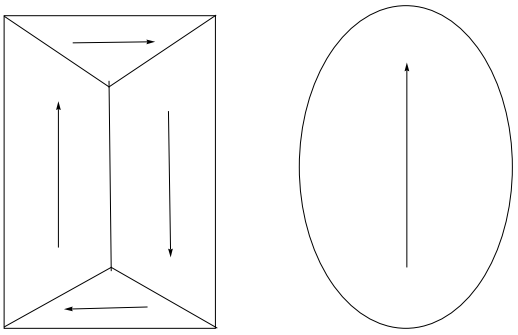

(a) Magnetic domains.

(b) Monodomain particles

Figure 1.5: a) Different distribution of magnetic domains in a magnet. Lines represent the different magnetic walls that separates each domain. b) Monodomain particle. As the size of the particle is smaller than the domain wall the formation of domains is not possible.

1.1.4. Superparamagnetism

For single domain particles with large spins (higher than 100), and for a classical spin description the anisotropy energy of a nanoparticle can be represented as (in the case of a uniaxial anisotropy):

$$E_A = -KV \sin^2 \theta \tag{1.10}$$

where K is the anisotropy constant of the material, V is the volume of the particle, and θ is the angle between the magnetization of the particle and the easy axis. In this case, representing the energy of the particle as a function of θ, a continuous barrier energy is obtained, which depends on the orientation of the spin along the easy axis (figure 1.6). In fact, in the absence of resonant tunnel effect [11], the system can only overcome the barrier via thermal activation, characterized by the thermal energy, $E_T \propto k_B T$, k_B being the Boltzman constant and T the

temperature. To compute the total magnetization for an ensemble of identical particles (same volume), with easy axes parallel to the z-axis, and for a magnetic field $\vec{H} = H\widehat{e_z}$, one can define the two magnetic states parallel and antiparallel to the field as M_+ and M_-. The time rate transition of the two states are given by:

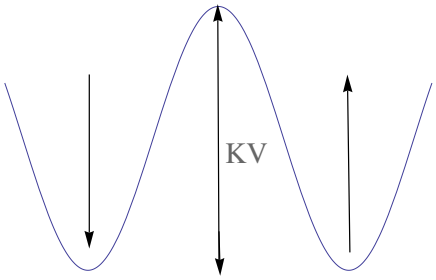

Figure 1.6: Energy barrier as a function of the angle θ between the easy axis and the magnetization. There are two equilibrium position along the easy axes and one unestable position perpendicular to the axis.

$$\frac{dM_+}{dt} = -\Gamma_+ M_+ + \Gamma_- M_- \tag{1.11}$$

$$\frac{dM_-}{dt} = -\Gamma_- M_- + \Gamma_+ M_+ \tag{1.12}$$

being Γ_+ and Γ_- the frequency to transit to the state M_+ and M_-, respectively. Consequently, this process is a relaxation problem through an energy barrier, defined by the anisotropy energy, to a stable state. These transitions can only be originated by thermal effects, and thus, at finite temperatures T, the probability frequency of the spin to overcome the energy barrier follows the Arrhenius law:

$$\Gamma_\pm = \Gamma_{o\pm} e^{\frac{KV}{k_B T}} \tag{1.13}$$

With equation 1.13 we can define a relaxation time as:

$$\tau_= \frac{1}{\Gamma} = \tau_o e^{-\frac{KV}{k_B T}} \tag{1.14}$$

being τ_o the attempt time a constant of the system, known as the attempt time, and τ is the time that takes for the nanoparticle's magnetization to randomly flip (overcome the barrier) as a result of thermal fluctuations. As seen in equation 1.14, the relaxation time depends on the high of the barrier and the temperature: for high temperatures the thermal fluctuations diminishes the relaxation time to overcome the barrier. On the other hand, for large particles (larger volume) the energy barrier is higher than for smaller particles, and hence the attempt time to

overcome the barrier is larger than for smaller particles of the same material. This fact will be explored in the next chapters.

Defining the total magnetization as the sum of states M_+ and M_-, $M = M_+ - M_-$ and using equations 1.11 and 1.12, the total magnetization is expressed as:

$$M(t) = M_{eq} + (M_o - M_{eq})\, e^{-\Gamma t} \tag{1.15}$$

where $M_{eq} = \frac{\Gamma_- - \Gamma_+}{\Gamma_- + \Gamma_+} M_s$ is the equilibrium moment, $M_s = M_+ + M_-$ is the the total magnetization at saturation, $M_o = M(t=0)$, and $\Gamma = \Gamma_- + \Gamma_+$.

Equation 1.15 only consider identical particles, as counterpart, for a system of uniformly oriented non-interacting uniaxial particles with the same magnetization and anisotropy energy per unit volume, but with a distribution of volumes $f(V)$, equation 1.16 turns into:

$$M(t) = M_o - [M_o - M_{eq}] \frac{\int_o^{V_B} dV f(V)}{\int_o^{\infty} dV f(V) V} \tag{1.16}$$

In equation 1.16 it was introduced the dependence of the thermal relaxation on the size distribution. In addition, it was introduced the blocking volume in the numerator integral, V_B (it depicted in equation 1.17), that is a maximum particle volume that can flip its magnetic moment at the temperature, T. In general the integral takes the following form: $\int_0^{\infty} dV f(_V) V \exp(-\Gamma(V) t)$. Since typical values of νt are between $10^{11} - 10^{15}$, the exponential part can be approximated by a Heaviside function, $\Theta(V - V_B)$, and the limits of the integral become: $\int_{V_B}^{\infty} = \int_0^{\infty} - \int_0^{V_B}$, obtaining the result depicted by equation 1.16.

$$V_B = \frac{k_B T}{K} \ln(\nu t) \tag{1.17}$$

Consequently, in the ensemble described by a size distribution, only particles with volumes $V_B(t)$, at time t, contribute to the relaxation: smaller particles have already relaxed, whereas bigger particles have their moments blocked in the initial orientation.

In the general case, for which there is a random distribution of easy axis, equation 1.16 remain valid, only if the applied field is smaller than the anisotropy field (it explained at the end of this section), which is the typical situation. If this requirement is not accomplish, then the total moment of the ensemble depends on the orientation of the particles respect to the field, as well as the transition rates. Furthermore, if the product $f(V) V$ drops rapidly above a certain value V_o, namely the mean volume of the distribution, one can characterize the system in terms of the blocking temperature:

$$T_B = \frac{KV_o}{k_B \ln(\nu t)} \tag{1.18}$$

where t is the characteristic measurement time of the instrument. Because condition $T << T_B$ is mathematically equivalent to the condition $V_B << V$, the physical meaning of the blocking temperature is: if the thermal energy is lower than the energy barrier ($T < T_B$), the system can not flip the spin overcoming the barrier, and the particle remains with its spin blocked (blocked state). However, if the thermal energy is bigger than the barrier height ($T >> T_B$), the system can flip the spin through the barrier, that is the spin can change between the parallel and anti-parallel states. In the later case, the particles align its magnetic moment directly with any field, behaving like a paramagnet with a large susceptibilty. This latest case is known as superparamagnetism and its response to a magnetic field follows a Langevin function:

$$L(x) = \coth(x) - \frac{1}{x} \tag{1.19}$$

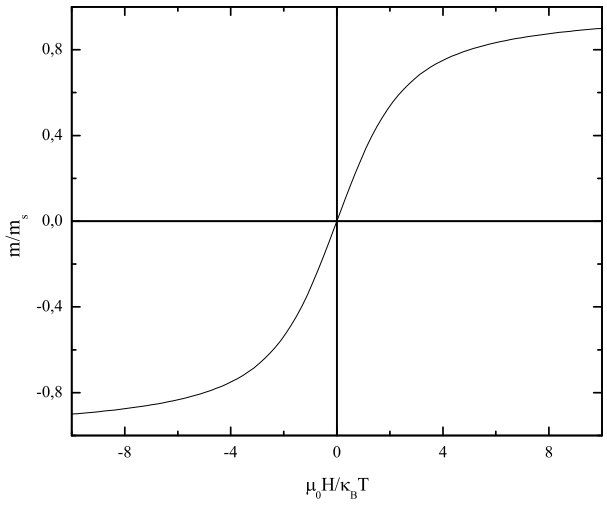

Figure 1.7: Langevin function.

Using equation 1.19, the magnetization of the nanoparticle in the superparamagnetic state is $M = M_S L(x)$, with $x = \mu_o g \mu_B JH/k_B T$. In addition at low and constant fields, the magnetization follows a $\frac{1}{T}$ law when the system becomes superparamagnetic: that is above the blocking state.

As mentioned above, the blocking temperature not only depends on the energy barrier but on experimental window time as well. If the time that needs the system to flip the spin orientation is τ (it described by equation 1.14), and τ_m the experimental measurement time, there exist three different cases:

- $\tau_m < \tau$ the time spend for the particle to reverse its spin is larger than the time we spend to measure its magnetization, thus the magnetization that we will measure is frozen and the nanoparticle is in the blocked state.

- $\tau_m = \tau$ is the limit case when the thermal energy equals the height of the anisotropy barrier, at the blocking temperature, defined by equation 1.18.

- $\tau_m > \tau$ the spin of the particle overcome the barrier many times during the whole time window measurement. That is the magnetization flips several times and its average becomes zero. Hence the system is in the super paramagnetic state.

For example a SQUID system spends 1 s for a measurement, taking into account that for typical nanoparticles the attempt time is between 10^{-10} s and 10^{-12} s, the value of $\ln\left(\frac{\tau_o}{\tau_m}\right)$ about 30. Then for a SQUID equipment the blocking temperature is defined as $T_B = \frac{KV}{30k_B}$. On the other hand, Mössbauer spectroscopy has a measurement time in the order of a few nanoseconds and T_B will be significantly larger than in the case of SQUID measurements.

Returning to equation 1.16, the thermal relaxation of the magnetization depends on time only through the combination $T\ln(\nu t)$, based on the size distribution $f(V)$ changes slower than exponentially in the vicinity of V_B. That is the case for typical statistical distributions, such as the Gaussian, Maxwellian, and exponential ones, but this assumption becomes correct only for $V_B \ll V_o$. Thus, the $\ln(t)$ relaxation should be expected at $T \ll T_B$ but must finish at $T \simeq T_B$. In the case of non-interacting particles and in the approximation of small fields, the definition of the magnetic viscosity, which is independent from the initial and final state, is:

$$S = -\frac{1}{M_o - M_{eq}}\frac{dM}{d\ln(t)} = \frac{T}{K < V >}\frac{V_B f(V_B)}{\int_0^\infty dV f(V)} \tag{1.20}$$

where $< V >= \int_0^\infty dV f(V) V / \int_0^\infty dV f(V)$. In general the magnetic viscosity, S, must depend logarithmically on time and, alternatively one may extract the distribution function from relaxation measurements.

Finally, in general the effect of a magnetic field in the energy barrier is to reduce its height (it defined as $U = KV$ at zero field):

$$U = KV\left(1 - \frac{H}{H_K}\right)^2 \tag{1.21}$$

where H_K is the anisotropy field.

1.1.5. The zero-field-cooled magnetization curve

In the next section we remind the most important measurement techniques in magnetic nanoparticles and will be used in the following chapters: the zero-field-cooled (ZFC) Field-cooled (FC) curves, Thermal Remanent Magnetization (TRM), and ac-susceptibilty, where ZFC-FC curves will be reviewed first.

Let us consider a system of small particles with a volume distribution $f(V)$ cooled to a very low temperature (for example 2 K) at zero magnetic field. The moments of the particles will be oriented randomly with total magnetization being zero (the sum of the individual magnetization for each particle). The ZFC curve consists of applying a small field $H \ll H_k$ to study the temperature dependence of the magnetization, as the ensemble of particles is warming. Only particles of a volume smaller than the blocking volume contribute to the net magnetization, or in other words those superparamagnetic particles can align their magnetic moment along the field at given temperature T.

Introducing the distribution function $f(V)$, and taking into account the normalization condition $\int_0^\infty dV f(V) = N$, we obtain for the total ZFC moment:

$$M_{ZFC}(T, H, t) = \frac{m_S^2 H}{2T} \int_0^{V_B(T,t)} dV f(V) V^2 \tag{1.22}$$

where the factor $\frac{1}{2}$ came from taking the average over the angle. When all the particles become superparamagnetic (for $T > T_B$ that is the same that $V_B > V$) the integral becomes constant in equation **??**, and, then M_{ZFC} is proportional to $1/T$ (all the particles are in the superparamagnetic state). On the other hand, for $T \ll T_B$ (or $V_B \ll V_o$), the integral is not constant and then the magnetization of the ensemble depends on the size distribution. Despite this fact, it can be demonstrated [13] that $M \propto T^{2+n}$ for those distribution functions proportional to V^n. Therefore, for $n \geq -2$ the ZFC magnetization grows with T. In this text, the studied size distributions of particles verifies the condition mentioned above, exhibiting an increase in the ZFC magnetization until T_B, followed by a decrease according to Curie law above T_B.

Finally, the conventional experimental definition of the blocking temperature is the temperature at which the ZFC magnetization curve goes through the maximum. Consequently, from equation 1.22 is obtained that T_B satisfies:

$$V_B \frac{df}{dV_B} + 2f\left(V_B\right) = 0 \tag{1.23}$$

For example, for a size distribution $f = \exp\left(-V/V_o\right)$ the experimental T_B is $2KV_o/\ln\left(\nu t\right)$, whereas for $f = exp\left(-V^2/V_o^2\right)$ is $KV_o/\ln\left(\nu t\right)$. Consequently the ZFC magnetization data provide information of the size distribution of the particles and its blocking temperature.

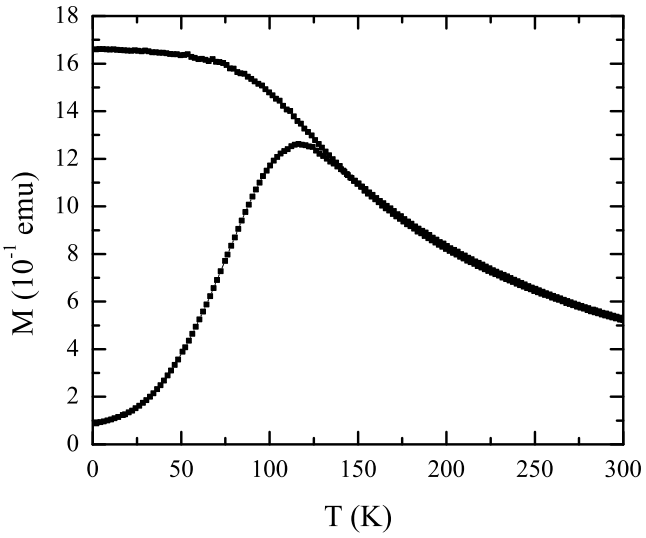

Figure 1.8: ZFC-FC for $CoFe_2O_4$ particles. The ZFC shows how nanoparticles start to be unblocked until they reach a maxima (higher barrier energy in the system). In the FC curve the particles still frozen along the field below the blocking temperature.

On the other hand, Field cooled process represents the stable magnetization curve of an ensemble of particles. In this case, the particles are cooled down to a very low temperature, such as the ZFC case, but with a low applied magnetic field ($H << H_k$). As seen in figure 1.8,, below the blocking temperature the total magnetization of the ensemble is saturated or frozen in the direction of the field. Above the blocking temperature is observed the usual $1/T$ law, of which the particles are in the superparamagnetic state. The FC magnetization can be computed as:

$$M_{FC}\left(T,H,t\right) = \frac{m_S^2 H}{2T}\int_0^{V_B(T,t)} dV f\left(V\right)V^2 + \frac{m_S^2 H}{2T}\int_{V_B(T,t)}^{\infty} dV f\left(V\right)V^2 \tag{1.24}$$

where the left term corresponds to the unblocked particles and the right term to the blocked ones. It is important to take into account the blocked particles

because in this case they contribute to the total moment with the state that they were frozen. As final remark, the ZFC and FC magnetization data accomplish the following equation:

$$\frac{d\left(M_{FC}-M_{ZFC}\right)}{dT} \propto f\left(V\right) \tag{1.25}$$

1.1.6. Thermal Remanent Magnetization: TRM

In the previous section it was discussed how the ZFC data can be analyzed to obtain the distribution function and/or the blocking temperature. Another interesting and useful experimental method is the Thermal Remanent Magnetization measurement (TRM, developed by Sappey [26]). The main idea of a TRM measurement is to obtain the size distribution through ZFC-FC measurements, but taking into account the effect of the magnetic field on the energy barriers.

Like in the ZFC-FC case, we consider an ensemble of particles cooled down to a very low temperatures, but with a applied magnetic field (in the case of the ZFC the sample is cooled without a field). Then the field is removed and the measurements are carried out. Let $f\left(V\right)$ be the size distribution of the ensemble, hence the TRM magnetization is expressed as:

$$M\left(T\right) = \frac{M_S^2}{3k_B} H \int_{V_B(T,0)}^{\infty} dV \frac{f\left(V\right) V^2}{T_B\left(V,H\right)} \tag{1.26}$$

where V_B is the blocking volume as a function of the temperature. Remarkably the derivative of TRM magnetization as a function of temperature provides the quantity $Vf\left(V\right)$ that, for example, in the case of a log-normal its maximum is V_o, that is the mean volume of the distribution $f\left(V\right)$. Consequently, with this method it is possible to deduce the mean volume of the distribution, V_o, with a direct measurement. Furthermore, the derivative of the TRM magnetization is:

$$\frac{\partial M_{TRM}}{\partial T} = -\frac{M_S^2 k_B H}{3K^2} \frac{\ln^2\left(t_m/\tau_o\right)}{\left(1-H/H_a\right)^2} V_B\left(T,0\right) f\left(V_B,0\right) \tag{1.27}$$

where α depends on the orientation of the particles along the magnetic field, and typical measured TRM for $CoFe_2O_4$ nanoparticles and its derivative are represented in figure 1.9. As important fact, equation 1.27 does not have any contribution about the barrier modulation as a function of the field. For this reason, there exist another measurement protocol know as R-TRM. It consists of cooling down the system with an applied field, $+H$, and then measuring the magnetization increasing the temperature with a $-H$ applied field. If one sums the FC magnetization to the R-TRM magnetization an computes its derivative, the result is:

$$\frac{\partial\left(M_{R-TRM}+M_{FC}\right)}{\partial T}=-2\frac{M_S^2 K k_B \ln^2\left(t_m/\tau_o\right)}{3K^2\left(1-H/H_a\right)^{2\alpha}}V_B\left(T,H\right)f\left(V_B\left(T,H\right)\right) \quad (1.28)$$

As it is observed, the blocking volume in equation 1.28 corresponds to the blocking at different temperatures and fields. Therefore, it is possible estimate the influence of the field on the energy barrier at different fields. Finally the magnezitation of the ZFC-FC and R-TRM processes are related between them by:

$$M_{ZFC}=\frac{1}{2}\left(M_{FC}-M_{R-TRM}\right) \quad (1.29)$$

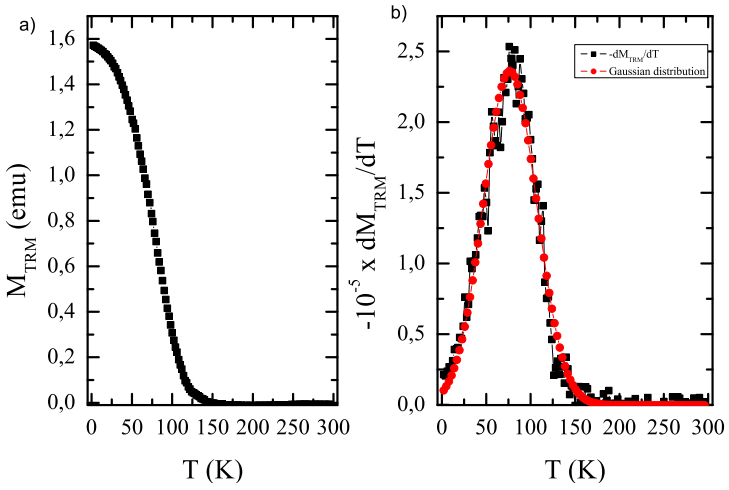

Figure 1.9: a)Measured TRM and b)its derivate for typical $CoFe_2O_4$ particles. The derivative fits to a gaussian distribution function.

1.1.7. AC susceptibility

The dependence of the blocking temperature on the measurement time originates different experimental approaches in order to study the different properties of the distribution of energies barriers, such as the ZFC-FC, TRM, R-TRM and the ac-susceptibility. In this last case we consider a system of identical non-interacting particles whose total magnetization is relaxing and satisfied the relaxation equation in absence of a field, $\tau\left(dM/dt\right)+M=0$, where τ is the single relaxation time. On the other hand, in the presence of an oscillating weak magnetic field, $h=h_o\cos\omega t$ the magnetic response of the system is $M\left(t\right)=\chi_o h_o\cos\left(\omega t\right)$. Therefore, in the presence of both relaxation and an AC field the following equation is found:

$$\tau\frac{dM}{dt} + M = \chi_o h_o \cos(\omega t) \tag{1.30}$$

And the solution of equation 1.30 can be written as:

$$M = \chi' h_o \cos(\omega t) + \chi'' h_o \sin(\omega t) \tag{1.31}$$

being χ' and χ'' the in-phase and out-phase susceptibilities correspondingly.

$$\chi' = \chi_o \frac{1}{1+(\omega\tau)^2}$$

$$\chi'' = \chi_o \frac{\omega\tau}{1+(\omega\tau)^2} \tag{1.32}$$

As counterpart, in the case of non-identical particles, which are represented by a size distribution $f(V)$, equations 1.32 become:

$$\chi' = \frac{\chi_o}{V_t}\int_0^\infty dV \frac{f(V)V}{1+[\omega\tau(V)]^2}$$

$$\chi'' = \frac{\chi_o}{V_t}\int_0^\infty dV \frac{f(V)V\omega\tau(V)}{1+[\omega\tau(V)]^2} \tag{1.33}$$

Typical results for $CoFe_2O_4$ nanoparticles in the presence of oscillating fields are represented in figure 1.10. Similarly the ZFC-FC case, one can define a blocking volume $V_B = (Tk_B/K)\ln(\nu/\omega)$ that combined with the definition in equations 1.32, the in-phase component of the magnetic susceptibility becomes:

$$\chi' = \chi_o \frac{\int_0^{V_B} dV f(V)V}{\int_0^\infty dV f(V)V} \tag{1.34}$$

and in the case of χ'', it can be approximated as:

$$\chi'' = \frac{\chi_0 V_B f(V_B)\int_0^\infty dV\omega\tau(V)[1+(\omega\tau(V))]^{-1}}{\int_0^\infty dV f(V)V} = \frac{\pi}{2}\chi_o\frac{k_BT}{K}\frac{V_B f(V_B)}{\int_0^\infty dV f(V)V} \tag{1.35}$$

where we use the explicit form of $\tau(V)$ to integrate the numerator over V. As it is observed in equation 1.35, there exist the following relation between χ' and χ'':

$$\chi'' = -\frac{\pi}{2}\frac{\partial\chi'}{\partial\ln(\omega)} \tag{1.36}$$

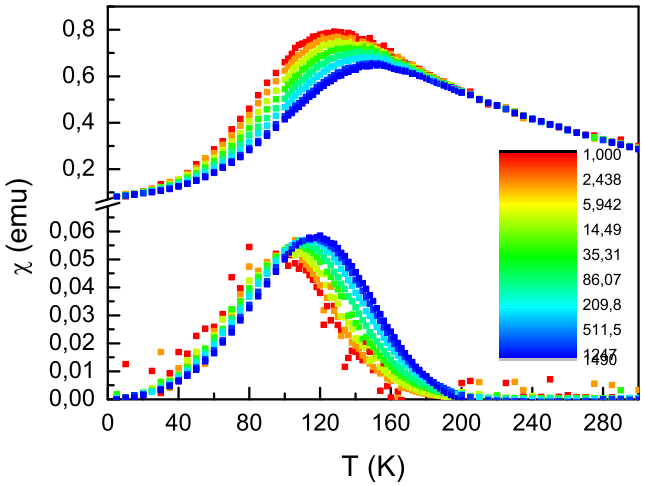

Figure 1.10: AC-susceptibility for $CoFe_2O_4$ nanoparticles. The blocking temperature depends on the logarithm of the frequency of the ac-magnetic field.

In equation 1.36 it is observed that χ' should depend on the temperature and frequency by the combination of $T \ln(\tau/\omega)$, such as ZFC measurements. If the period of the AC field has the order of magnitude of the DC relaxation time, the out-of-phase susceptibility and the viscosity are connected by:

$$\chi'' = \frac{\pi}{2}\chi_o S \tag{1.37}$$

Therefore ac-measurements are another experimental approach to observe how far is the system from thermal equilibrium and the different parameters related to its size and energy barries distributions. As final remark it is also related to the measurement of the magnetic viscosity.

1.2. $CoFe_2O_4$ Nanoparticles

Oxidic spinels have been of great interest in science and technological applications, because of their special electrical and magnetic properties [27], [28]. In the technological field, these kind of materials are used in high frequency devices, and magnetic record media.

Ferrite spinels consist of a close-packed face centered cubic lattice of O^{2-} assisted by interstitial cationics sites, namely tethaedral or octhaedral sites. The physical properties of these kind of materials depend not only on the type of cation but also on the cationic distribution.

Their magnetic properties stem from the presence of two different magnetic sublattices, originated by the exchange interaction between the magnetic moments in tethaedral sites (A) and octhaedral sites (B). It is possible to create different compounds for oxidic spinels, of the type $T_xFe_{3-x}O_4$, being T ions such as Cu^{+2}, Co^{+2}, Mg^{+2}, Ni^{+2}... Moreover, in some cases such as $CoFe_2O_4$, the strong exchange interaction generates a ferrimagnetic order inside the material.

Finally systems such as $CoFe_2O_4$ present an order temperature of about 700 K, and as anisotropy constant of $K = 2 \cdot 10^6 erg/cm^3$ resulting in a blocking temperature for ultrafine particles, e.g. 5 nm, of about 52 K. Therefore, in the nanoscience and nanotechnology size region ($1 - 100$ nm), $CoFe_2O_4$ should only present the phenomenology related to magnetic nanoparticles, that is, monodomain particles with an anisotropy energy barrier.

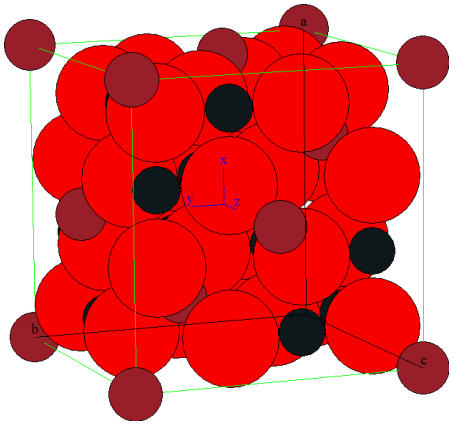

Figure 1.11: Inverse spinel unit cell for bulk $CoFe_2O_4$. Dark red points represent oxygen atoms, red points iron atoms, and black points cobalt atoms.

1.3. Synthesis of $CoFe_2O_4$

The synthesis of our cobalt ferrite particles was carried out via the decomposition of stoichiometric quantities of Fe(acetylacetonate)$_3$ and Co(acetylacetonate)$_2$ (from now on we will say acetylacetonate as acac) in high-boiling-point solvents, diphenyl and dibenzyl ether. Three different sets of cobalt ferrite nanoparticles were prepared to obtain characterizable size distributions of the nanoparticles following two consecutive and separate stages of nucleation and growth, correspondingly.

Co(acac)2 (1 $mmol$), Fe(acac)3 (2 $mmol$), 1,2-hexadecanediol (10 $mmol$), oleic acid (6 $mmol$), oleylamine (6 $mmol$), and benzyl ether (20 mL) were mixed and magnetically stirred under nitrogen. The mixture was heated to 200 ^oC for 2

hours, and then, under a blanket of nitrogen, heated to reflux (290 ^oC) for 1 hour. The black-colored mixture was cooled down to room temperature by removing the heat source. Under ambient conditions, ethanol was added to the mixture and black material was precipitated and separated via centrifugation. The obtained black product was dispersed in hexane and then re-flocculated by adding ethanol, followed by centrifugation. Several washings with hexane/ethanol were performed in order to remove any byproducts.

The capping of the oleic acid actuated as a stabilizer of the particle and prevented their aggregation. The three different sets of particles were characterized structurally, stoichiometricly, and magnetically, in order to study their physical properties.

1.4. Structural Characterization

To confirm the composition, the size and the shape of cobalt ferrite particles Energy-dispersive X-ray Spectroscopy (EDX, as a local stoichiometry probe), Xray Diffraction (XRD), and Transmission Electron Microscopy (TEM) was used. The obtained EDX spectrum is shown in figure 1.12, which showed the presence of cobalt and iron in an approximate 1:2 ratio, as expected for $CoFe_2O_4$. For clarity, we omit the presence of oxygen and carbon peaks (found in the composition of the particles and the oleic acid).

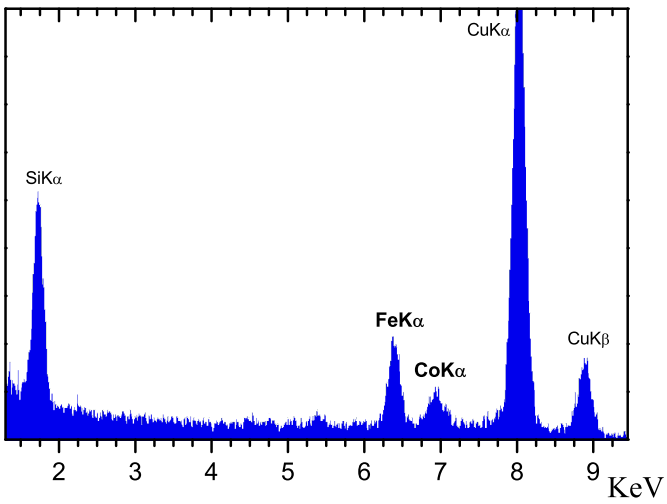

Figure 1.12: EDX spectra for one of the prepared samples. The data show the presence of cobalt and iron in 1:2 ratio. The other peaks are associated with the used grid and the X-Ray source.

Particle morphology, shape and size distribution of the three samples were examined by a JEOL JEM 2100 transmission electron microscope. The samples were prepared by drying a hexane dispersion of the particles on amorphous carbon-coated copper grids and their TEM images are shown in figure 1.4. The mean particle size and distribution were evaluated by measuring the largest dimension of at least 100 particles, for each sample. The result for the particle size histogram, shown in figure 2.2, demonstrated the presence of a bimodal size distribution of particles, for each sample. The distributions were fitted as the sum of two log-normal distributions (see equation 1.38) obtaining for each sample : mean diameters of $4.5 \pm 0.5\ nm$ in sample A, $6.7 \pm 0.6\ nm$ in sample B and $5.4 \pm 0.5\ nm$ in sample C, for large particles; and the other one with $2.01 \pm 0.1\ nm$ for sample A, 2.0 ± 0.4 for sample B, and $2.6 \pm 0.3\ nm$ for sample C mean diameter, for the smaller particles.

$$f(v) = \frac{1}{\sqrt{2\pi}\sigma V} \exp\left[-\frac{\ln^2(V/V_o)}{2\sigma^2}\right] \tag{1.38}$$

With the TEM images was also possible to compute the spacing between the atomic planes of the family (311), d_{311} (it was the peak with highest intensity in the X-Ray spectra for all the analyzed particles, see figure 1.15). The distance was calculated selecting only each particle in the image, then the Fourier Transform was done for the selected area, and the distance between the diffraction peaks was measured. In figure 1.16 the distances corresponding to the (311) family of planes are plotted, as a function of particle's sizes (in this text it is only shown the interatomic space for Sample C). A clear variation of the distance between the atomics planes with the size of the particle existed, with an increase of nearly 20 % when the size of the particle decreased form 5 to 3 nm. In the case of largest particles, the spacing coincided with the interatomic distance expected for bulk cobalt ferrite.

To study the crystallographic structure of the samples, X-ray diffraction (figure 1.17, from now on in this text only the results of sample C are shown) was carried out using Cu kα radiation ($\lambda = 1.5408\ nm$). The spectrum showed the presence of only two broad peaks at positions that corresponded to the most intense peaks for bulk $CoFe_2O_4$. The width of the peak was big enough to smear out the contribution of the weakest peaks in the spectrum and was compatible with the existence of very small nanoparticles.

Remarkably, the peaks were shifted to low diffraction angles that those for bulk $CoFe_2O_4$. This feature indicated a reduction in the cell parameter of the crystallographic structure, as seen in TEM measurements. Moreover, the broadness of the peaks was a clear signature of the presence of small particles. In addition, the Scherrer formula was used to compute the crystallite size, equation (1.39):

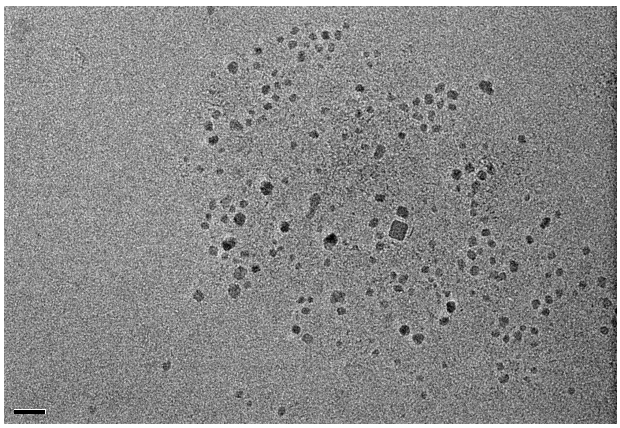

(a)

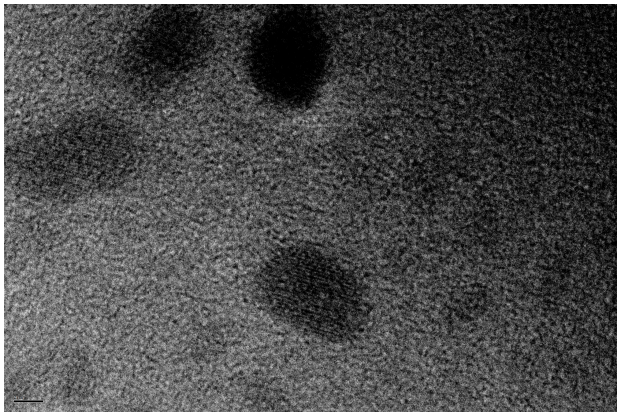

(b)

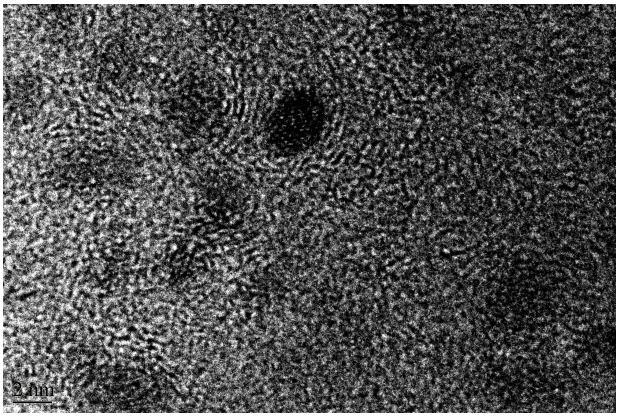

(c)

Figure 1.13: TEM images of the three $CoFe_2O_4$, in the three samples were founded two different distribution size of nanoparticles. a) Sample A, b) Sample B, and c) Sample C.

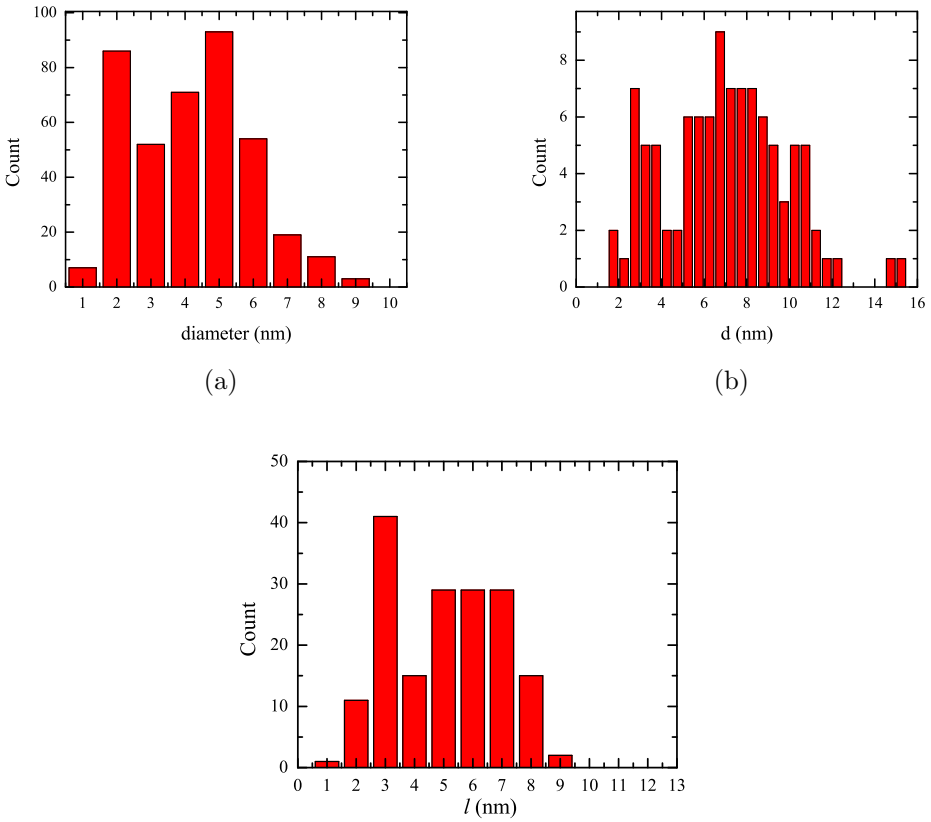

Figure 1.14: Size distribution for the three measured samples. All the size distributions were fitted to a sum of two log-normal functions, obtaining 2.01 and 4.5 nm for sample A, 2.0 and 6.75 nm for sample B, and 2.6 and 5.4 nm for sample C.

$$d = \frac{0.94\lambda}{\beta \cos\theta} \tag{1.39}$$

being λ the wave length of the X-ray, β the broadness of the Bragg peak at half height, and θ the angle where the peak occurs. Taking into account the position of the two detected peaks (35° and 61°), the obtained crystallite sizes, for each peak, were 4.79 and 6.79 nm, differing one with each other.

Skoropata et al. [29] discussed that the measured X-ray spectrum, of our three sets of $CoFe_2O_4$ cannot be interpreted solely on the basis of a $CoFe_2O_4$ spinel structure and the Scherrer broadening. Calibration spectra recorded under the same conditions and with a reference sample showed that the fluorescence and instrumental broadenings of the peaks were below 0.2° in the entire experimental

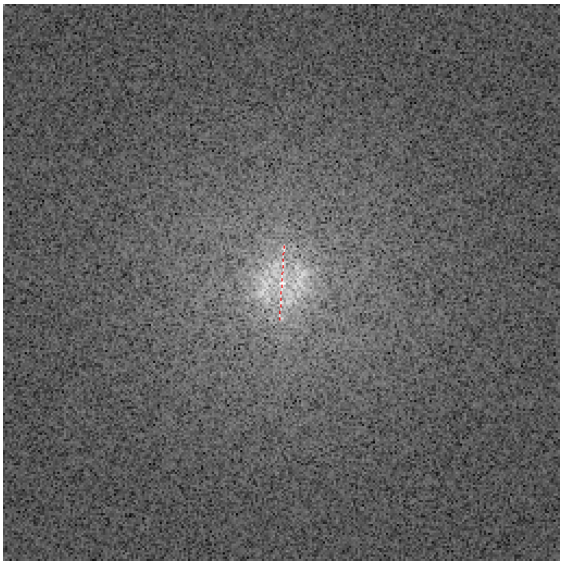

Figure 1.15: Result to apply the Fourier transform in one large nanoparticle in sample C.

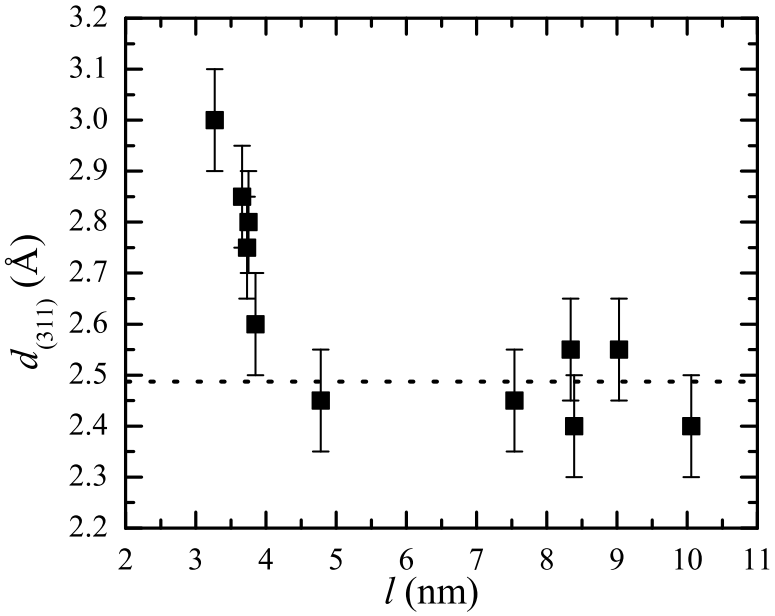

Figure 1.16: Interplanar distance as a function of nanoparticle characteristic size. It is observed that the smaller the particle, the bigger the interplanar distance. The doted horizontal line indicates the expected value for bulk cobalt ferrite, which coincides with the case of large particles.

window and cannot be the origin of the discrepancy. Thus, the quality of XRD spectra was sufficient, and the broad peaks we have measured were inherent of the sample and not due to experimental errors.

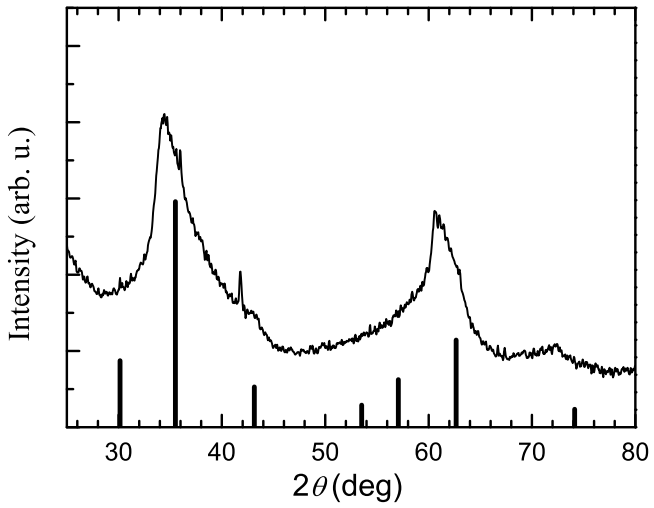

Figure 1.17: X-ray for sample C carried out with k-α cooper line. The fine lines represent the different difraction peaks for bulk cobalt ferrite. Comparing the peaks associated with the particles and with the bulk, a clear enlaregement of the particles is observed.

However, the combination of CoO and Fe-oxide can mimic the $CoFe_2O_4$ spectrum. In the case of the spectrum of our samples, it was different form bulk $CoFe_2O_4$ and the one corresponding to the mixture of CoO and Fe-oxide since in our spectra only two peaks were clearly seen. Moreover, the addition of CoO in the Fe-oxide would shift the original peaks to higher angles, but the peaks in our sample were moved toward low angles.

In conclusion the broadness of the peak and its shift to small angles respect to bulk material was an indication of the presence of small particles. In addition, the feature of having different sizes in each sample made that the measured signal was the convolution of individual diffracted spectra for each particle.

1.5. Magnetic studies

For clarity in this section we only show the results for sample C, because the experimental set up and results for sample A, B, and C are analogous. For further information of samples A and B see appendix A. The magnetic measurements were carried out using a commercial magnetometer, SQUID, from Quantum Designs ltd. The metastable curve, zero-field-cooled (ZFC) and the stable curve, field-cooled (FC) magnetization data, were measured with an applied field of 1 mT, and they are shown in figure 1.18. The ZFC measurement protocol was performed as follows:

first,the sample was cooled down to the lowest temperature (T=2 K) at zero field; afterwards the measuring magnetic field was applied and the magnetization was recorded as the sample's temperature was increased at a constant sweep rate of about 1 K/min. The FC protocol only differed from the ZFC in that the measuring field was applied before cooling the sample.

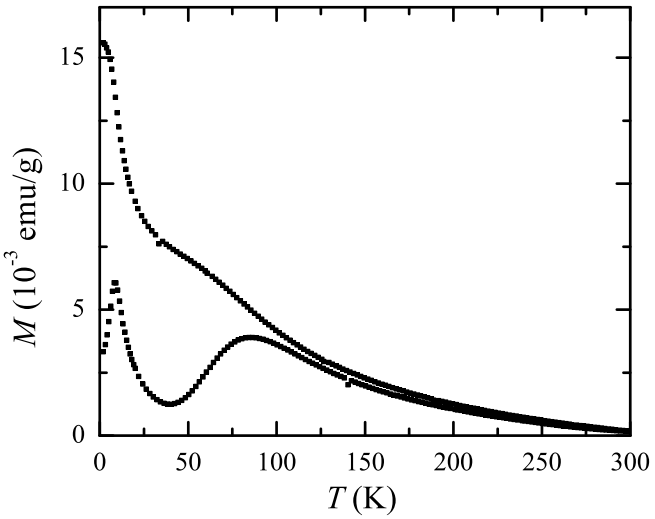

Figure 1.18: Temperature dependence of the ZFC (lower curve) and FC (upper curve) magnetization data measured under an applied field of 1 mT. The magnetization peaks at 8.5 K and 90 K.

The data revealed that above $T = 2K$, the ZFC magnetization curve increased strongly from the initial value to a maximum at 8.5 K; above this temperature the magnetization decreased following a paramagnetic curve, $M = C_1 + 1/T$, until 20 K, on which C_1 is a parameter representing the magnetic contribution of the blocked large particles, whose magnetization in this small range temperatures may be assumed constant. The magnetization increased again until having a next maximum at $T = 90$ K, above it decreased until room temperature. The equilibrium FC magnetization curve, which increased when decreasing the temperature, deviated from the ZFC at round 150 K being the irreversible temperature. At $T < 150$ K the FC curve increased until reach a maximum at 8.5 K, and in the temperature interval between 20 and 8.5 K , it followed a similar paramagnetic law, described by $M = C_2 + \frac{1}{T}$ dependence like in the case of the ZFC data.

To even more support the conclusion of both existence of two sets of $CoFe_2O_4$ nanoparticles centered at two different sizes, Thermal Remanent Magnetization experiments were carried out, figure 3.10. The TRM mesurements were perfomed

with the following procedure: first a 50 kOe magnetic field was applied at 300 K and then we field-cooled the sample until 2 K. At this low temperature the field was switched off and the remnant magnetization was measured between 2 and 300 K

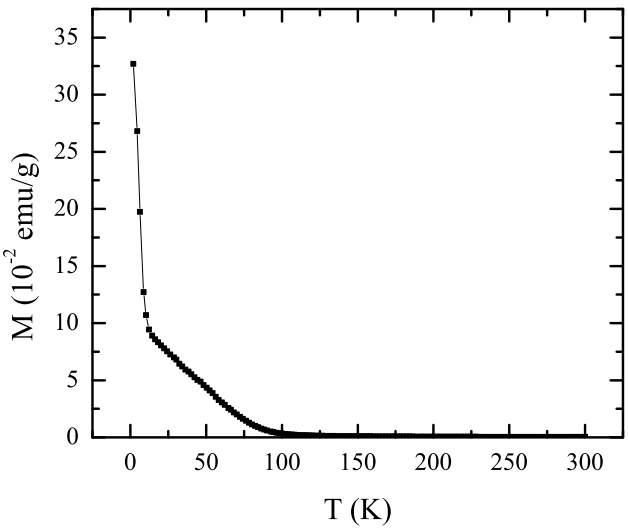

Figure 1.19: TRM of sample C, two different inflection points are observed at 10 and 100 K, that is the same position than the peaks detected in the ZFC-FC curves.

The data of the TRM measurement showed a reduction of the remnant magnetization as a function of the temperature. At 10 K an inflation point was present separating two different thermal regimes related to the bimodal size distributions. The derivative of TRM data was computed to obtain the distribution of energy barriers of the system, as it predicts equation 1.27 (figure 1.20). In the computed derivative was clearly observed two different barrier energy associated with the bimodal size distribution of particles, in concordance with the TEM and ZFC-FC data. The peaks related to the blocking temperatures for each size were 6 K, and 75 K, respectively. Therefore the TRM data could agree well with the interpretation that in a $CoFe_2O_4$ powder sample existed two blocking temperature corresponding to each size of particles. This interpretation was supported by the coincidence with the inflation point for the ZFC-FC curves, as expected. Furthermore, in figure 1.20 it was also represented the barrier distribution for a unimodal $CoFe_2O_4$ particles having a single distribution of sizes and a very similar blocking temperature. The unimodal size distribution sample did not show the peak at low temperature.

On the basis of our data, we proceed to compute the blocking temperature

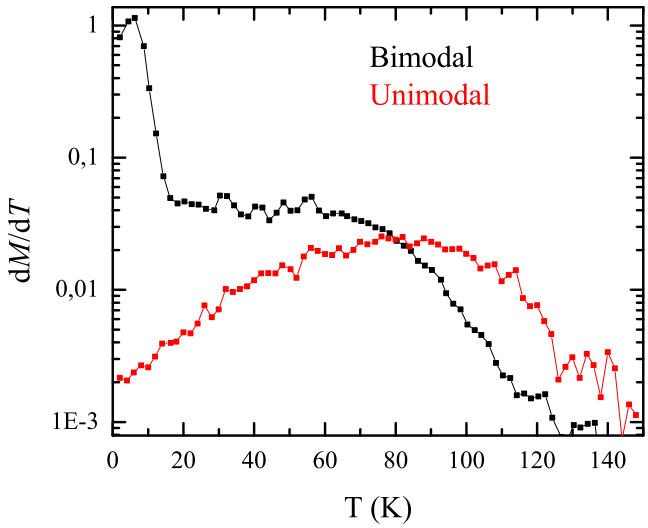

Figure 1.20: Energy barrier deduced from the TRM data. Two different peaks are detected, at 6 and 75 K, at the same positions as the inflection points in the ZFC-FC data. Otherwise, a similar size distribution (in the case of large particles) is represented as well, to obtain a direct comparison between large particles and other $CoFe_2O_4$.

related to the bimodal size distribution using equation 1.18, with $k_B = 1.38 \cdot 10^{-16} erg\ K^{-1}$ being the value of Boltzman constant, 2.6 nm and 5.6 nm the mean size of the bimodal distribution and considering the particles were cubic. The used value for the anisotropy constant was $CoFe_2O_4$ bulk value, $K = 2 \cdot 10^6 erg\ cm^{-3}$:

$$T_B\,(2.4nm) = \frac{KV}{30k_B} = 8.5K$$

$$T_B\,(5.6nm) = \frac{KV}{30k_B} = 76K$$

The result for large particles (5.6 nm) was in concordance with the value measured in the TRM and ZFC experiments. But the value obtained for small particles, 2.3 nm, was larger than the value measured in the ZFC-FC and TRM curves. This fact can rely upon size effects [30] depicted in equation 1.40:

$$K_{eff} = K_{bulk} + \frac{S}{V} K_s \tag{1.40}$$

where K_{bulk} is the anisotropy constant of bulk material, S is the surface of the particle , V is the volume of the particle, and K_s is the surface anisotropy constant. Equation 1.40 strongly depends on the surface-volume ratio that increases as the

size of the particle decreases. Nevertheless, taking into account the computed blocking temperature was larger than the measured in the ZFC-FC and TRM values, it turns out that the anisotropy constant had a lower value for small particles that its value for bulk material, which is not explained in terms of equation 1.40. Consequently, this interpretation of the peak at low temperatures as a blocking associated with small particles cannot be done. In addition, $CoFe_2O_4$ nanoparticles larger than 5.6 nm showed a tendency toward cubic anisotropy. On the other hand, particles with diameter lower than 5 nm presented uniaxial anisotropy [31], [32]. Therefore, it is reasonable to think, for samples with bimodal distribution centered at 2.3 and 5.6 nm, that a coexistence of uniaxial and cubic anisotropy should be present. However, this change in the type of anisotropy cannot explain the presence of such a narrow peak in the low temperature regime, despite the broadness of the size distribution.

For a correct understanding of the peak at low temperatures detected in the ZFC data, it was measured the temperature dependence of the ac susceptibility recorded at different frequencies for the ac field, ranging from 1 to 1000 Hz. In figure 1.21, both the in-phase and out-of-phase components were observed, showing two maximas similar to the ZFC magnetization. In the case of the out-phase-component the maximum corresponded to the inflation point of the in-phase susceptibility in all the frequency range, as depicted in figure 1.22.

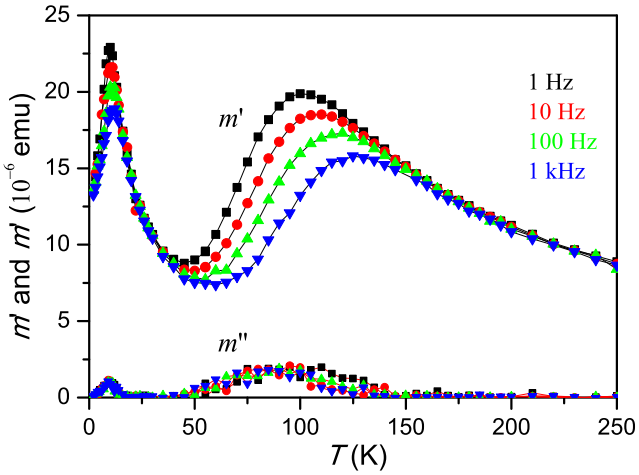

Figure 1.21: Temperature dependence of the in-phase, m', and out-phase, m", components of the ac-susceptibility measured at different frequencies. The high-temperature peak shifts to higher temperatures as a function of the applied frequency. On the other hand, the low-temperature peak remains at the same position for all the applied frequencies.

The position of the high-temperature peak depended logarithmically on the

used frequency (see equation 1.18) according to the Arrhenius thermal activation law over an energy barrier, using the value of the anisotropy constant deduced above and the value of about $10^{-11}s$ for the attempt time. This is clearly seen in the case of the in-phase susceptibility for all frequencies, see figure 1.22. Thus, the three exposed experimental facts (ZFC-FC curves, TRM, and ac-ZFC) are clear signatures that the high-temperature peak corresponded to the blocking temperature of the large magnetic particles.

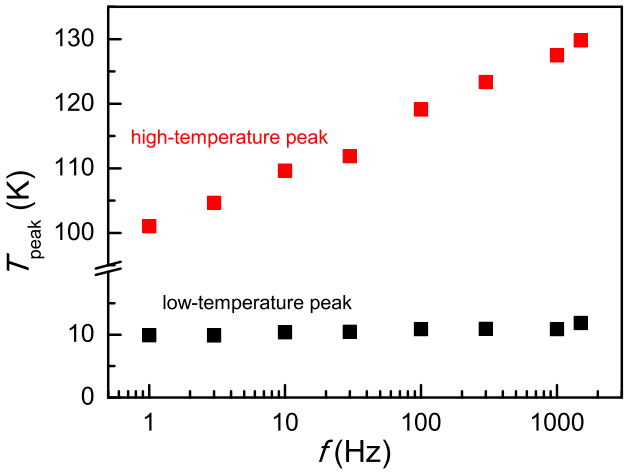

Figure 1.22: Peak vs logarithm of frequency. The displacement of the peak at high temperatures follows a logarithmic law with the ac-frequency. From the fit, using equation 1.18 is extracted the attempt time, $\tau_o = 10^{-10}s$. Otherwise, the peak at low temperature did not fits with an Arrhenius law.

The position of the low-temperature peak of both components had a very little dependence on the ac-frequency used and appeared always at 8.5 K, which was the same value of the low-temperature peak in the ZFC magnetization. The invariance of the low-temperature peak of the frequency of the applied magnetic field suggests that this peak was not a blocking temperature related to the small particles. Since cobalt ferrite is a ferrimagnetic material due to its spinel structure, and the lattice was deformed for the smaller particles, as shown in HRTEM data, we suggest that the low-temperature peak was a phase transition, between the paramagnetic state ($\frac{1}{T}$ law) and the ferrimagnetic phase. That is, below 8.5 K, the smallest particles were magnetically ordered, whereas above this temperature, they behaved paramagnetically. Furthermore, fitting the data at low temperatures with an Arrhenius law it results on an unphysical value for the attempt time, τ_o of about 10^{-20} s, which supports our hypothesis.

This interpretation encouraged us to perform measurements of ZFC curves at

much higher fields, as shown in figure 1.23. The measurement protocol was the same as for the ZFC-FC protocol, but in each measurement it was applied different and higher fields, ranging from 1 to 50 kOe. First the sample is cooled down to the lowest temperature at zero field, afterwards the magnetic field is turned on and the magnetization recorded as the sample's temperature is increased. In all the measurements the sample was previously warmed up until 200 K to ensure all the magnetic moments were randomly oriented.

From the figure 1.23, it is clearly seen that the high-temperature peak shifted to lower temperatures when the magnetic field was increased, and disappeared for fields larger than 10 kOe, as seen in equation 1.21. The case of the low-temperature at 8.5 K peak was completely different, it suffered only a small shift to lower temperatures for fields of the order of several Teslas, such as the effect of the ac-field on the in-phase and out-phase components.

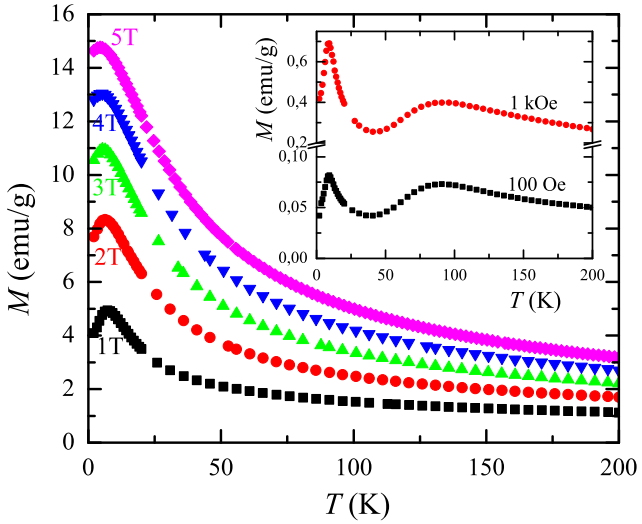

Figure 1.23: ZFC magnetization obtained at different magnetic fields (10, 20, 30, 40 and 50 kOe). The inset shows the magnetization data at lowers fields (10 and 100 mT). The high-temperature peak at about 90 K shifts to lower temperatures as the field increases and disappears for fields higher than 1 kOe, whereas the peak at low temperatures remains for all the values of the applied fields.

As explained before the energy barrier associated with the magnetic anisotropy can be destroyed with an applied magnetic field, $H = H_K$ where H_K is the anisotropy field (see equation 1.21). This anisotropy field is defined as the necessary field to fully destroy the energy barrier; $H_K = 2K/M_S$, where M_S is the magnetic saturation of the particle and K the anisotropy constant. From figure 1.23 it is clearly seen that the anisotropy field was lower than 10 kOe, and, as

mentioned in the discussion for ac-susceptibility the peak at high temperature corresponds to the blocking temperatures of large particles.

The case of the low-temperature peak at 8.5 K was completely different. It suffered a little shift to low temperatures (for 8.5 to 4.5 K), having an anisotropy field higher than 50 kOe. This little shift to lower temperatures, and the lack of dependence on the ac-frequency , pointed again that the low-temperature peak was not a blocking temperature, and it clearly supported a magnetic phase transition phenomena in small particles. Furthermore, the $\frac{1}{T}$ behavior of the paramagnetic signal of the small particles was modified by as we increased the applied magnetic field. Remarkably, the magnetic coupling existing below 8.5 K was almost unaffected by the magnetic field, indicating strong exchange coupling inside the small particles.

In addition, if small particles presented a phase transition between ferrimagnetic-to-paramagnetic state, one can expect that the magnetic hysteresis loop, at high temperature, should be a combination of a paramagnetic and superparamagnetic signals. For this reason, isothermal magnetization studies of the samples have also been performed in the temperature range between 2 and 100 K, as depicted in figure 1.24. The protocol was as follow: First the sample was cooled down without an applied field to the desire measurement temperature. Afterwards, the magnetization was recorded as a function of the magnetic field, between -50 and 50 kOe.

From this curve, below 10 K it is clear that the average anisotropy field of all particles at low temperatures was higher than 50 kOe, in agreement with the existence of high magnetic anisotropic $CoFe_2O_4$ nanoparticles, while the coercive field, even at lowest temperature of 2 K, was only 0.3 T . This small value of the coercive field was the consequence that, even at this low temperature, there were still very small nanoparticles that behaved superparamagnetically, having zero magnetization at zero field. The Langevin temperature dependence of these very small superparamangetic nanoparticles was deforming the entire magnetization curve, reducing, therefore, the value of the coercive field.

At $T = 10$ K, contribution of the paramagnetic signal of the small particles went to zero, which was the reason for the small coercivity at this temperature. The hysteresis cycle was not closed even at 50 kOe, which may be the consequence of the very high value of the magnetic anisotropy field of the small particles.

In the temperature range between the order temperature and the blocking temperature of large particles ($10K < T < 75K$), the hysteresis loop reduced and a paramagnetic signal overlapped the magnetization, as expected if small particles had a phase transition below 10 K. Small particles became paramagnetic.

At $T > 100$ K, the M(H) curve corresponded to the case when the small particles behaved paramagnetically and the large particles were superparamagnetic.

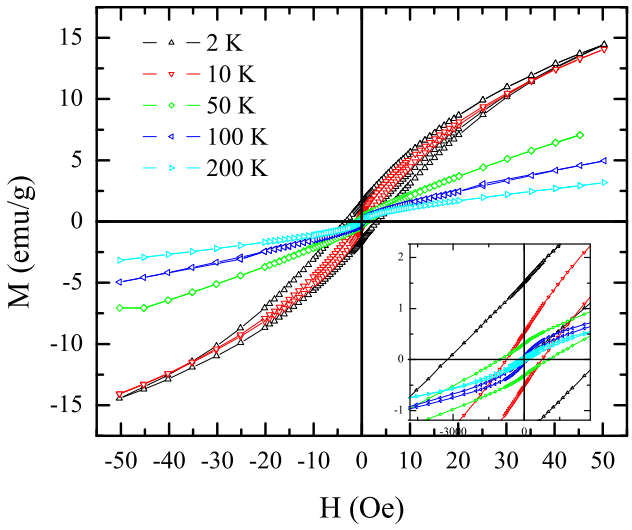

Figure 1.24: Magnetic hysteresis curves recorded at different temperatures (2, 10, 50, 100, and 200 K). In the inset (zero field region), it is observed a superparamgnetic state above 100 K.

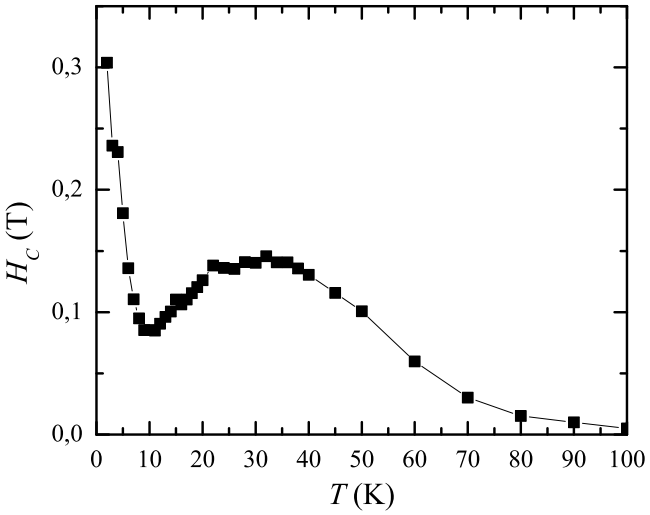

Figure 1.25: Coercivity as a function of temperature. In the plot exists two different regime, one associated with the paramagnetism of the small particles, and secondly with large particles.

Consequently the system exhibited neither remanence nor coercivity.

As support material, in figure 1.25 the coercive field, H_c is represented as a

function of the temperature. The values of coercive field increased with lowering the temperature as more particles were blocked and there was not enough thermal energy to overcome the barrier height. Around 30 K, it was observed a maximum and the follow up decreasing until 10 K corresponded to the case when both sets of particles, the small paramagnetic and the large, were contributing to the detected signal. Below 10 K, basically was observed the coercivity of smallest particles.

It is also important to remark that any attempt to fit the high temperature magnetization data above the blocking temperature ($T > 100\ K$) of large particles, assuming that all particles are super paramagnetic, fails. However, it was obtained a good fit of the magnetization curve at these high temperature with the expression:

$$M(H,T) = \int_0^\infty L\left(\frac{\mu H}{k_B T}\right) f(\mu)\, d\mu \tag{1.41}$$

in the fit, we were assuming that large particles were superparamagnetic and that there was a paramagnetic signal due to the smallest particles. In this case we have determined that the value of magnetic moment of the paramagnetic smallest particles was 2 ± 1 Bohr magnetons. This number was about two order of magnitude smaller than the value expected for 2-3 nm super paramagnetic $CoFe_2O_4$ particles. Therefore the magnetization of small particles at 100 K was not due to a coherent rotation of all spins in the particles (superparamagnetism) but to the individual signal of individual atomic spins. That is, at temperatures higher than 10 K (above the peak at low temperature), the small particles behaved paramagnetically, not superparamagnetically.

Finally, we have explored the metastability of the system by performing relaxation measurements in all of the temperature ranges between 2 and 90 K. The protocol used was as follows: First, the sample was set at 200 K in order to ensure random magnetic orientation between the particles (much higher than the blocking temperature of the largest particles). Then a field of 50 kOe was applied to saturate the sample. Afterwards the sample was cooled down to the desired temperature, the magnetic field switched off, and the system was allowed to relax to the new equilibrium state while the magnetic moment was recorded. The results are plotted in figure 1.26.

The relaxation of the system at zero field followed a logarithmic law, expected for magnetic nanoparticles. From these curves the magnetic viscosity was computed, following equation 1.20, fitting the magnetization with the logarithm of time, being the slope its magnetic viscosity, see figure 1.27.

The results revealed that at higher temperatures, the viscosity showed a maximum close to 90 K (not shown), then it decreased with decreasing temperature; below 10 K: it had a maximum around 6.5 K.

The results of the magnetic relaxation can also be presented in a different way

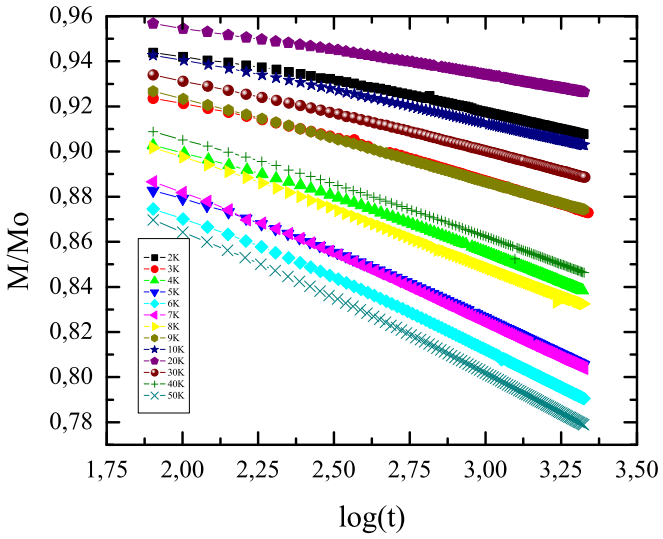

Figure 1.26: Magnetic relaxation at different temperatures. The magnetization has a logarithmic relaxation for all the measured temperatures.

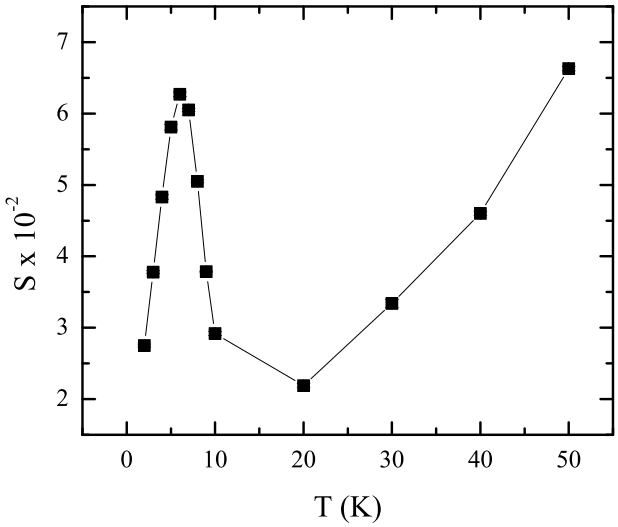

Figure 1.27: Magnetic viscosity. The magnetization peaks at two different temperatures related to the magnetic blocking of the two size distribution, at 6 and 90 K respectively.

to better understand the nature of the physics of the observed phenomena. The time evolution of magnetization M of the sample depends on time only through the

combination of $T\log(t/\tau_o)$, where τ_o is the attempt time to cross the energy barrier, and it is of the order of $10^{-11}s$. This means, for example, that if one observes the $\log(t)$ magnetic relaxation due to the barrier distribution, the coefficient in front of $\log(t)$ must be proportional to T. This is a very natural feature of complex system because, as the observation time is running, the system arrives at greater and greater barriers that are more difficult to overcome. The good scaling observed in figure 1.28 in all the regimes in the $T\log(t/\tau_o)$ plot was clear evidence of the thermally activated process of barrier jumping and of the independent relaxation of the two sets of particles. That is, at high temperatures, the data corresponded to the relaxation of the largest particles, whereas at temperatures below 10 K, the magnetic moment of the biggest was mostly blocked and we only saw the relaxation of the magnetic moment of the smallest particles. This low-temperature behavior of the viscosity indicated that, for the smallest particles, both the ordering and the blocking temperature were very similar.

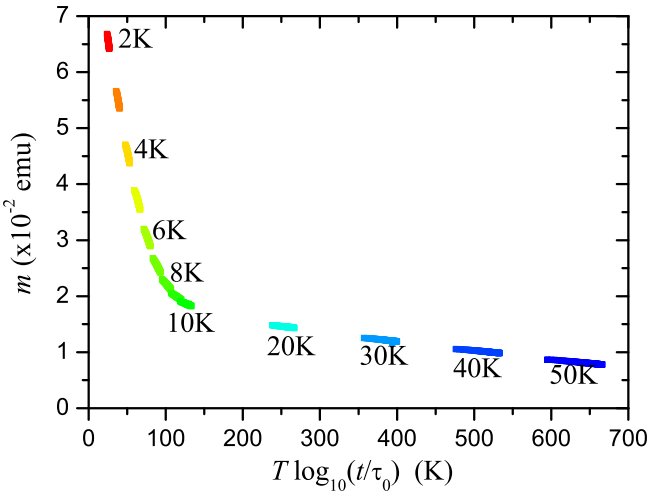

Figure 1.28: Results of the magnetic relaxation experiments shown in a $T\log(t)$ scale. The different colors indicate the different temperatures (shown in the labels) at which the relaxation experiments are performed. In the $T\log(t)$ plot, there are two different thermal regimes.

The low-temperature relaxation results pointed to little anisotropy barriers. The size of the smallest particles, therefore, was responsible for both the low value of the ordering temperature of these particles and the small height of the magnetic anisotropy barriers involved in the relaxation phenomena.

1.6. Conclusions

In summary, in this chapter it has been reported the synthesis, the structural and magnetic characterization of three different powder samples of $CoFe_2O_4$ nanoparticles. The synthesis method consisted in a grow-nucleation process of Fe and Co nucleus, and generated three different sets of $CoFe_2O_4$ nanoparticles capped with oleic acid, which funcionalized and stabilized the particles preventing their aggregation. The chemical analysis by EDS confirmed the relation of 1:2 between Fe and Co, demonstrating impurities were not presented in any sample.

The structural characterization was done using HRTEM and XRD, of which was detected a bimodal size distribution with mean diameters of 2.5 and 5.7 nm, in the sample analyzed in this text (the other results are shown in appendix A). HRTEM images have also revealed an increase in the interplanar distance of the plane (311) in small nanoparticles respect bulk material, suggesting a change in the crystallographic phase. Furthermore, the data obtained with XRD revealed two peaks. These diffraction peaks shifted to lower angles than the diffraction peaks for bulk $CoFe_2O_4$ or other compounds such as CoO, and also suggested a change in the crystallographic structure in the particles, as HRTM data.

The magnetic characterization was carried out in a SQUID magnetometer in which the performed experiments were: ZFC-FC, ZFC-FC at high field, ac-ZFC measurements, hysteresis loops, and relaxation experiments. Concerning to ZFC-FC experiments, two peaks were detected for the three samples, at low and high temperature (8.5 and 75 K for the sample explained in this chapter). Each peak was associated with the bimodal size distribution observed in the structural characterization. In addition ac-ZFC revealed, in the case of the peak at high temperature, a logarithmic dependence on frequency and an attempt time about 10^{-11} s. Moreover, the magnetization data for ZFC at high fields showed an anisotropy field lower than 10 kOe. Hence the peak at high temperatures corresponded to the blocking temperature of large particles.

On the other hand, for the low temperature peak, in ac-susceptibility, the fitting of temperature versus frequency gave an attempt time about 10^{-20} s, being, therefore, an unrealistic result. Furthermore, small particles presented an anisotropy field lager than 50 kOe. All these features were a clear experimental evidence of a lowering order temperature for particles with mean diameter around 3 nm. Therefore, the measured order temperature, 8.5 K was 50 times smaller than the Curie temperature for bulk material. Just below the Curie temperature, these particles were fully blocked presenting an interesting case where the phase transition from ferrimagnetic to paramagnetic phase transition occurred at the same low temperature than the blocking temperature. Furthermore, the magnetic curve, in the hysteresis loop experiments, was a combination of paramagnetic and superparamagnetic signals at high temperatures. Fitting the data to a distribu-

tion of Langevin functions, it was obtained for small particles a magnetic moment about 2 ± 1 Bohr magnetons, in discrepancy to the magnetic moment expected for nanoparticles ranging between 2-3 nm.

On the basis of our data, we suggest that this low-temperature magnetic transition was related to the interplay of surface effects and the increase of the lattice parameter. Due to the small size of the particles and the existence of both "materials", small and large particles, we were not able to get a direct observation of the structural differences between them. However, with HRTEM analysis it was verified that the large particles in the case of other samples had the usual $CoFe_2O_4$ spinel structure. On the other hand, smallest particles may present a different crystallographic structure that reduced the Curie temperature of the material down to 10 K. In other words, there was a strongly reduced exchange interaction energy in the smallest particles as a consequence of the enlargement of the inter planar distance, in agreement with the experimental results. This fact is in agreement with the exponential dependence of the exchange interaction on the interatomic distances. That is, small changes in interatomic distances may produce dramatic changes in the Curie temperature.

In the case of small particles, the variation detected in the cell parameters suggests that the exchange interaction is smaller than that in the bulk and it can even change sign. As a final remark, no effects were introduced by interparticle interactions. We may also conclude that the interparticle interactions were not playing any role in the obtained data because the three analyzed samples had a different ratio between large and small particles and the same phenomenology were always observed.

Chapter 2

Magnetization dynamics and magnetic resonances at Gigahertz frequencies

2.1. Introduction

Microwave technologies are very important in our everyday life [33]. For example mobiles phones has made a new wireless world that connect everyone in everywhere. On the other hand, the ease of microwave generation and detection by electronic systems have generated a wide range of applications out of the wireless communications, such those that in the near future could be present in new medical applications [34] or security tagging [35].

As explained in the last chapter, magnetic nanoparticles show a large potential for: microwaves devices and medical applications [16], [18] owing to their fast dynamics in the superparamagnetic state (SPM) with ac-fields [36], [37], and their resonant phenomena such as the ferromagnetic resonance [38]. For example, the new magnetic memories based on magnetic nanoparticles combine DC-magnetic fields lower than the switching field (minimum field to reverse the magnetization of the particle) with ac-fields at microwave frequencies to store new information [39]. Moreover, magnetic nanoparticles can be used to protect electronic devices or part of their components of electromagnetic radiations or interferences due to their loses at high frequencies. Besides, the tunable properties of magnetic nanoparticles can control the broadness of the work-band in microwaves devices.

On the other hand, in the last decades, interesting medical applications such as Nuclear Magnetic Imaging, or Hypertemia have been combined with magnetic nanoparticles working at microwave frequencies [40], [41]. For example, NMI uses superpamagnetic particles to increase the contrast in the images due to the power

absorption of the particles in this frequency range. In magnetic hyperthermia [42], SPM particles are attached to a specific molecule in order to recognize cancer cells. Once the magnetic nanoparticle is joined to the cell, it is exited with electromagnetic radiation, and the coherent fluctuations of its magnetic moment and/or the mechanical rotation of the particle increases the temperature of the particle until 50 C, destroying the cancer cell.

Regarding to the fundamentals aspects of magnetic nanoparticles, in the first chapter we demonstrated that the blocking temperature of a magnetic nanoparticle depends on the measuring time or the frequency of an ac-field (section ac-ZFC). For an ac-field, as its frequency increases the magnetic moment of the particle can become blocked even above its blocking temperature. This feature is based upon the fact that the switch of the field occurs in a time lower than the attempt time of the particle to overcome its energy barrier. It turns out that this phenomenon is equivalent to an increase of the blocking temperature as a function of the frequency. Consequently, for particles in the superparamagnetic state at room temperature can behave magnetically blocked at microwave frequencies.

Furthermore, magnetic materials where their spins interact between them (for instance ferromagnets) have a resonance phenomenon known as the ferromagnetic resonance (FMR) (for antifferomagnetic and ferrimagnetic materials is also possible define a resonance phenomenon). For a ferromagnetic material the resonance condition occurs at a frequency that depends on the anisotropy of the system, the magnetic field, and the magnetic moment of the material. At the resonant frequency the amplitude of the magnetization of the system increases dramatically as a consequence of the resonant absorption of the energy of the field. As an important condition, the ferromagnet must be uniformly magnetized, otherwise the resonant frequency depends on each zone of the magnet. In the case of ferromagnetic nanoparticles [43] the resonance condition turns out to be more complicate than for bulk material. These features are due to the size distribution of the particles, the random orientation of the anisotropy axes. The main consequence, therefore, is an increase of the linewidth of the FMR.

In this chapter we show our studies on magnetite (Fe_3O_4) and manganite particles ($La_{0.6}Sr_{0.3}MnO_3$) among microwave frequencies using coplanar transmission lines. The chapter is structured in the following sections: First the studied samples will be presented, and their structural, magnetic and electrical characterization will be exposed. Finally, the results of the spin dynamics at microwave frequencies of the studied particles will be shown as well as our main conclusions.

2.2. Fe_3O_4 and $La_{0.6}Sr_{0.3}MnO_3$ samples

The samples analyzed in this chapter were Fe_3O_4 magnetite nanoparticles capped with silica and $La_{0.6}Sr_{0.3}MnO_3$ manganite particles, both in powder form. Size distribution, particle morphology and shape for magnetite particles were measured using a JEOL TEM 2100 transmission electron microscope. The samples were prepared by drying a hexane dispersion of the particles on amorphous carbon-coated copper grid. Figure 2.1 plots an TEM image of the Fe_3O_4 nanoparticles. The mean particle size and distribution were evaluated by measuring the largest dimension of the particles due to their cubic shape (size histogram is shown in figure 2.2). Mean diameter was extracted fitting the measured size hystogram to a Gaussian distribution function, where the mean diameter was 44 nm. Remarkably, the ensemble had particles below 20 nm (the 2.5% of the total), and particles with a mean diameter of 70 nm. Hence the sample were composed by a wide range of sizes ranging form 5 to 70 nm.

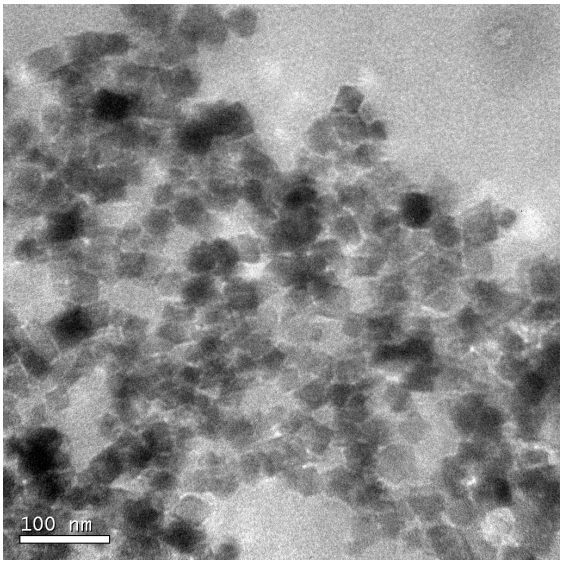

Figure 2.1: TEM image for $F3_3O_4$ nanoparticles. In the picture is clearly seen particles of 50 nm size.

The sample having $La_{0.6}Sr_{0.3}MnO_3$ manganite particles had three different sizes: 0.5, 0.8 and 2 μm, and mean diameter round 1 μm.

2.3. Magnetic studies

Magnetic studies were carried out using a SQUID magnetometer and following the same experimental protocol for Fe_3O_4 and $La_{0.6}Sr_{0.4}MnO_3$ particles. They

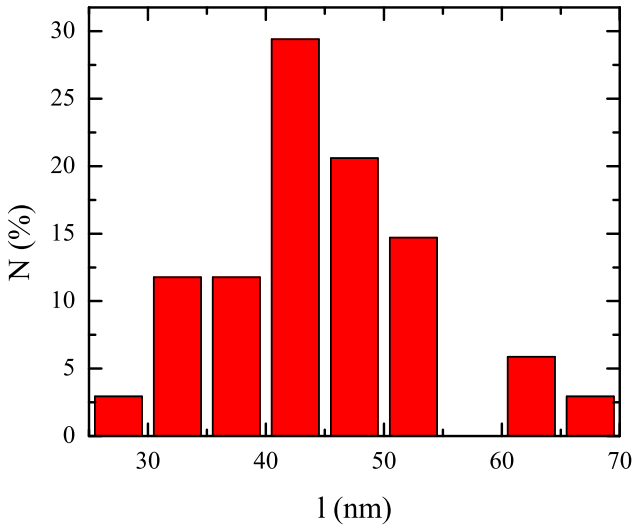

Figure 2.2: Particle size distribution for Fe_3O_4. The result shows a mean distribution of 44 nm with a broadness between 5 and 70 nm. Moreover particles with size between 60 and 70 nm were also detected as well as below 30 nm.

consisted of a ZFC-FC and hysteresis loop measurements. ZFC-FC measurements were performed as follows: first,the sample was cooled down to the lowest temperature (T=2 K) at zero field; afterwards the measuring magnetic field was applied, 50 Oe, and the magnetization was recorded as the sample's temperature was increased at a constant sweep rate of about 1 K/min. The FC protocol only differs from the ZFC in the fact that the magnetic measuring field was applied before cooling the sample. In figures 2.3 and 2.4 are plotted the results for Fe_3O_4 nanoparticles and $La_{0.6}Sr_{0.3}MnO_3$ particles respectively.

ZFC data for Fe_3O_4 nanoparticles show that for $T > 2K$ the magnetization increases from its initial value until 100 K, where the curve has an inflection point. For $T > 100$ K the magnetization still increasing even at $T > 300$ K. The equilibrium FC magnetization curve, which increases when the temperature is reduced, deviated from the ZFC at 300 K (the irreversible temperature). At $T = 100$ K an inflection point was observed, and for $T < 100$ K the magnetization remained constant. No maximum was detected in the ZFC-FC curve associated with a blocking temperature.

The inflection point detected at 100 K corresponds to the Verwey transition: above the transition temperature the magnetite nanoparticles are in a spinel structure, where cations Fe^{+2} occupy tetrahedral sites (A) and Fe^{+2} are localized in octraedral sites (B). Below the transition temperature a crystallographic distortion

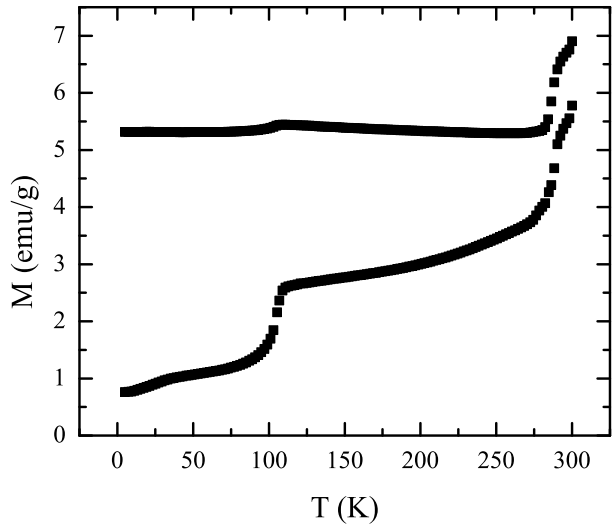

Figure 2.3: ZFC-FC for Fe_3O_4 nanoparticles. As seen in the figure, at 100 K occurs the Vervey transition. Moreover, the mean blocking temperature of the particles is above 300 K.

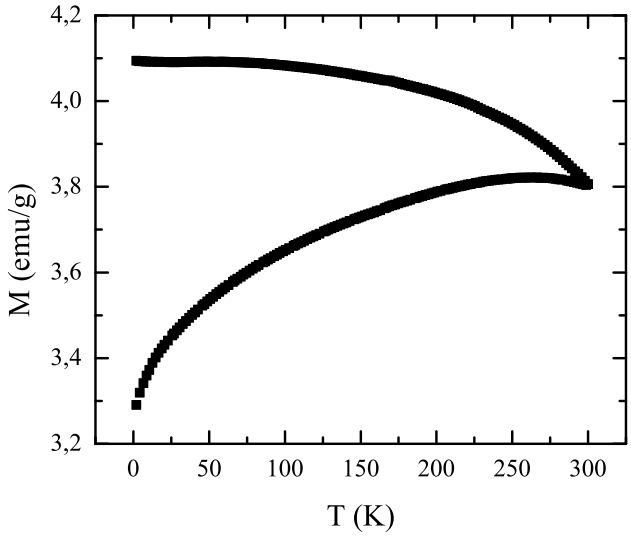

Figure 2.4: ZFC-FC for $La_{0.6}Sr_{0.3}MnO_3$ nanoparticles. Transition from ferromagnetic state to paramagnetic was observed, which occurs at 370 K.

occurs that induces a charge ordering in A-sites ions. Consequently, at this temperature the sample suffers a phase transition from conductor to insulator. From

a magnetic point of view, the new cation order inside the material changes the crystal field and thus the anisotropy constant. Taking into account this feature, we computed the size distribution using equation 1.25 from the data of the ZFC-FC measurements. The values used for the anisotropy constant are: for $T > 100$ K it is the same value that for bulk material ($H_{sat} 1.1 \cdot 10^5$ erg/cm^3), but below the Vervey transition it is $K = 8 \cdot 10^5$ erg/cm^3. This value was extracted using the magnetic saturation and the anisotropy field at 50 K (below the transition temperature) , and the relation $K = \frac{1}{2} M_S \cdot H_a$.

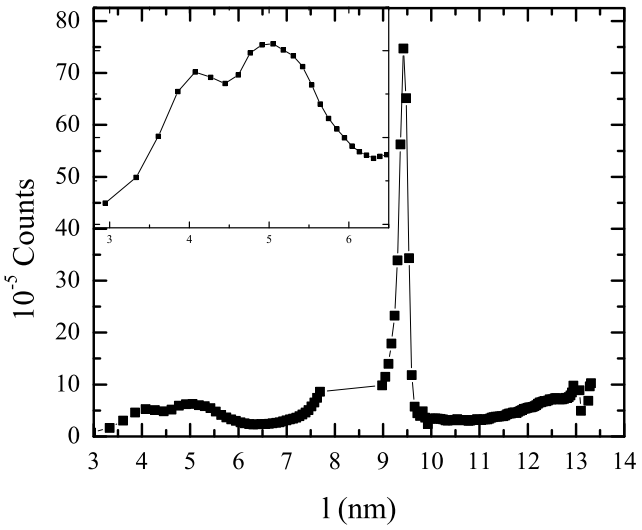

Figure 2.5: Computed size distribution for Fe_3O_4 nanoparticles. The peak detected at 9 nm corresponds to the Vervey transition, which generates an artifact that can be confused with a thin size distribution. Remarkably particles smaller than 6 nm were observed.

Figure 2.5 shows four clearly peaks in the obtained magnetic volumes: at 4, 5, 9 and above 13 nm. Taking into account the values of the anisotropy constant, it is clear that the peak 9 nm is associated with the Verwey transition, and is not a real size. Nevertheless, the minor distribution that peaks at 4 and 5 nm correspond to ultrafine nanoparticles that were also observed in the TEM measurements. Therefore, the nanoparticles that contribute to the ZFC-FC magnetization are those with a size below 13 nm (maximum size obtained in figure 2.5).

On the other hand, for manganite 1 μm particles, ZFC-FC magnetization increased from $T = 5$ K until $T = 300$ K. FC magnetization data followed the behavior of ferromagnetic particles, for which the magnetization reduced increasing the temperature until the Curie temperature. In our sample, Curie temperature was not observed because it was 370 K. However, the transition (transient between

saturate state to zero magnetization) was observed until room temperature. Since the mean size of manganite particles was 1 μm the particles were multidomain particles. Consequently, the ZFC-FC corresponds to ferromagnetic particles with a Curie temperature above 300 K.

With the aim to have a full characterization of our samples, hysteresis loops were carried out at 300 K recording the magnetization as a function of the magnetic field, between -3 and 3 kOe, the same interval such as the microwave experiments. Figures 2.6 and 2.7 show the isothermal curves recorded at 300 K for magnetite and manganite nanoparticles respectively.

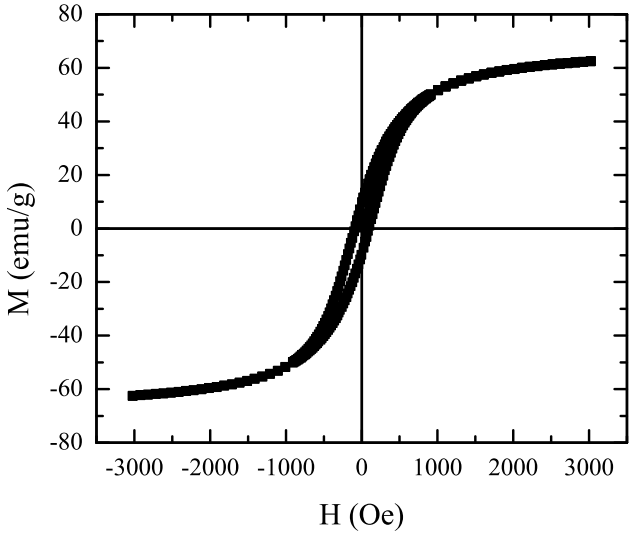

Figure 2.6: Isothermal magnetization at constant temperature 300 K. The data shows a coercieve field about 88 Oe, $0.24M_S$ remanance and a saturation field of 1 kOe.

Using the isothermal data, it was determined that, at 300 K, Fe_3O_4 nanoparticles have a coercive field of 88 Oe, a remanence of $0.24M_S$ where M_S is the magnetic saturation of the sample, and a saturation field of 1 kOe. As described above, for 44 nm length nanoparticles their blocking temperature is above 300 K, thus the coercitivity must be larger than the founded value. As shown in the ZFC-FC data there exist particles with sizes smaller than 6 nm, whose blocking temperature is below 300 K, and, consequently such particles behave superparamagnetically explaining the reduction of the coercivity.

In the case of manganite particles, the isothermal magnetization curve at room temperature followed a Brillouin function in agreement with the ZFC-FC magnetization data. The value of the saturation field was 2.5 kOe.

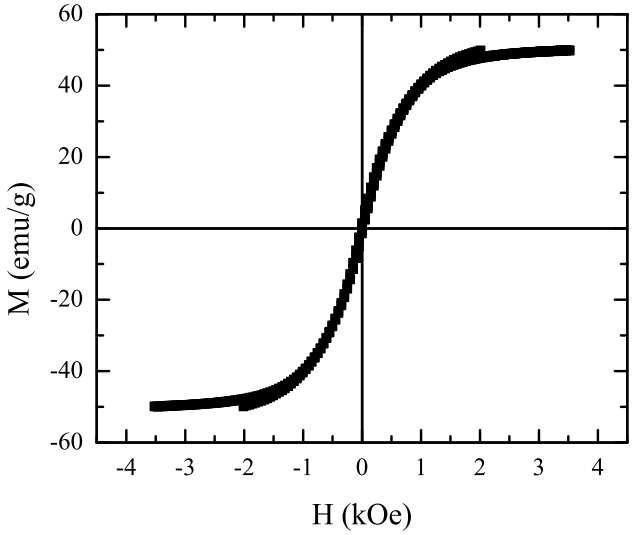

Figure 2.7: Hysteresis loop measured at 300 K for manganite particles. As it was seen in the ZFC-FC measurements, the data fitted with a Brillouin function that means the system transitates at this temperature from ferromagnetic to paramagnetic state.

2.4. Magnetoresistance experiments

In order to have a fully characterization of the physical properties of both samples we also carried out magnetoresistance experiments. Because the samples were powders, it was used a press to form a tablet of each sample. The preparation consisted of: it was prepared 30 mg of each sample and pressure for 5 minutes, applying a pressure of 200 Pa/cm^2. With this method a tablet with a diameter of 1 cm was made, and used for both the magnetoresistance and microwave experiments.

The sample holder was constructed by a plate of fiber glass, where the sample was fixed by the application of silver paint in two opposite extrems of the sample (see figure 2.8). The silver electrical contacts were also attached to two cables that applied a voltage, and measured the electrical current that crossed the sample using a source meter Kethley from Agilent ltd. To apply an uniform magnetic field, the sample holder was placed in the air gap of an electromagnet that was attached to a power supply to control the electrical current and, hence, the magnetic field applied to the sample. A Hall probe measured the magnetic field that generated the electromagnet, whose characteristic curve is represented in figure 2.9. The results show that the electromagnet was magnetically saturate at 3.5 kOe, corresponding to the maximum field that was possible to apply in our experiments.

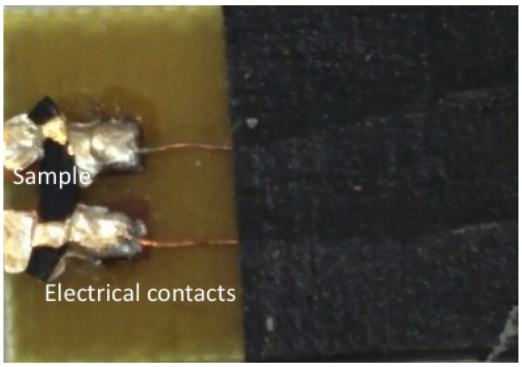

Figure 2.8: Sample holder used for the magnetoresistance experiments. The base consisted in a fiber glass plate, and two copper lines. The sample was attached to the two copper lines using silver paint. The two electrical contacts were used to apply a voltage to the sample and measure the induced current.

The measurement protocol was as follows: a constant voltage was applied whereas the magnetic field was swept from -3.5 to 3.5 kOe. A computer program controlled all the process and recorded the current induced by the applied voltage to compute the electrical resistance of the sample , that is the Ohm's law. Data analysis consisted on compute the relative variations respect to the resistance at zero field (see figure 2.10).

Fe_3O_4 nanoparticles have a electrical resistance at zero magnetic field of 45 $M\Omega$. The electrical resistance followed down until 1 kOe, where its reduction was around 1%. For $H > 1$ kOe, above the saturation magnetic field, the value of the electrical resistance remained constant. Consequently, ferrite nanoparticles presented a magnetoresistance phenomenon: the electrical resistivity decreases as a function of the magnetic field until the saturation field.

On the other hand, in the magnetoresistance measurements for $La_{0.6}Sr_{0.3}MnO_3$ particles, it was observed a larger variation of the electrical resistance than Fe_3O_4 nanoparticles, as seen in figure 2.11. The relative reduction respect zero field (the value in absence of was 9.6 $k\Omega$) was a 6% until 3 kOe, which corresponds to the saturation field observed in the isothermal measurements.

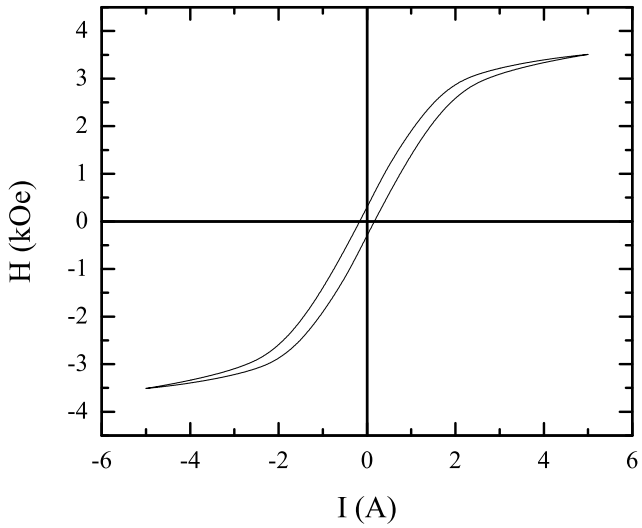

Figure 2.9: Measured magnetic field by the Hall probe in the electromagnet as a function of the current provided by the source power. The data shows that the electromagnet present hysteresis as well as a saturation above 3 kOe. Moreover, the maximum field generated by the electromagnet was 3.5 kOe.

2.5. Microwave experiments

2.5.1. Experimental set-up

Microwave experiments were performed using a Programable Network Analyzer (PNA) form Agilent ltd in transmission and reflection configurations from 1 to 20 GHz. Bistatic measurements were carried out on a coplanar transmission line because they do not have resonant phenomena, and hence are better for studying ferromagnetic resonances.

As in the case of electrical characterization, the sample in form of a tablet was placed at the top of the microwave guide, and the whole piece at the middle of the air gap of the electromagnet (for the magnetic field that can provide see figure 2.9). This experimental set-up ensured the application of a dc-field by the electromagnet, and a ac-magnetic field by the coplanar line. Although the coplanar line was placed perpendicular to the dc-field to detect ferromagnetic resonances, the orientation of the line was not important due to the random distribution of anisotropy axes of the samples. A computer program registered the applied field, the frequency, the real and imaginary component, the modulus and the phase of the bistatic coefficients S_{11} and S_{21} at each frequency. The meaning of these two parameters is: the PNA has two ports that emit and receive the radiation. Let

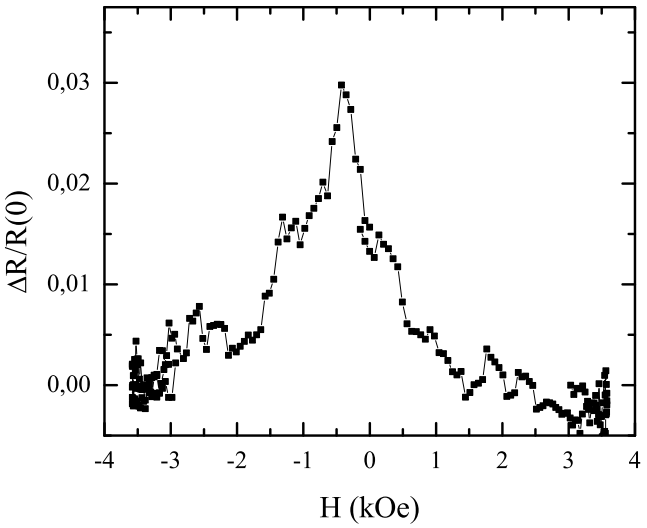

Figure 2.10: Measured magnetoresistance as function of the magnetic field applied by the electromagnet. The data was normalized respect the resistance value at zero field. The electrical resistance of the sample reduces from 0 to 1 *kOe* that corresponds to the saturation field of ferrite nanoparticles.

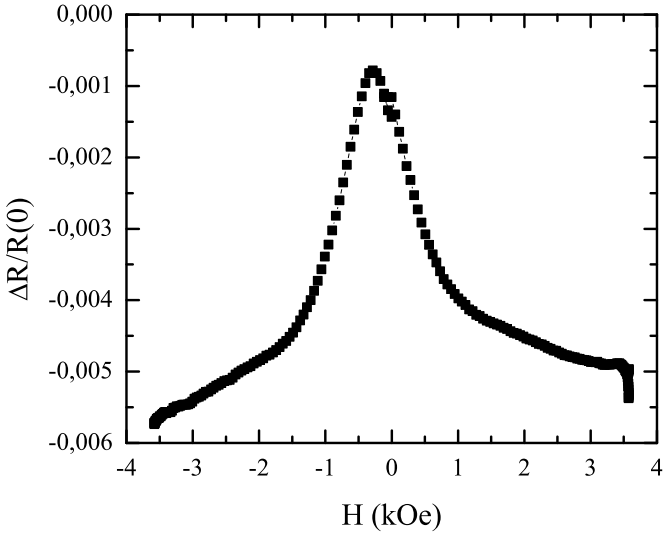

Figure 2.11: Magnetoresistance for manganite nanoparticles. The results show a variation of the 6% of the resistance until 2.5 *kOe*. Above 2.5 *kOe* the magnetoresistance still constant.

us assume that the port i-th emits the microwave and the port j-th receives the radiation, where i and j can be the same port, therefore the parameter S_{ij} becomes:

$$S_{ij} = \frac{S_i}{S_j} \tag{2.1}$$

being S_i the radiation that emits the i-th port and S_j the radiation that receives the port j-th. Consequently the ratio S_{11} is the reflection that measures the port 1 or S_{12} the transmission between the port 1 and 2, and so on. In our studies it was measured the reflection, S_{11}, and transmission, S_{21}, coefficients in the coplanar line.

Data analysis consisted of compute the relative variation of the modulus of the bistatic magnitudes respect the value at the maximum field provided by the electromagnet:

$$\Delta S_{22} = \frac{S_{22}(H) - S_{22}(3.5kOe)}{S_{22}(3.5kOe)} \tag{2.2}$$

where $S_{22}(3.5kOe)$ is the coefficient S_{22} at 3.5 kOe, and $S_{22}(H)$ the value of S_{22} at the field H. In an analogous way the relative variation of S_{21} becomes:

$$\Delta S_{21} = \frac{S_{21}(H) - S_{21}(3.5kOe)}{S_{21}(3.5kOe)} \tag{2.3}$$

To smear out error sources, the reflection and transmission signals of the coplanar line used in the experiments were characterized as a function of the field provided by the electromagnet, in the frequency range between 1 and 20 GHz. The results are represented in figures 2.12(a) and 2.12(b) in the following way; the y-axis represents the frequency of the microwave, the x-axis is the magnetic field, and the color bare corresponds to the relative variation of the coefficients S_{22} for reflection or S_{21} for transmission, for which black is the lowest and white the largest value of both parameters. Both results show a series of minima values for different frequencies that do not depend on the magnetic field. These values are associated with characteristic resonances of the line related to its length, and the connectors. Therefore, the variations with the field of both coefficients in the following experiments are only due to the samples.

2.5.2. Results for Fe_3O_4 nanoparticles

Figure 2.13 depicts the relative variation of coefficient S_{22} between 3 and 8 GHz. It turns out two different behaviors of the microwave reflection as a function of the frequency. First, the S_{22} coefficient has a minimum at zero field. For $H \neq 0$, the reflection rises as increasing the field until 1 kOe, which was the saturation

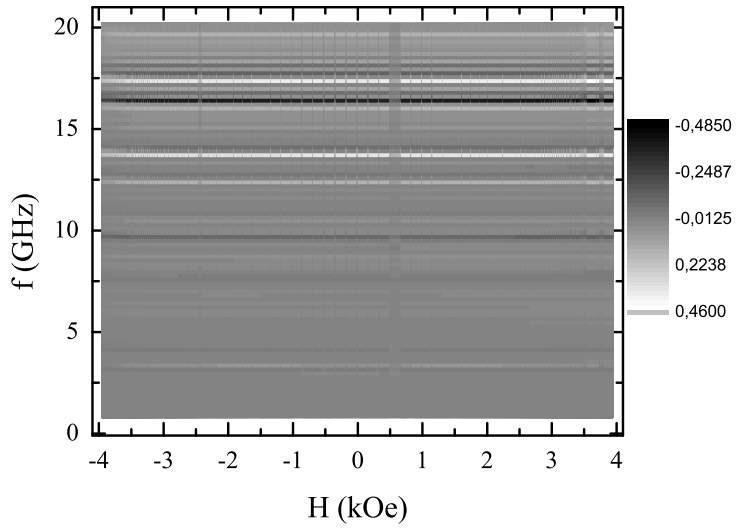

(a) S_{22} bistatic coefficient as a function of the magnetic field without sample. Different resonant frequencies were observed but they did not depend on the field.

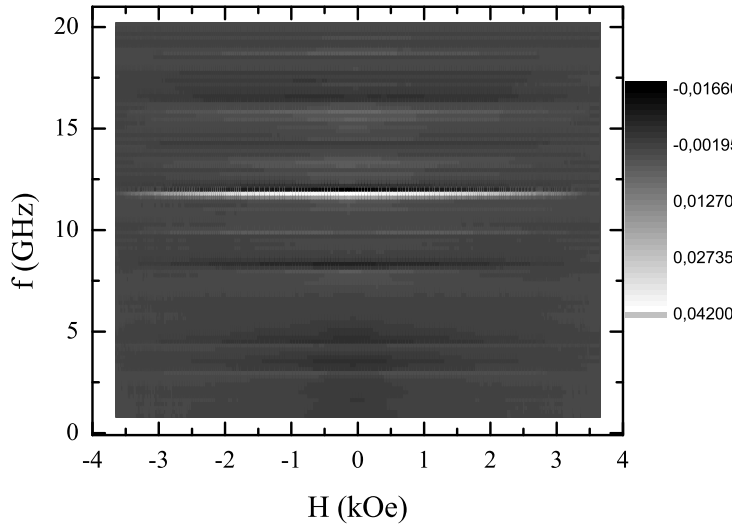

(b) S_{21} bistatic coefficient as a function of the magnetic field without sample. Different resonant frequencies were observed but they did not depend on the field.

Figure 2.12: Measured reflection and transmission in the coplanar line in the absence of sample. The y axis refers to the frequency range studied from 1 to 20 GHz, the x-axis the applied magnetic field, between -3.5 and 3.5 kOe, and the colors refers to the magnitude of the parameter S_{11} or S_{21}, in which black color refers to the minimum value and white color to the maximum.

field of magnetite nanoparticles (see the curve for 3 GHz in figure 2.13), whereas at $H > 1$ kOe the reflection remains constant. Secondly, for $f > 3$ GHz there is also a minimum above 1 kOe, in addition to the minimum at zero field. Since the second minimum (above $f > 3$ GHz) depends on the magnetic field, we conclude that this peak corresponds to the ferromagnetic resonance of the magnetite nanoparticles. A good analysis of this ferromagnetic resonance cannot be done because the field provided by the electromagnet was not enough high to obtain a mapping of the resonant frequency as a function of the applied magnetic field. Furthermore, the broadness of the resonance was due to the amplitude of the size distribution, whose sizes are between 5 and 70 nm. This feature relies upon each particle absorbs resonantly the energy at different frequencies and fields. Therefore, it is expected a larger linewidth for an assembly of nanoparticles than for bulk material.

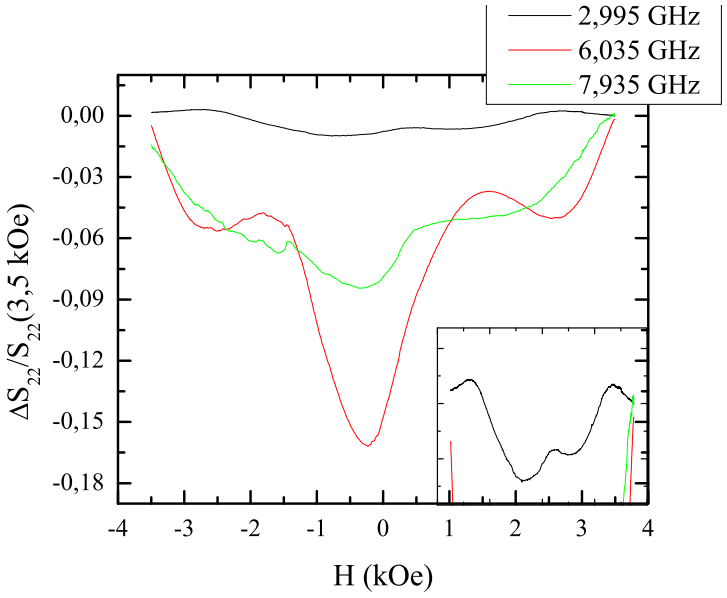

Figure 2.13: Relative variation of coefficient S_{22} between 3 and 8 GHz. For $f < 3$ GHz only a minimum is observed, whereas for $f > 3$ GHz two symmetric minima are observed for fields different to zero. In the inset is plotted the case of 3 GHz.

On the other hand, the peak observed at zero field does not change its position increasing the frequency. As first interpretation, this absorption peak could be related to the magnetoresistance phenomenon showed in section 2.4. However, the electrical resistance reduces increasing the field, that is the sample is a better conductor for highest fields. But the relative variation of the coefficient S_{22} shows another behavior: as the magnetic field increases the bistatic coefficient has a lower variation respect its value at 3.5 kOe. That is, the sample becomes a better conductor at zero field (the electrons can resonantly absorb the electromagnetic

energy) than a higher fields, demonstrating that this phenomenon is not related to the magnetoresistance effect. Therefore, we suggest that the peak at zero field should correspond to the ac-susceptibility of the magnetite nanoparticles. But this ac-magnetic response cannot be attributed to large particles, because they are magnetically blocked as their blocking temperature was higher than 300 K and, then, they cannot follow the ac-electromagnetic field. However, the blocking temperature for nanoparticles of 5.85 nm (size distribution found between 3 and 6 nm) size is:

$$T_B = \frac{KV}{30k_B} = 33K \tag{2.4}$$

where $K = 5.8 \cdot 10^6\ erg/cm^3$ is the anisotropy constant for Fe_3O_4 particles above 100 K, V is the volume for a cubic particle with length 5.85 nm, k_B is the Boltzmann constant and the blocking temperature is computed using the time scale in a SQUID magnetometer $\ln \tau/\tau_m = 30$. Considering an attempt time of $\tau_o = 10^{-11}\ s$, the blocking becomes for an ac-frequency of $f = 1\ GHz$:

$$T_B = \frac{KV}{k_B \ln(\tau_o f)} = 182K \tag{2.5}$$

Moreover, at 8 GHz, the blocking temperature becomes 333 K, and hence being the maximum frequency for which particles of 5.8 nm are in the superpamagnetic state. Nevertheless, in the sample there are nanoparticles having a size lower than 4 nm, for which behaves superparamagnetic until the frequency of 10 GHz, as seen in the S_{22} results. The general behavior of the S_{22} curves, for $f < 10$ GHz, also reflects the magnetization dynamics of the magnetite nanoparticles: At zero field all the superparamagnetic nanoparticles can follow the electromagnetic field provided by the coplanar line. As the DC field increases, the magnetic moment of the particles become fixed along the direction of the DC field, and at the saturation field all the magnetic moments are oriented along the DC field. It is important to remark that this measurement system has a large resolution to detect superpamagnetic particles, because small particles do only represent the 2% of the assembly.

The results of the transmission coefficient (S_{21}, plotted in figure 2.14), are analogous to the reflection measurements. First it can be mentioned that the relative variation of S_{21} coefficient shows a low signal-to-noise ration (SNR) than in the case of reflection measurements, which is a typical fact in such measurement systems. Secondly, the minima observed in the previous measurements are also seen in the relative variation of the coefficient S_{22}: a ferromagnetic resonance is clearly detected above 3 GHz that shifts from 1 to 3 kOe, and a peak at zero field associated with the ac-response of superparamagnetic nanoparticles.

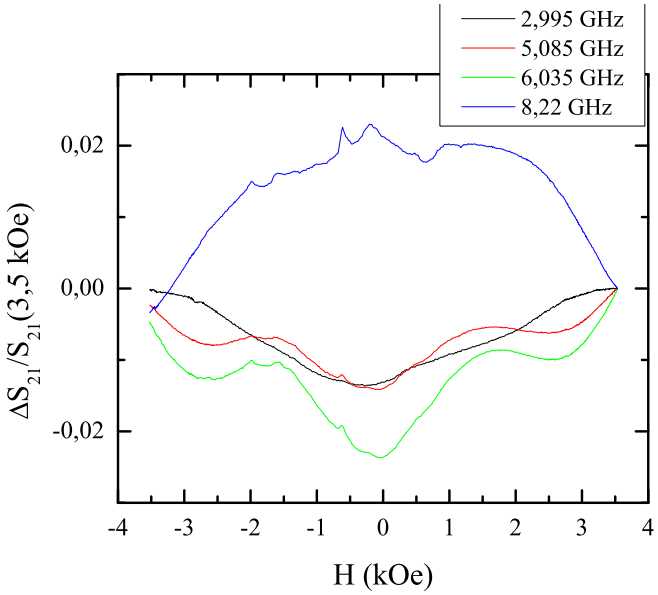

Figure 2.14: Relative variation of the coefficient S_{21} as a function of the magnetic field. Such as the case of the relfection results, it is clearly seen a peak at zero field below 10 GHz, and two symmetric peaks that depend on the magnetic field for $f > 3$ GHz.

To sum up, the ac-susceptibility of magnetite nanoparticles was studied as well as the ferromagnetic resonance at microwave frequencies using a coplanar line. This experimental method is capable to detect superparamagnetic particles and their dynamics with a large resolution in a fast and efficient way.

2.5.3. Results for $La_{0.6}Sr_{0.3}MnO_3$

In figure 2.15 is plotted the reflection data (S_{22}) for $La_{0.6}Sr_{0.3}MnO_3$ particles as a function of the field for low frequencies (between 3 and 8 GHz). The results show a significantly higher absorption of the microwaves than in the case of Fe_3O_4 nanoparticles, although both samples have a similar behavior.

As seen in figure 2.15, for $f < 8$ GHz a minimum at zero field was detected independent on the magnetic field. Increasing the field the reflection rises until 3 kOe. A saturation of the S_{22} coefficient is not clearly seen due to the high saturation field that has the manganite sample (see figure 2.7). Magnetoresitance measurements cannot explain this absorption peak as in the case of magnetite nanoparticles. I turns out that this absorption peak should be related to the ac-susceptibility of the system. But our manganite particles are not single particles (1 μm mean size) not superpamagnetic at room temperature, then we suggest that such ac-response maybe related to the movement of the domain walls between

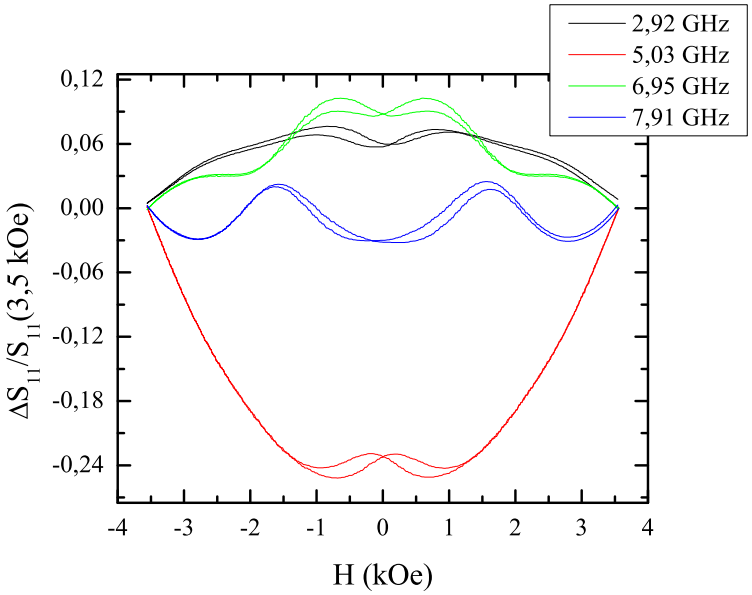

Figure 2.15: S_{22} bistatic coefficient as a function of the magnetic field. For the plotted frequencies an absorption peak is observed, and for $f > 5\ GHz$ two symmetric minima are observed for $H > 2.5\ kOe$.

magnetic domains. It is important to remark that the system has an ac-response until 13 GHz (not shown in figure 2.15), whereas Fe_3O_4 nanoparticles only until 10 GHz.

On the other hand, two symmetric minima above 2.5 kOe (above the saturation field), which shift increasing the field at $f > 7\ GHz$, are clearly seen. We suggest that such resonances are ferromagnetic resonances of the manganite nanoparticles. Figure 2.16 shows the dependence of the resonant frequency on the resonant field. For frequencies below 7 GHz another resonance peak appears in the experiments. As this peak occurs for fields larger than 2.5 kOe it is not possible to make a good mapping of its dependence on frequency.

Relative variations of the bistatic coefficient S_{21} shows the same behavior than coefficient S_{22}: a ferromagnetic resonance, above 2.5 kOe, and a resonance at zero field (see figure 2.17). The peak at zero field is only detected for $f < 13\ GHz$, and the ferromagnetic resonance is observed for $f > 7\ GHz$; such as in the reflection measurements. Therefore, the two set of data agree with these two interpretations.

2.6. Conclusions

In this chapter the interaction between magnetic nanoparticles and microwaves having frequencies between 1 and 20 GHz has been studied using a coplanar line.

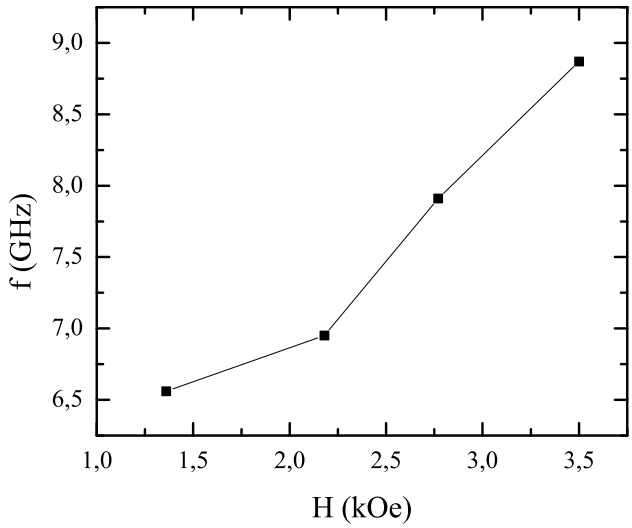

Figure 2.16: Frequency as function of the resonant field, for the detected ferromagnetic resonance.

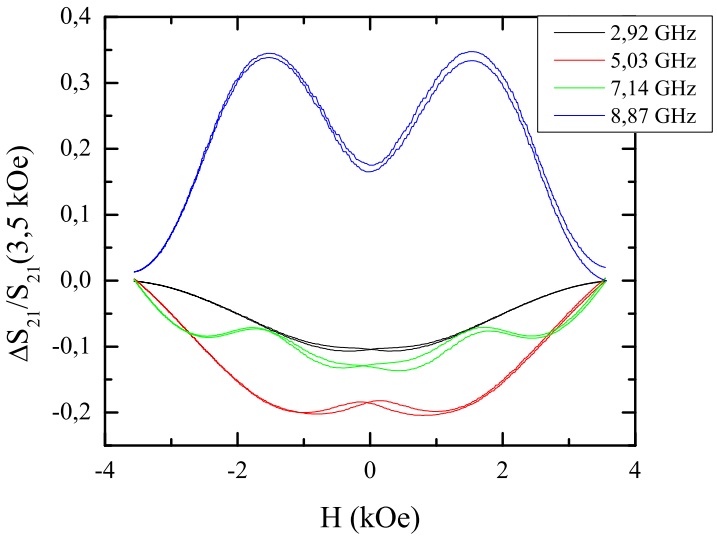

Figure 2.17: Transmission for $Lr_{0.6}Sr_{0.3}MnO_3$ nanoparticles between 1 and 7 GHz. The results reveled a minimum at zero field, whose abosrvance is round a 20% for 6 GHz. In addition, hysteresis is present in the vecinity of zero field.

Two samples were studied, Fe_3O_4 nanoparticles having a mean size of 44 nm and manganite particles, having a mean size of 1 μm.

Structural characterization of ferrite nanoparticles showed a broad size distribution of nanoparticles having a mean size of 44 nm. Nevertheless, magnetic studies confirmed the broad size distribution, in which the computed magnetic volumes showed the presence of small particles having a mean size about $4 - 5$ nm. These results were also confirmed measuring their isothermal magnetization, where a reduction of the coercivity was observed at 300 K, 88 kOe, and a saturation field of 1 kOe; fully compatible with the presence of superparamgnetic and blocked nanoparticles. On the other hand, manganite particles presented a ferromagnetic behavior with a Curie temperature above 370 K. Isothermal measurements showed a paramagnetic signal, and a saturation field higher than 2.5 kOe.

Both samples showed a magnetoresistance phenomenon. In the case of magnetite nanoparticles the electrical resistance reduced a 1% respect to its value at zero field. In the case of manganite particles such reduction was about a 12%.

In the microwave measurements using a coplanar line, both samples had a FMR resonance for fields higher than the saturation field, 1 kOe for Fe_3O_4 nanoparticles and 2.5 kOe for manganite particles. Furthermore, both samples has a minimum in their transmission and reflection data at zero field, which was related to the ac-susceptibility, in other words, the response of the magnetic moment to the oscillating field. In the case, of Fe_3O_4 particles it was associated with small particles presented in the size distribution, lower than 5 nm. Those particles behaved superparamagnetic at room temperature and, then, they can follow the microwave field, until 10 GHz, when their blocking temperature is above 300 K.

In the case of manganite particles also presented an absorption at zero field. Because mean size of manganite particles was 1 μm, they were not superparamagnetic and, hence, the ac-susceptibility was associated with the movement of domain walls. This minimum was observed until 13 GHz being a higher frequency than in the case of magnetite nanoparticles. In addition, it was observed a FRM resonance for field higher than 2.5 kOe, that is above the saturation field.

To sum up, GHz measurements with a coplanar line represent a good methodology to detect, in one measurement, magnetic resonances as well as the spin dynamics at high frequencies. In addition, this technique allow a large sensitivity of SPM particles or domain wall movements. This work can open new technological applications in data storage or in the construction of coherent bits. Finally, fully magnetic characterization at ac-fields using coplanar lines have been demonstrate, where an easy and fast experiments can be performed for NMI or magnetic hyperthermia.

Chapter 3

Magnetic gold nanoparticles

Metallic nanoparticles are a focus of interest in a wide range of scientific fields [44] such as physics, chemistry, and nanoenginering with applications on catalysis [45], medicine [46], optoelectronics [47], high density storage media [48] or single electron transistors [49], [50]. The properties of metallic nanoparticles do only not change due to size effects (such as the magnetic nanoparticles described in chapters 1 and 2) but also owing to the effect of different capping molecules. For example, it has been demonstrated that the optical properties of fine gold nanoparticles can be modified functionalacing their surface with fluorescent molecules [51], with applications in MRI contrast [52] or cancer diagnostics and treatment [53].

Currently research is focused to develop a controllable growing method for metallic particles [54]. For instance, polymers or other capping molecules of the nanoparticles, such as self-assembled monolayers, are a good strategy to achieve these requirements. But those capping molecules tune the surface properties of the particle, for example, the electric properties are changed by the capping [55]. In such systems a charge transfer between the particle and the capping molecule occurs [56], being an important source of new electronic, optical or magnetic properties in metallic particles. In particular, superparamagnetism and ferromagnetism have been reported in metallic particles owing to size effects [57] and the effect of organic functionalized molecules [51], [58] as well.

Size effects are also present in metallic nanoparticles related to the surface-volume ratio [59],[60] (for a gold particle with mean size of 2.5 nm this ratio is about 45% [61], [57]). For instance, the energy of degenerate levels become discretized and the Fermi wavelength of the electrons is comparable with the size of the particle, and hence the electronic properties of such metallic particles depends on the size.

In this chapter three sets of gold nanoparticles capped with two complexes that involved molecular capping agents (1PPS and 3PPS) and contained a sequence of three sulfur groups that attach to the surface gold atoms by noncovalent bonding;

and, the third with tetraoctyammonium bromide (TOAB). The chapter will be structured in the following sections: first, a brief introduction of diamagnetism and Pauli's paramagnetism in metals will be exposed. Afterwards, the three studied samples will be presented as well as their magnetic characterization. Finally, the results will be discussed and the conclusions will be exposed.

3.1. Theoretical background

3.1.1. Diamagnetism

As explained in chapter 1, there are different magnetic states: paramagnetism, diamagnetism, ferromagnetism, and antiferromagnetism. Diamagnetism is caused by the change of the orbital momentum of the electrons inside the atom, when an external magnetic field is applied. According to Lenz's law, for which the magnetic flux enclosed by a current loop is changed (for example by the application of an external magnetic field), an electric current is induced and generates an opposite magnetic field toward the original field. Thus the electronic motion of atoms can change (if they are considered as current loops) in the sense that a magnetic moment will be induced in the direction opposite along the applied field. A quantitative derivation of the diamagnetic susceptibility can be made using the Larmor's precession theorem [62], obtaining the following susceptibility:

$$\chi = -N\frac{e^2}{6mc^2}\sum_{i=1}^{Z}\bar{r_i^2} \tag{3.1}$$

where N is the density of electrons per unit volum, e is the electron charge, m the electron's mass, c the speed of light, Z the atomic number and $\bar{r_i^2}$ is the mean square distance from the atomic nucleus. The main conclusions from equation 3.1 are: the diamagnetic susceptibility is always negative, and does not depend on temperature, as represented in figure 1.2. In fact, all matter is diamagnetic in the sense that any system is formed by atoms with fully orbitals, and hence any applied magnetic field generates a diamagnetic response. Furthermore, the diamagnetic susceptibility does not depend on the spin or the total angular momentum of each atom or molecule, and, then any magnetic phenomena related to the spin, the orbital angular or the total angular momentum should be separated from the diamagnetic susceptibility. A typical value for the diamagnetic suscteptibility is round 10^{-5} at 300 K, being the lowest contribution in a magnetic material.

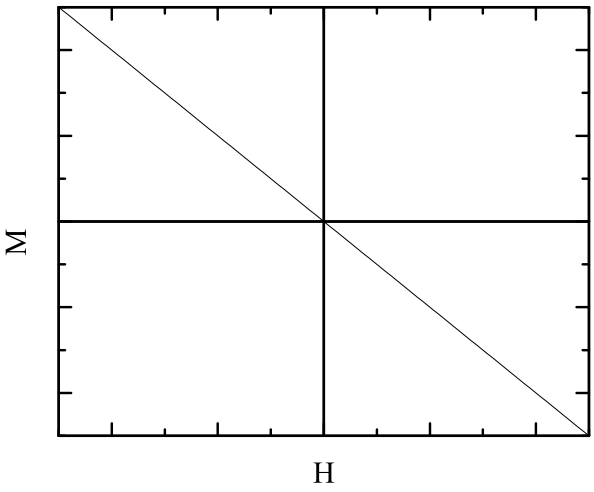

Figure 3.1: Magnetic responses of a diamagnetic material as a function of magnetic field. The diamagnetic signal does not depend on the temperature neither the spin of the material, becoming a opposite signal along the field.

3.1.2. Magnetism in metals

For the majority of solid materials without ions with non-zero magnetic moment, the description provided by atomic diamagnetism is sufficient to understand their magnetic behavior. Nevertheless for metals, the electrons in the conductance band contributes to the total magnetic susceptibility, because they behavior is totally different such as the valance electrons. The independent electrons approximation is sufficient for the majority of metals, such as the case of gold, to deduce the contribution of conducting electrons to the magnetic susceptibility. In this case [62], [63], it is not taking into account the orbital motion induced by the magnetic field in the electrons. In other words, it is only considered that the electrons have a magnetic moment due to their spins.

The contribution for each electron to the total magnetic density in the presence of a magnetic field $\vec{H}$ is with the magnetic moment per unit volume $\frac{-\mu_B}{V}$, if the electron spin is parallel to the field, or contributes with $\frac{\mu_B}{V}$ if the spin is aligned antiparallel. If the density of electrons in the state parallel to the field is n_+ and the antiparallel n_-, the total magnetic density becomes:

$$M = -\mu_B \left(n_+ - n_-\right) \tag{3.2}$$

Let us assume $g_\pm\left(\epsilon\right)$ the number of electrons with one of the two spins orientations per volume unit in the energy range between ϵ and $\epsilon + d\epsilon$. In the case without

field, $g_{\pm} = \frac{1}{2} g(\epsilon)$, where $g(\epsilon)$ is the ordinary density of levels. As counterpart, in the presence of a field the energy is shifted in $\pm \mu_B H$, depending on the orientation between the electronic spin and the field, respect its zero value. Consequently, the density of electrons at the energy ϵ by the field is the same than the density of levels without field with the energy $\epsilon \mp \mu_B H$. This feature allows write the density of levels as a function of the ordinary density and the number of electrons of each spin is given by:

$$n_{\pm} = \int d\epsilon g_{\pm}(\epsilon) f(\epsilon) \tag{3.3}$$

where $f(\epsilon)$ is the Fermi-Dirac distribution. For metals the basic variations on $g(\epsilon)$ occurs at the scale of ϵ_F, the Fermi level, owing to the energy shift $\mu_B H \approx 10^{-4} \epsilon_F$ at fields of 10^4, and hence the density of states, $g_{\pm}$ can be developed around $g(\epsilon)$. Taking into account this conclusion, equation 3.3 becomes:

$$n_{\pm} = \frac{1}{2} \int d\epsilon g(\epsilon) f(\epsilon) \mp \frac{1}{2} \mu_B H \int d\epsilon g'(\epsilon) f(\epsilon) \tag{3.4}$$

where $g'(\epsilon)$ comes from the expansion of $g_{\pm}(\epsilon) = 1/2 g(\epsilon \pm \mu_B H)$. Since the modifications are around the Fermi level, the chemical potential can be expressed as $\mu = \epsilon_F \left[1 + O\left(\frac{k_B T}{\epsilon_F}\right)^2\right]$. In this way, at $H = 0$ the chemical potential takes the same value that the Fermi energy. Therefore the magnetic density defined in equation 3.2 is:

$$M = \mu_B^2 H \int g'(\epsilon) f(\epsilon) d\epsilon = \mu_B^2 H \int g(\epsilon) \left(-\frac{\partial f}{\partial \epsilon}\right) d\epsilon \tag{3.5}$$

integrating by parts in the term of the right. Finally, for zero temperature $\frac{\partial f}{\partial \epsilon} = \delta(\epsilon - \epsilon_F)$, where δ is the Dirac function. Substituing in equation 3.5:

$$M = \mu_B^2 H g(\epsilon_F) \tag{3.6}$$

Equation 3.6 is called Pauli Paramagnetism. As first interesting fact, the approximation for zero temperature works for $T \neq 0$, because the corrections in $\frac{\partial f}{\partial \epsilon}$ are of the order of $\left(\frac{k_B T}{\epsilon_F}\right)$, and hence the deduced magnetization is valid for temperatures below $10^4\ K$, and it turns out that Pauli paramagnetism is independent on the temperature. In the case of free electrons, it takes the form:

$$\chi_{Pauli} = \left(\frac{\alpha}{2\pi}\right)^2 (a_o k_F) \tag{3.7}$$

being $\alpha = \frac{e^2}{\hbar c} = \frac{1}{137}$. The scale of Pauli paramagnetism is the same than atomic diamagnetism, and then smaller than currently ion paramagnetism. This reduced

value is due to Pauli's exclusion principle: Pauli's repulsion is much efficient than thermal fluctuations (paramagnetism) in disaligned the magnetic moments with the field.

Finally, if one consider the interaction of the electrical charge with the field, that is the orbital motion of the electrons by the interaction with the field, is founded Landau diamagentism. However, this diamagnetic contribution is half of Pauli paramagnetism.

Therefore, there exist three contributions in the magnetic susceptibility of metals: atomic diamagnetism, Pauli paramagnetism and Landau diamagnetism.

3.2. Gold samples

Gold atoms have the electronic structure of [Xe] $4f^{14}5d^{10}6s^1$ and their electrical properties, in bulk material (whose crystallographic structure corresponds to a face centered cubic, figure 3.2), come from the electron gas model of 6s band electrons, because of 5d electrons are below the Fermi level. In addition bulk gold is a diamagnetic material with a susceptibility of $-1.42 \cdot 10^{-7}\ emu\ g^{-1}Oe^{-1}$. It has been reported that gold nanoparticles capped with different thiols groups show a ferromagnetic behavior for particles below 3 nm [64]. Thiol molecules form a strong bond where a charge transfer from surface gold atoms to the sulfur atom present in the binding molecule. This feature generates a great interest to study gold nanoparticles aiming to understand the mechanism that give these properties, and the wide range of applications that open this new experimental fact. Because gold is biocompatible, and combined with the interest in medicine of magnetic nanoparticles, magnetic gold nanoparticles are a promising material with applications on ferrofluids [65], in molecular imaging [66], tumor targeting and hyperthermia [67].

The studied gold nanoparticles in this chapter were synthesized by chemical methods by the group of Professor R. Ziolo in the Investigation Center of Applied Chemistry in Mexico. Three sets of gold particles were synthesized in order to investigate the mechanism for the functionalization of the particles. Two sets of gold nanoparticles were carried out on the presence of the monomer poly(phenylenethynylene) and the molecule 2-S-thiodiethyl-bis(benzencarbothiolate) (2-sq3S) (in this text named sample Au 1PPS) and with other complex with the same flexible part that the Au-1PPS complex named Poly(Phenylene Ethynylene) (pPET3OC12-sqS) (in this text named Au 3PPS, see figure 3.3). These two chains are connected to the gold particle by a non covalent bond. In addition, a third chemical reaction was performed to obtain the particles in absence of the monomer, using tetraoctylammonium bromide (TOAB and the sample was named Au TOAB), it getting stable particles. TOAB molecule was also attached to the gold particles by a Au-S bond.

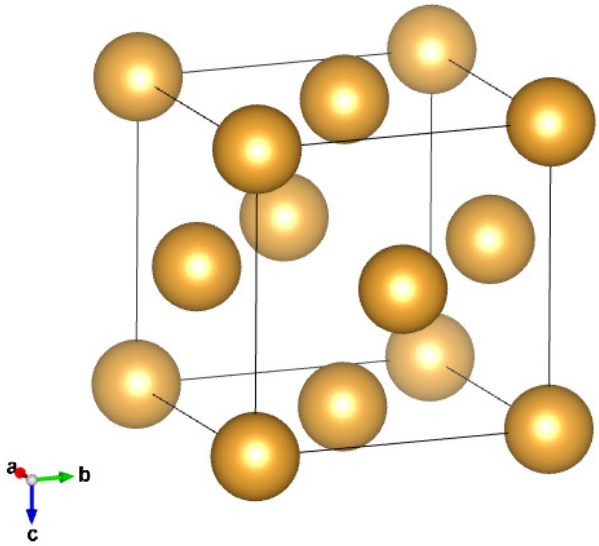

Figure 3.2: Gold crystallographic structure.

The bond scheme with the particle for the three sets are plotted in figure 3.4(a) for Au 1PPS, 3.4(b) Au 3PPS and 3.4(c) for Au TOAB.

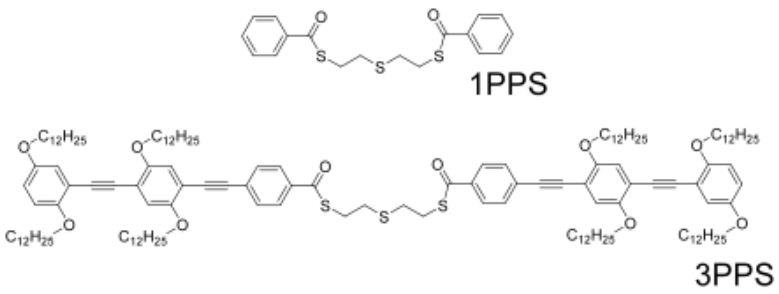

Figure 3.3: Capping molecules used on samples Au 1PPS and Au 3PPS. The two molecules have the same flexible part, and bind to surface gold atoms by a noncovalent bond.

The synthesis of gold particles using the different capping molecules suggested, for the chains 1PPS and 3PPS, stable and functionalized particles. On the other hand, the stabilization of the particles with the TOAB molecule only was possible by the combination of the monomer and the TOAB molecule, but the surface interaction only was by the TOAB molecule, which also interacts with the monomer.

High resolution TEM images have been obtained in the group of professor R. Ziolo, in order to characterized the size distribution of gold nanoparticles. In

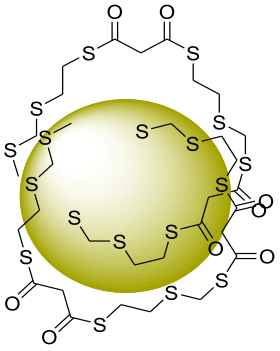

(a) Bond scheme of gold particles and the monomer 2-sq3S.

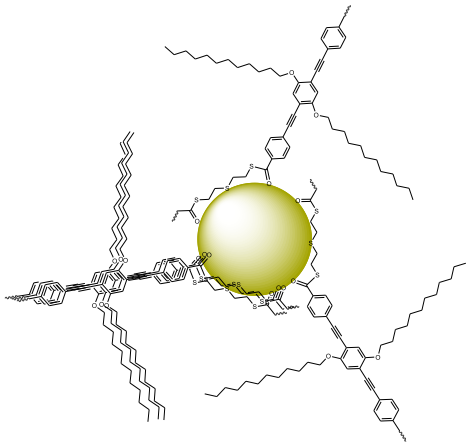

(b) Bond scheme of gold particles and the trimer pPET3OC12-sqS.

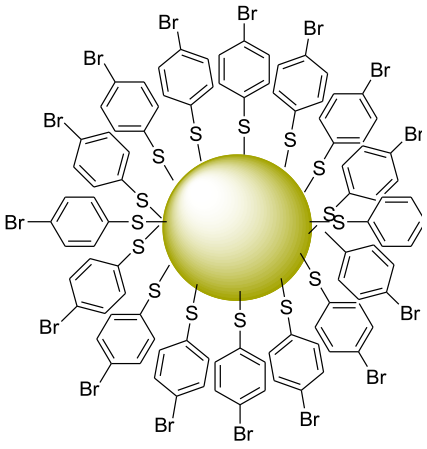

(c) Bond scheme of gold particles and the TOAB molecule. In addition, TOAB molecule was also bonded to a polymeric matrix.

Figure 3.4: Bond scheme for the three synthesized set of gold nanoparticles.

figures 3.5(a) and 3.5(b) are shown two TEM images for samples Au 1PPS and Au TOAB. For sample Au-1PPS was obtained a broad size distribution with mean size of 6 nm, and the sizes of the particles was compressed between 2 and 10 mm. TEM images also reveled a pyramidal hexagonal morphology with (1 1 1) and (2 0 0) growing planes. In the case of Au 3PPS another hexagonal pyramidal growing was founded but along the (2 2 2), (1 1 1) planes, with mean size round 10 nm, but with a large broadness size distribution. Au-TOAB nanoparticles showed a size distribution centered at 3.1 nm, and was the set of particles with thiner size distribution (maximum size at 5 nm).

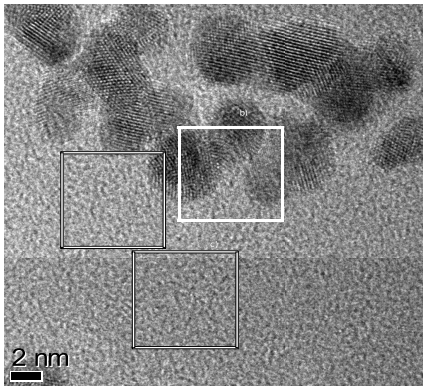

(a) TEM image for sample Au 1PPS. The results show a broad size distribution with mean size of 6 nm

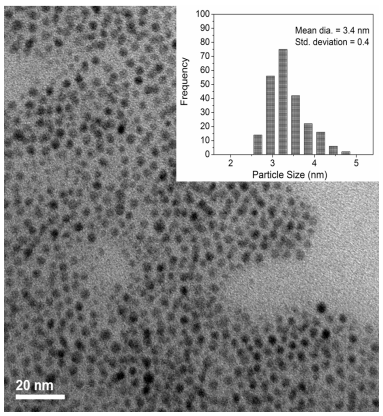

(b) TEM image for sample Au TOAB. In this case the particles have a thin size distribution centered at 3.2 nm.

Figure 3.5: Representative TEM images for gold nanoparticles capped with the 2P-sq3S and TOAB molecule.

Finally, Surface Plasmon Resonance (SPR) was also conducted in the group of Professor Ziolo (see figure 3.6(a) and 3.6(b) for Au-3PPS and Au-TOAB complexes) , where a peak at 540 nm was detected for the three samples. This absorption peak is related to oscillating movement of surface quasi-free electrons in the gold particles. However the intense of the peak for sample Au-TOAB was smaller than the two other complexes. This discrepancy might be attributed to the nature of the bond between the surface of the particle and the capping molecule. The covalent bond formed by the TOAB molecule and the surface atoms of gold gen-

erates a charge transfer from the 5d electron band to the sulfur atom. These low value in comparison with the two other complexes (where the bond nature is not covalent) suggests a localization of surface electrons. In addition, some additional resonances were observed for the complex Au-3PPS that were associated with the capping molecule.

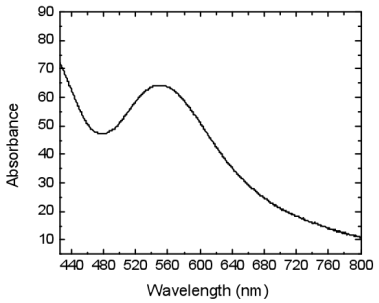

(a) Surface Plasmon Resonance for sample Au-3PPS.

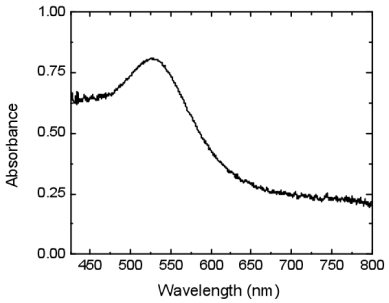

(b) Surface Plasmon Resonance for sample Au-TOAB.

Figure 3.6: Surface Plasmon Resonance for samples Au-3PPS and Au-TOAB respectively. The two spectras show a resonance at 540 nm, but in the case of sample Au-TOAB the intensity of the absorption peak is lower than the absorption peak for sample Au-3PPS. This fact indicates a charge transfer from surface gold atoms and the sulfur atom of the TOAB molecule.

3.3. Experimental set-up

Magnetic measurements were performed using a SQUID magnetometer and a Reciprocating Sample Option (RSO) measurement kit for 10^{-7} emu sensitivity. This selection stem from the lower signal expected in the three samples. For this reason to smear out other magnetic signals, the sample holders were magnetically characterized before the samples. They consisted of a 29 mg polycarbonate capsules suspended by a plastic straw. The capsules were sewed to the straw using a copper wire (figure 3.7). Taking into account the materials that form the sample holder, the expected magnetic signal was diamagnetic.

The magnetic characterization of the samples and their containers were done by performing ZFC-FC studies, TRM, and isothermal magnetization measurements. The ZFC-FC protocol was performed as follows: first, the samples were cooled down to the lowest temperature ($T = 5\ K$) at zero field; afterwards the measuring field was applied (1 kOe) and the magnetization was recorded as the sample's temperature was increased at constant sweep rate of 1 K/min. The FC protocol only differed from the ZFC in that the measuring magnetic field was applied before

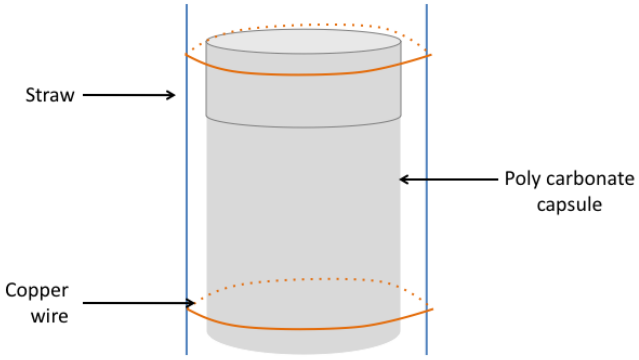

Figure 3.7: Sample holder used for the experiments.

cooling the sample. The reason for applying a high field was to obtain a measurable signal from the system, because the samples and the sample holders presented a magnetization lower than 10^{-5} emu.

Thermal Remanent Magnetization (TRM) was carried out on the following way: first a 50 kOe magnetic field was applied at 300 K and then we field-cooled the sample until 5 K. At this low temperature the field was switched off and the remanent magnetization was measured in the temperature range between 5 and 300 K.

Finally, isothermal magnetization studies of the samples have also been performed at 5, 100, 200 and 300 K. The protocol was as follows: first, the sample was cooled down without any applied field to the desire measurement temperature. Afterwards, the magnetization was recorded as a function of the magnetic field between -50 and 50 kOe.

3.4. Data analysis

The data acquisition and analysis was common for the three samples and their sample holders, and for this reason all are commented in this section. Since the sample holders and the samples were magnetically characterized in the same way, we refer to the characterization of the sample holders as measurements of type A, and the raw data of the experiments of the samples, measurements of type B. The general data treatment applied in all the experiments consisted of subtract the

magnetization of the sample holder (measurements of type A) to the magnetization of the holder with the sample (measurements of type B), in order to obtain the pure signal of the gold nanoparticles. In this text, we named these last measurements of type C.

In the three experiments (ZFC-FC, hysteresis loops and TRM) measurements of the type A, B and C were performed. The results of measurements C suggested, in the three experimental protocols, a superposition of a diamagnetic and positive signal, where the diamagnetic component was associated with the intrinsic diamagnetism from gold. Only in the case of isothermal magnetization experiments intrinsic gold diamagnetism was corrected for measurements of type C, whereas in TRM and ZFC-FC experiments the information provided by measurements of type A and B was sufficient. In the case of the hysteresis loops, the intrinsic diamagnetism of measurements C was subtracted by a linear fit of the data in the field range between 20 and 50 kOe. As diamagnetism does not depend on the temperature, the correction was done by the mean of the extracted slopes in all the temperature range.

3.5. Results

3.5.1. Au 1PPS

The first studied sample was gold Au 1PPS capped with the molecule 2-sq3S. The complete characterization of this sample was not possible because only 5 mg of sample was available, resulting on a signal with a large signal-to noise-ratio (SNR). ZFC-FC measurements of type A (empty sample holder) and B (holder containing the Au 1PPs) are plotted in figure 3.8. As seen in the figure, Au 1PPs has a diamagnetic signal larger than that of the sample holder in concordance with the metallic nature of gold. Furthermore, at low temperatures the sample shows a large irreversibility than the sample holder.

Results corresponding to measurements of type C are plotted in figure 3.9. The resulting ZFC magnetization increases as a function of the temperature, 5 K, until 100 K, remaining constant for $T > 100$ K. The FC curve does not change with the temperature and has an irreversible temperature round 150 K. FC data below 50 K are not shown because of their SNR.

Figures 3.10 and 3.11 depict measurements of type B of the TRM and its derivative respectively. The results show that the remanence magnetization of the system followed down in the whole temperature range. In this case, measurements of type C were not necessary because the measurements of type B directly were positive. This fact relies upon the unique dependence on the temperature was the positive contribution to the magnetic susceptibility (the dependence on

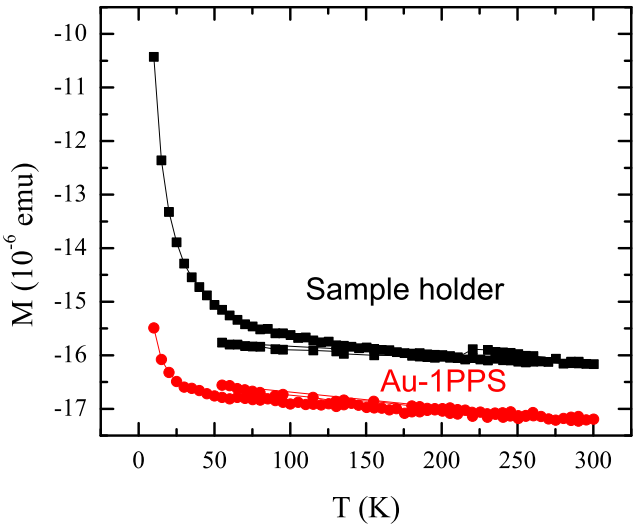

Figure 3.8: ZFC-FC data from sample Au-1PPS and its sample holder (type A and B respectively). The results show that the gold nanoparticles were more diamagnetic than the sample holder.

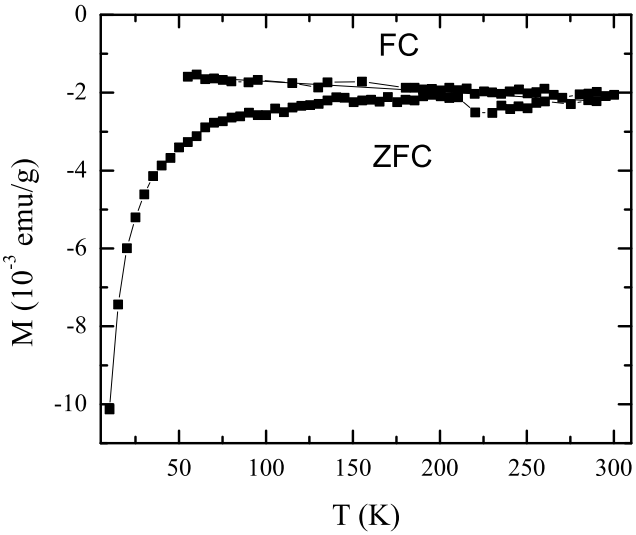

Figure 3.9: Results of type C for the ZFC-FC for sample Au-1PPS. The magnetization is a superposition of a diamagnetic signal and a characteristic thermal activated phenomenon.

temperature of measurements of type A was lower than for measurements of type B). Consequently, in figure 3.10 is observed the remanence magnetization of the

positive part of the susceptibility, and thus a positive sign for the magnetization.

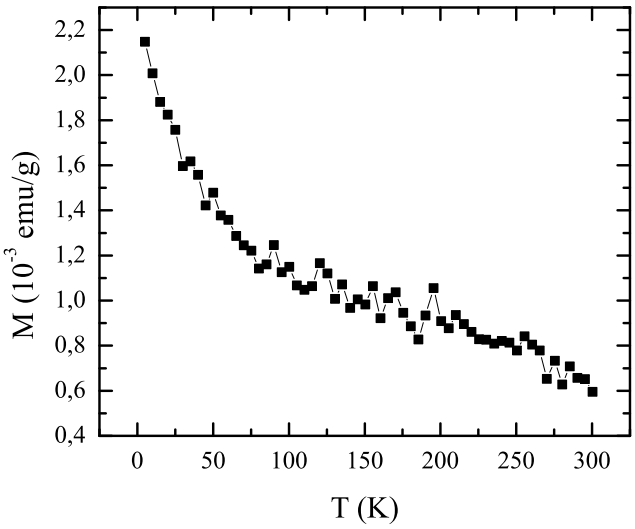

Figure 3.10: TRM data for measurements of tpye B for sample Au 1PPS. In the figure is clearly seen the evolution of the remanent magnetization as a function of the temperature.

The derivative of TRM data was computed and smoothed due to its SNR (figure 3.11). As seen in figure, the magnetization of the sample peaks at 5 K confirming the results of ZFC-FC measurements. Consequently, the most plausible explanation to the behavior of the ZFC-FC and TRM magnetization curves is that the system follows a thermal activation process over anisotropy barrier energies with an average barrier height of $KV/k_B = 150\ K$. Therefore, gold particles have a mean blocking temperature around 5 K.

Isothermal magnetization measurements of type B are shown in figure 3.12. The results were consistent with the ZFC-FC, whose results demonstrate that the sample has a larger diamagnetic component than the sample holder. For this reason when the signal of the sample holder was subtracted, the sample remained diamangetically (measurements of type C). This feature relies upon intrinsic diamagnetism of gold nanoparticles was larger than any signal in the system. To estimate correctly the diamagnetism of the sample, and taking into account that diamagnetism does not depend on the temperature, the data were fitted to a straight line in the field range between 20 and 50 kOe. The diamagnetic susceptibility founded with this method was $2.6 \cdot 10^{-8}\ emu/Oe$ for all the assessed temperatures. Hence, the curves in figure 3.12 were obtained subtracting a linear magnetization using the computed susceptibility.

The results (they plot in figure 3.12) show that the magnetization, between

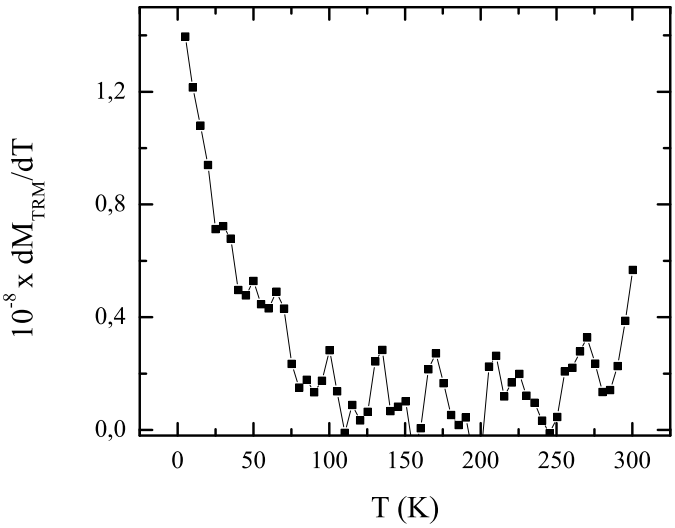

Figure 3.11: Derivative of the TRM magnetization data. The results show a peak at 5 K, which can mean a blocking temperature round 5 K.

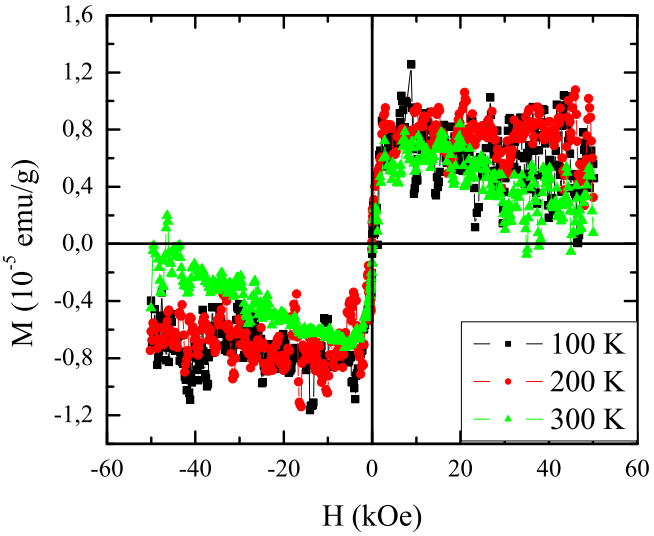

Figure 3.12: Measurements of type C for sample Au 1PPS between 100 to 300 K.

100 and 300 K, do not depend on the temperature. This fact is compatible with the results obtained for the ZFC-FC experiments, for which above 50 K the magnetization remained constant as a function of the temperature. As interesting

remark, the saturation field was below 10 KOe with a saturation magnetization of 10^{-5} emu/g. The constant linear magnetization at low fields for all the temperature range is attributed to Pauli's paramagnetism that is independent on the temperature.

It turns out that the system below 5 K should behave such as ferromagnetic nanoparticles only if the peak observed in the previous measurements is a blocking temperature. On the other hand, above 5 K should behave superparamagnetically. However, in the ZFC-FC and hysteresis loops measurements the system is independent on the temperature. As counterpart, if the system behaves superparamagnetically some dependence on temperature should be detected, which is not the case, supporting the hypothesis for Pauli's paramagnetism. As the experiments for low temperatures, 5 K, failed, it was not possible obtain in a large temperature range the behavior of the system, to support this interpretation. Nevertheless, we suppose that the isothermal curve for $T < 50$ K is for ferromangetic particles.

3.5.2. Au 3PPS

In the case of gold nanoparticles capped with the molecule pPET3OC12-sqS, it was used 46 mg of sample allowing to obtain better signals than in the previous sample. Figure 3.13 depicts the ZFC-FC results for measurements of type A and B. Like in the previous case, the results show that gold nanoparticles has a large diamagnetic component than the holder.

ZFC-FC results for measurements of type C are shown in figure 3.14, where it is observed an overlap between a diamagnetic and a paramagnetic signal. For all the measuring temperature range, the magnetization decreases following a $1/T$ law. Remarkably, the system presents an irreversible behavior between the ZFC and the FC curves even at 300 K.

These results encouraged us to compute the energy barrier distribution using equation 1.25 (see figure 3.15) from the ZFC-FC magnetization data. The results show a peak at 5 K that can be interpreted as a blocking temperature. Therefore, taking into account these results the height of the barrier is about 150 K, which was similar than for Au 1PPS sample.

TRM results and its derivative are represented in figures 3.16 and 3.17, respectively. The remanence magnetization decreases as a function of the temperature, in concordance with ZFC-FC measurements. In addition, the derivative of TRM has a peak at 5 K also in concordance with the results of the ZFC-FC magnetization.

Figure 3.18 depicts the results for measurements of type A and B for the hysteresis loops experiments performed for sample Au 3PPS. As seen in the figure, the sample has a larger diamagnetic component than the sample holder, such as the ZFC-FC results and the previous analyzed sample. Intrinsic diamagnetic susceptibility of the sample was corrected using the same method for sample Au

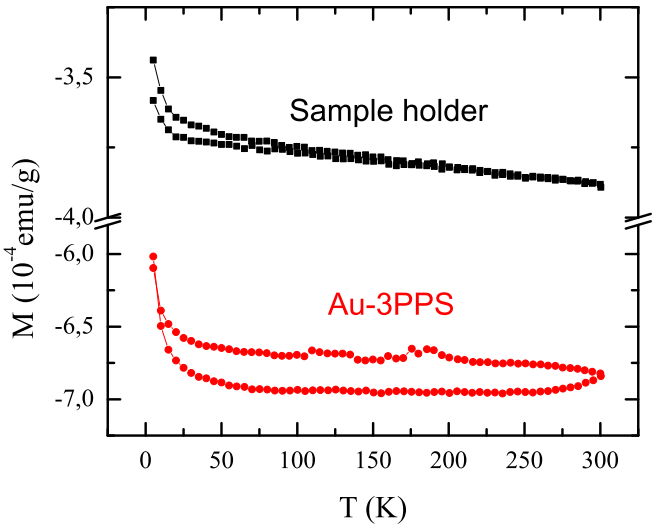

Figure 3.13: ZFC-FC for gold nanoparticles capped with the molecule pPET3OC12-sqS and its sample holder (measurements of type A and B). The data suggested that gold nanoparticles behave more diamagnetically than the sample holder.

1PPS. The obtained diamagnetic susceptibility was $2{\cdot}10^{-8} emu/Oe$, such as sample Au 1PPS.

The results for measurements of type C are represented in figure 3.19. For $T = 5\ K$ the sample shows hysteresis for high fields, which corresponds to a ferromagnetic phase. Nevertheless, for low fields a linear relationship between magnetization and the magnetic field is also observed in which neither hysteresis nor coercivity is detected. This reduction of the coercive field, at $T = 5\ K$ is associated with Pauli's paramagnetism that reduces dramatically the coercivity of the ferromagnetic phase. For $T > 100\ K$ the hysteresis seen at 5 K disappears but the paramagnetic contribution at low fields remain with the same slope that at 5 K: $2 \cdot 10^{-10}\ emu/Oe$.

Finally, the results for $T = 300\ K$ at low fields were equivalent that those at 100 K: a paramagnetic signal with the same slope that the other explored temperatures. Nevertheless, at high fields the magnetization follows up until the saturation field that is higher than 50 kOe. This discrepancy maybe due to the fact that the measurements at 300 K were not correct. On the other hand, we consider correct the results at low fields (below 1 kOe) because the slope of the linear part coincides with the slope of the temperature- independent paramagnetism.

As main conclusion, the behavior of sample Au 3PPS was similar than for sample Au 1PPS, a peak in the derivative of the ZFC-FC magnetization data.

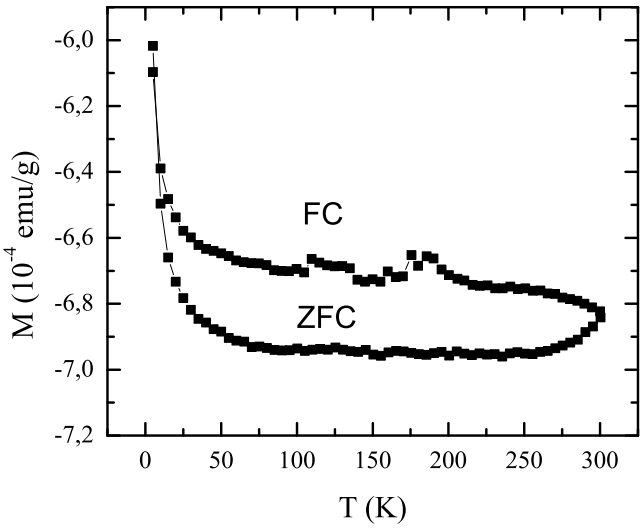

Figure 3.14: Measurements of type C for the ZFC-FC for Au-3PPS. The results suggest that the magnetization of the particles decreases following a $1/T$ law. Moreover, hysteresis was detected in the whole range of measurement.

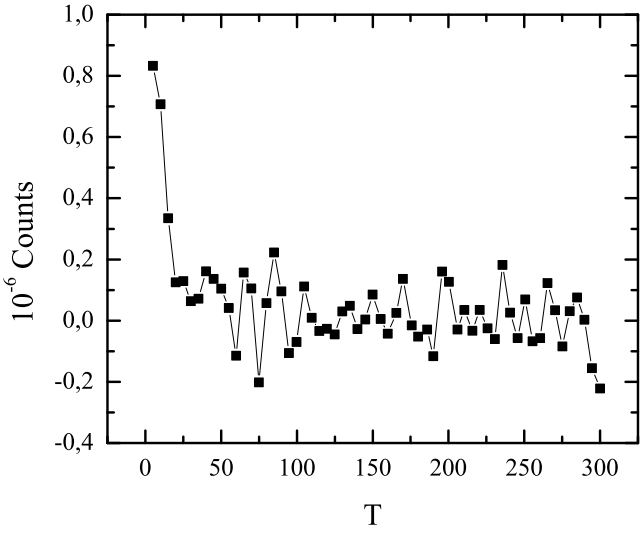

Figure 3.15: Computed energy barriers for sample Au-3PPS. The results show small energy barriers, which peaked at 5 K.

In the two cases Pauli's paramagnetism is observed above the peak, and below

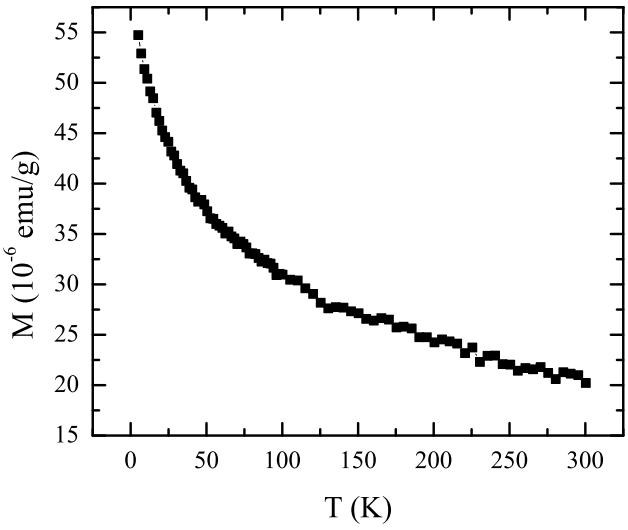

Figure 3.16: TRM magnetization for measurements of type B for sample Au 3PPS. The remanence magnetization diminish decreasing the temperature, such as a thermal activation process.

a ferromagnetic phase (it only observed for sample Au 3PPS). The most plausible explanation for the discrepancy of the ZFC-FC magnetization curves and the isothermal result at 300 K can be that the energy barriers in the system, and the ferromagnetic coupling in the particles were different (it being lower for Au 3PPS). These differences can only be to the effects introduced by the capping molecule.

3.5.3. Au TOAB

The last analyzed sample was 13 mg of gold nanoparticles capped with the molecule tetraoctilamonium bromier. ZFC-FC magnetization data of type A and B are plotted in figure 3.20. The results show the same behavior than the previous samples, that is a larger diamagnetic signal than the holder.

Figure 3.21 depicts the results for measurements of type C. In this case, the results are similarly to the ZFC-FC obtained for sample Au 1PPS. The ZFC increases from the initial temperature, $T = 5\ K$, until 100 K , at which the magnetization remained constant until 300 K. In the case of the FC curve, the magnetization data remain constant for the whole temperature range. Finally, the irreversible temperature is round 100 K.

To go deeper on the understanding of this phenomena, we computed the derivative of the difference between the FC and the ZFC as a function of the temperature,

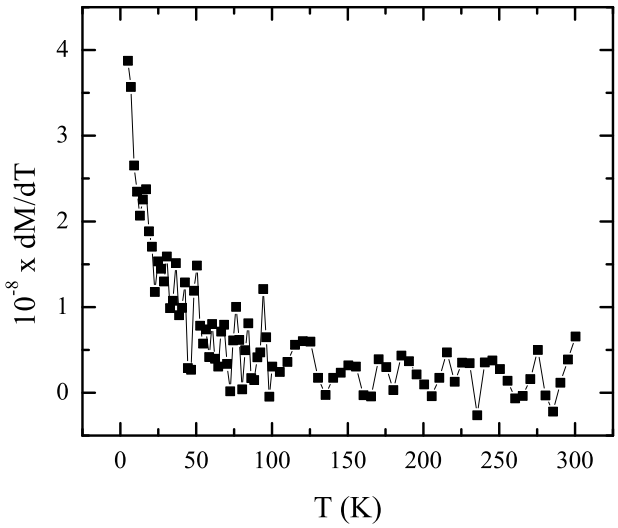

Figure 3.17: Dependence of the derivative of TRM magnetization data on the temperature. The results show a peak at 5 K in concordance with ZFC-FC results.

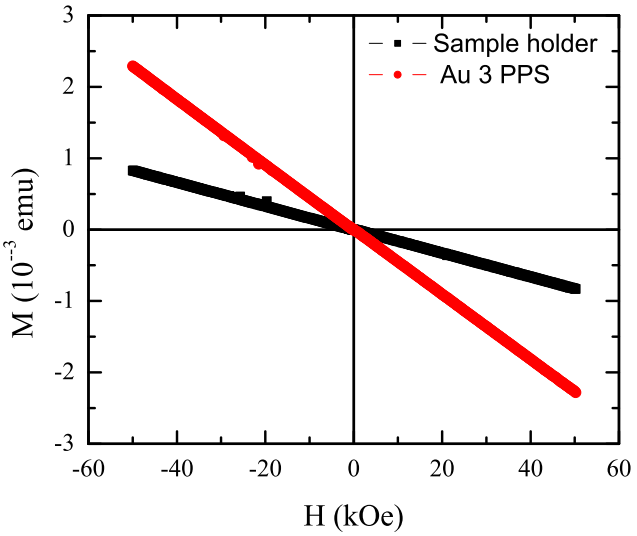

Figure 3.18: Hysteresis loop of type A and B for sample Au 3PPS at 300 K. As seen in the figure the magnetic signal of the sample was larger than the sample holder.

as shown in figure 3.22. In the figure, a peak at 5 K is observed that means an energy barrier with a mean height of 150 K.

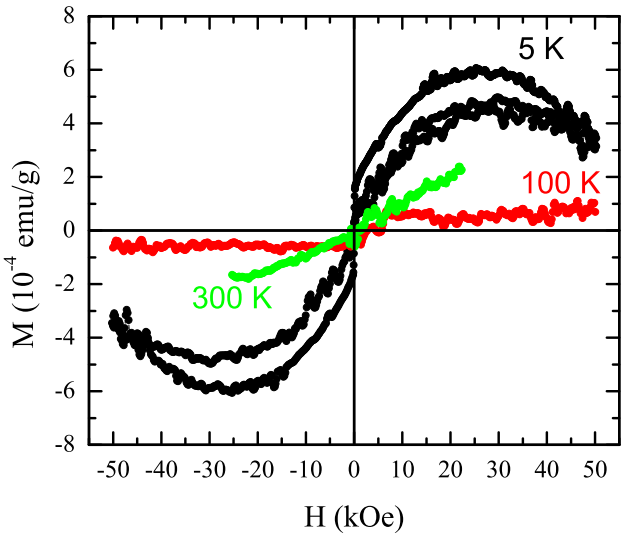

Figure 3.19: Hysteresis loops at 5, 100, and 300 K for gold nanoparticles capped with the triomer.

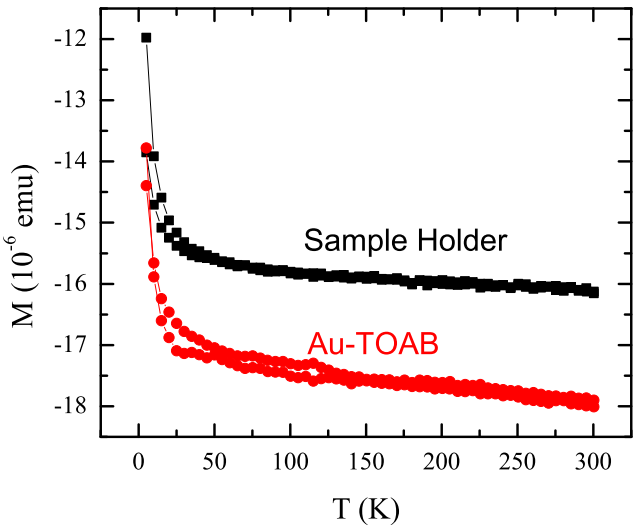

Figure 3.20: ZFC-FC for sample Au TOAB and its container (measurements of type A and B). As the previous sample, gold nanoparticles had a larger diamagnetic signal than the sample holder.

In the case of TRM data for measurements of type B (represented in figure 3.23), the magnetization decreases for the whole temperature range and shows an

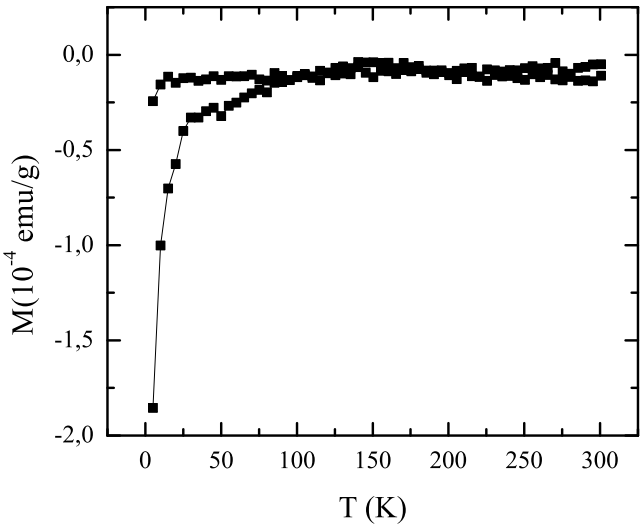

Figure 3.21: ZFC-FC results for measurements of type C for sample Au TOAB. In the figure is clearly seen a thermal activated process.

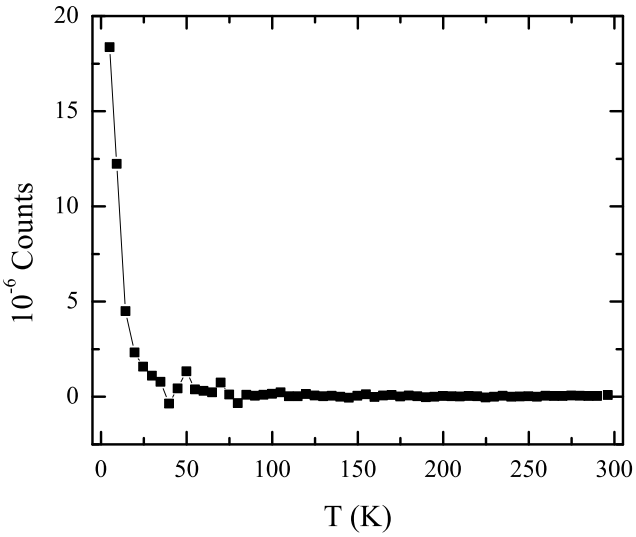

Figure 3.22: Extracted barrier energy distribution from the ZFC-FC data. A peak is clearly seen at 5 K

inflection point below 50 K. This feature can be a clear signature of a distribution of energy barriers, as seen in the derivative of TRM data, in figure 3.24.

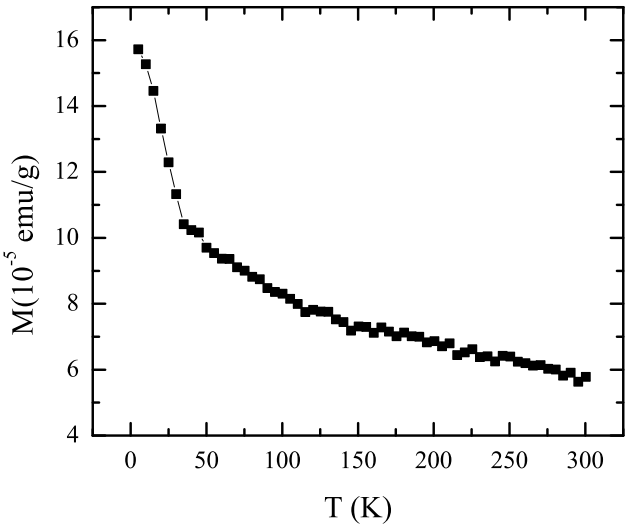

Figure 3.23: TRM magnetization data of type B for sample Au TOAB. In the figure is observed an inflection point at 50 K,

The derivative of the remanence magnetization shows a peak at 20 K (see figure 3.24) that corresponds to the inflection point in the ZFC-FC data. However, the peak extracted from its derivative was at 5 K. Since TRM was a direct measurement, we consider correct the peak founded in its derivative, although the computed energy barrier distribution from the ZFC-FC gave another result. The incorrect value of the derivative of the difference of the ZFC-FC can be by the noise of the measurement that affects to the result. Consequently in this sample, a barrier distribution was clearly seen, with a mean blocking temperature at 20 K, and a mean barrier height of 3000 K.

The high temperature peak in the Au TOAB sample encourage us to perform isothermal experiments in the region round 20 K. For this reason, hysteresis loops studies were carried out at low temperature, between 3 and 100 K. as seen in figure 3.25.

At low temperatures the hysteresis loop shows the superposition of a ferromagnet, at high fields, and a paramagnet, at low fields, such as the other samples. The effect of the paramagnetic phase on the ferromagnetic behavior is a dramatic reduction of the coercivity field, being lower than 100 Oe at $T = 5$ K. In addition , the paramagnetic signal is independent on the temperature, and has the same slope for all the temperatures (Pauli's paramagnetism). As interesting remark, the magnetic saturation reduces as a function of the temperature until 20 K (peak observed in the derivative of TRM measurements), and above remains constant.

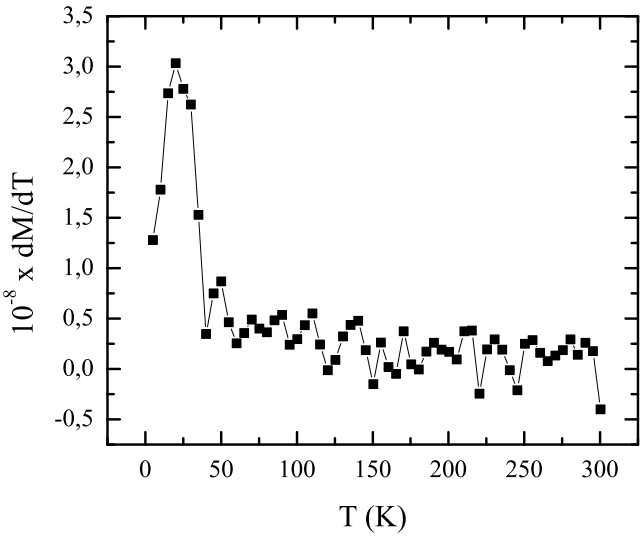

Figure 3.24: Derivative of the TRM magnetization as a function of the temperature. At 20 K was observed a peak.

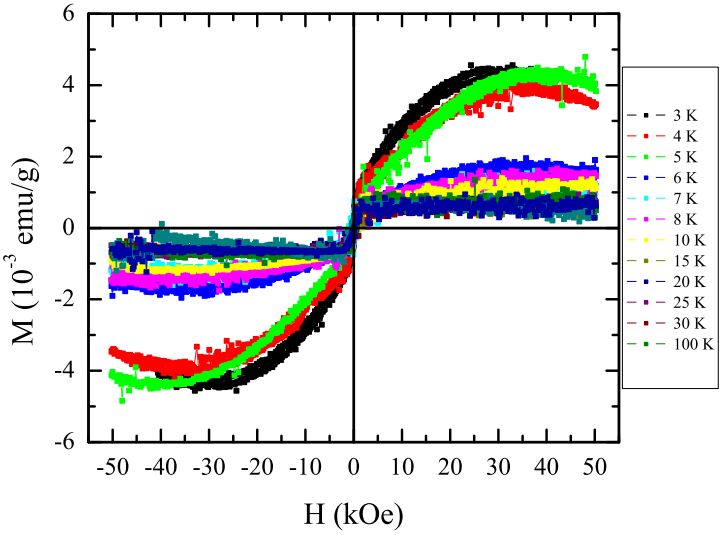

Figure 3.25: Dependence of the magnetization for sample Au TOAB on the applied field (measurements of type C). Since this sample presented a blocking temperature at 20 K, we decided make different hysteresis loop round 20 K.

The saturation field was at 2.5 kOe below the peak detected in the derivative

of the TRM magnetization data. As counterpart, for $T > 20\ K$ the saturation field is below 1 kOe, and the magnetization as a function of the applied field is independent on the temperature, such as the previous experiments.

Therefore, below 20 K the system behave ferromagnetically and above paramagnetically or superparamagnetically. To remark these features, the saturation magnetization at each temperature is represented as a function of the temperature, as is shown in figure 3.26. The saturation magnetization decreases from 3 to 20 K, whereas above 20 K the magnetic saturation remains constant.

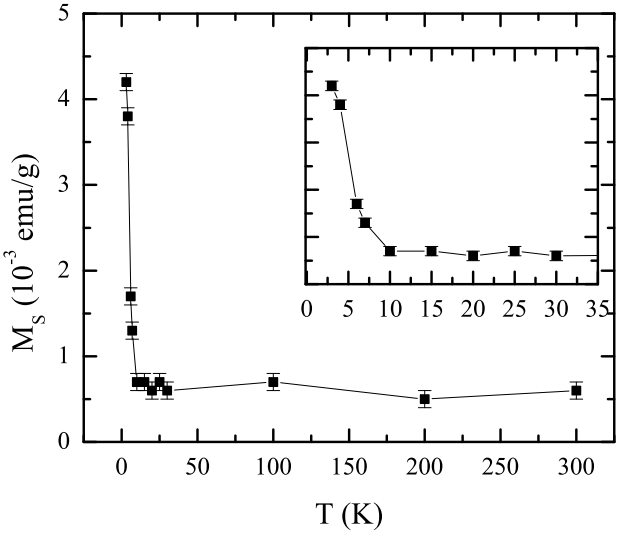

Figure 3.26: Magnetic saturation of sample Au TOAB as a function of the temperature. The data show a reduction of the saturation until 10 K in which the saturation remained constant.

3.6. Discussion

Taking into account the results for the three gold samples, we may conclude that the most plausible explanation for the observed peak in the derivative of TRM and the ZFC-FC data corresponds to a blocking temperature of ferromagnetic nanoparticles at 5 K for sample AU 1PPS and AU 3PPS, and at 20 K for sample Au TOAB. Below the blocking the particles behave as ferromagnetic nanoparticles, and above the blocking temperature the predominant contribution at low fields, in the magnetic susceptibility, was a paramagnetic signal independent on the temperature (Pauli's paramagnetism explained in the introduction section). The paramagnetic susceptibility was $10^{-6}\ emu/gOe$ for Au 1PPS and Au 3PPS

and for Au TOAB was $4 \cdot 10^{-7}$ emu/gOe. The similarity of the three paramagnetic susceptibilities confirmed that Pauli's paramagnetism was an intrinsic phenomenon associated with pure gold. In addition, the reduction of the paramagnetic signal for the complex Au TOAB is in concordance with the nature of the bond between surface gold atoms and the binding molecule, which effect is a localization of the surface electrons. Consequently, the reduction of the paramagnetic susceptibility should be related to the effect of the capping molecule on the conduction electrons.

The most plausible explanation for the different magnetic moments and the blocking temperatures of each sample is that the synthesis conditions/method, and the capped molecule affect to the magnetic behavior of the nanoparticles. First, as observed in the TEM measurements the structure and size of gold particles was different. H. Hori et al. [58] demonstrated that the ferromagnetic magnetization in gold particles capped with dodecane thiol depended on the the particle size. They showed that 3 nm diameter particles had the maximum spontaneous magnetic moment, reducing its value as the diameter decreased until 4 nm. In our case, gold particles capped with TOAB molecule was the sample containing the lowest mean diameter (round 3.5 nm). Comparing the value of the saturation magnetization with that documented by H. Hori [58] our data agree with their experimental results.

On the other hand, our results show that the capping molecule and its interaction with the surface of the nanoparticle is also important. Crespo et al [64] showed the effect of different thiols groups in the permanent magnetic moment of gold nanoparticles. They found that nanoparticles capped with polimeric molecules (non-covalent bond) showed the lowest magnetic moment, such as our results for the samples Au 1PPS and Au 3PPS. However, our sample Au TOAB, whose magnetic moment is larger than the magnetic moment of the other two samples, has a covalent Au-S bond. This type of bond promotes a permanent magnetic moment on metallic nanoparticles [68]. Another interesting result demonstrate by Crespo et al. [64] is the correlation between the SPR spectra and the magnetic moment of gold nanoparticles. The samples studied by them with larger magnetic moment were those the plasmonic resonance is completely suppress. The SPR data provided by the group of professor Ziolo showed that the plasmonic resonance was not suppressed in the samples, but sample Au TOAB had a considerable reduction of its plasmonic resonance respect to the other samples. It is clear that the nature of the bond in sample Au TOAB and its SPR spectra is in concordance with the obtained by Crespo et al.

Based on the change of the electronic structure due to the effect of the capping molecule, two different theories have been proposed in the literature to explain the magnetic behavior of gold nanoparticles. The first one is the Fermi hole effect, that is when an electron leaves a surface atom it leaves a hole in the electronic d shell in

the case of gold. This hole is generate by the charge transfer between surface gold atoms and the capping molecule. Around the generated hole, neighboring electrons (in a close sphere) promote an antiparallel orientation of their spins among the spin of the hole, hence the total spin remains zero. This scenario only occurs at the bulk of the particle. Nevertheless, when the hole is generate at the surface of the particle, the hole is only surrounded by a half sphere generating a spin imbalance. Furthermore, the sphere where the Fermi hole effect occurs has a limited range: $\frac{\pi}{k_F} = 0.3\,nm$, where k_F is the Fermi wavevector. Due to the limited size, the charge transfer that generates the Fermi hole effect at the surface generates a magnetic outer shell. In this sense is possible to interpret the particle as a core-shell system. Nevertheless, this model only explain the permanent magnetic moment at the surface, but fails in the explanation of the ferromagnetic order of the particle.

Alternatively Crespo et al. [69] suggested an unique model that explains the observed magnetism on gold films and nanoparticles. In the case of films decorate by SAMs molecules; such capping molecules form ordered domains that modifies the surface potential. This modification lies in a potential well where free surface electrons are trapped forming atomic-like orbitals, which also generates an orbital angular momentum (L_z). Crespo et al. minimized the energy related to the Hamiltonian that represents this phenomenon for a circular domain of radius ξ, where the main result was that $L_z \propto \xi^2$, and hence they predicted large angular momentums. In addition, the electrostatic energy of the trapped electrons is minimized for parallel alignment, and the spin-orbit coupling, which is large range in gold, also align the spins of such electrons, thus generating a ferromagnetic order. It turns out for small nanoparticles that SAM molecules only generate small domains and then small magnetic moments. Moreover, the reduction of the magnetic moment measured by Hori et al. [58] is also explained by this model. For large domains and size large gold nanoparticles is expected high magnetic moments (it due to the increase of the radius of the domain). Nevertheless, an increase of the size of the particle lies in a increase of the diamagnetic core that is diamagnetic, and reduces the magnetic moment of the surface. Finally, one of the basis of this model is the suppression of the SPR resonance, mentioned above, due to the localization of the electrons. In our case and based on this model, the efficiency and the domains generated by the decorating molecules is small enough to generate a low magnetic signal, as Crespo et al. demonstrated.

Therefore, and based on the theory of Crespo et al., the samples Au 1PPS and Au 3PPS that do not have covalent bonds presented the lower magnetism. On the other hand, sample Au TOAB presented the largest magnetic signal and the minimum absorption peak in the SPR spectra, as the theory predicts. As mentioned above, another proof of this feature was the reduction of Pauli's paramagnetism on Au TOAB complex. This reduction is also related to the localization of quasi-free

surface electrons in the particle, which also contribute to Pauli's paramagnetism.

It turns out that one can think that the magnetic behavior of gold particles can be due to impurities such as iron. Chemical analysis of the samples was carried out by our collaborators and they did not found any contamination in the samples. Furthermore, the effect of Fe impurities should be different, reducing the effect of the anisotropy and they do not explain the permanent magnetization [70].

Finally, despite ferromagnetic particle were clearly detected for samples 3PPS and TOAB, the three magnetic contributions founded made impossible know the behavior of the system above the ferromagnetic phase, that is if the system behaved superparamagnetically or paramagnetically.

3.7. Conclusions

Three different set of gold nanoparticles with different capping agents (two molecules with the same flexible part, and TOAB molecule) were magnetically characterized using a SQUID magnetometer. Moreover, their structural characterization showed that the particles had a mean size of 6 and 10 nm for samples Au-1PPS and 3PPS, and 3.5 nm for the TOAB agent particles, respectively. This particle size was ideal for magnetic phenomena for gold nanoparticles capped with organic molecules [58].

Because bulk gold is diamagnetic, and we expected a small positive signal for the samples, the samples holders were characterized before the samples. The results showed a diamagnetic signal prominent from the sample holders. Therefore, the data analysis consisted on subtract the diamagnetic signal from the sample holder to the samples. Although this operation, the resultant signal was also diamagnetic. Consequently, the samples presented a large diamagnetic signal. Another correction was needed to remove the intrinsic diamagnetism of gold, obtaining a positive signal.

ZFC-FC magnetization curves showed for sample Au 1PPS and Au TOAB an increase of the magnetization until 100 K and 50 K respectively, which those values corresponded to the inflection point in the curves. Above these temperatures the magnetization remained constant. This behavior was firstly associated with a barrier energy distribution. For the case of Au 3PPS the ZFC-FC magnetization data suggested a paramagnetic curve, with a remanence between the two branches.

On the other hand, Thermal Remanent Magnetization measurements were fully compatible with the information extracted for the ZFC-FC curves: an inflection point was detected for the three samples at positions similar to the inflection point of the ZFC-FC curves. The derivative of TRM data showed a peak, such as the ZFC-FC measurements, also suggesting a energy barrier distribution.

Isothermal magnetization curves showed two interesting phenomena: a pre-

dominant paramagnetic signal at low fields and a ferromagnetic behavior below the peaks founded in the ZFC-FC curves. The paramagnetic signal independent on the temperature was interpreted as Pauli paramagnetism that is a intrinsic magnetic susceptibility for metals. Nevertheless, the ferromagnetic signal was different depending on the capping molecule. Consequently, the bond between the molecule and the particle was crucial to generate the magnetic behavior of the particle. Since the molecular capping was in the surface, we conclude that the magnetic effects were at this region of the nanoparticles. The interaction between the capping molecule and the gold atoms, Au-S bonds concretely, generated a ferromagnetic order on the surface of the nanoparticles. As counterpart, the core of the particle remained diamagnetic, it being the principal source of diamagnetism in the samples. Some works [71] have suggested and have proved a theoretical model for a ferromagnetic shell and a diamagnetic core that interactuates between them by an exchange interaction, supporting our hypothesis. Although this theoretical works explain the general behavior of magnetic gold nanoparticles, they do not take into account the source of the ferromagnetic order at the surface.

As discussed above, the kind of bond between surface atoms and the capping molecule should generate a ferromagnetic order in the surface of the particles. Sample Au TOAB had a reduction of its plasmonic resonance that is associated with the nature of the binding molecule, and therefore a change on its electronic structure and the ferromagnetic order on the surface of the particle, as mentioned in the previous section. Nevertheless, this theory cannot explain the ferromagnetic behavior observed in samples Au 1PPS and 3PPS, but it turns out that such binding molecules generate a low magnetic moment, for which the reduction can be associated with the bond or the fact that those particles presented a largest size (the diamagnetic core counterbalance the ferromagnetic shell). Moreover, Crespo et al. [69] demonstrated that magnetic order in the surface is promoted by the level of self-assembly of the molecular chain capped to the nanoparticle, and, hence the magnetic properties are tuned by the capping molecule, such as our results. Based on our results, the more effective mechanism for the formation of a ferromagnetic shell was for the gold-TOAB complex.

Finally, magnetic gold nanoparticles may represent a wide range of applications, such as in optics, medicine, nanotechnology or solar cells technology. The efficiency of charge transfer between the particle and the capping molecule is a crucial parameter to improve the efficiency of the solar cell. Furthermore, gold is a biocompatible material that combined with organic capping and these new magnetic properties can have a great variety of applications in drug delivery, magnetic hypertermia, or NMI because of their low toxicity. In the context of our work, metallic gold nanoparticles having a magnetic behaviour are an interesting sistem to be combined with high frequency technology. First, gold is a biocompat-

ible material that can be used for magnetic hyperthermia, drug delivery, or NMI. At last, magnetic gold nanoparticles can open new technological applications and phenomena such as explained in chapter 2, combining their electrical and these new magnetic properties.

Chapter 4

Non-invasive Terahertz time-domain and its application in the measurement of the permeation of topical drugs

In the twentieth century, electromagnetic waves have been of great interest in inspection of materials [72], biological tissues [73], and detection of chemicals [74]. For example, X-ray is used in medicine for the inspection of whole human body [75], [76] and in security inspection luggage in airports. But X-ray is an ionizing radiation and different secure protocols are needed. Less energetic radiations, such as microwaves, are safer than X-rays but they present worst resolution.

Technologies based on electromagnetic radiations, such as spectroscopies techniques [77], are also extended methods to identify in a rapid and effective way compounds as hazardous, chemicals or explosives. But depending on the electromagnetic band, photochemical reactions can be induced, and consequently, a correct selection of frequency band is crucial to ensure that neither chemical nor structural changes occurs in the system under study.

The progress in femto-laser technology combined with semiconductor materials have made possible the generation of coherent T-rays [78], [79], which has been a forbidden band until the nineties. Terahertz band, which has a submillimeter wavelength and low energy (several meV), has represented a new wide range of applications in material science [79], [80], biology [81], spectroscopy techniques [82], [83], chemistry [84], [85]and physics [86], [87]. For example, Terahertz is a potential technology that can be applied in pharmaceuticals problems as the percutaneous flux onto skin of topic drugs, but also surface material inspection with great importance in quality construction tests. This new technology promotes a non-invasive, non-destructive and cleaned methodology, whereas traditional technologies based

on electromagnetic waves do not accomplish these characteristics.

In this chapter Terahertz technological applications will be reviewed as material inspection technique and, specially, its application in the permeation of liquid pharmaceutical excipients through synthetic membranes and human skin. The chapter is structured as follows: First the problem of the permeation of drugs and its experimental studies is exposed. THz radiation is introduced as a new technique, some of its applications in material inspection, and the codification of information using low THz frequencies as well. Finally in vitro experiments in artificial membranes and human skin are shown, and revealing the possibility of characterize the permeation of any substance with Terahertz time-domain technology.

4.1. Introduction

Typical drugs are composed by an active molecule that carries the therapeutic effect of the formulation, and excipients (or vehicles) pharmacological native substances that allow the dispersion of the active in the treatment zone. In particular, topical formulations distinguish from others, because they are applied onto skin or mucous membranes [88], thus the effect is founded locally. For this reason, it is possible directly study their delivery process into the application zone.

Release mechanism of topically applied formulations onto the application zone is known as the permeation process [89]. Drug permeation through skin is influenced by the penetration kinetics of active components present in the formulation (permeation enhancers) or excipients [90], and then obtaining a specific drug's permeability profile as a function of the formulation. These features allow to improve the permeation of the topic formulation, for example including in the formulation chemical penetration enhancers, novel vehicle systems, e.g. microemulsions, liposomal-based delivery systems, and supersaturated formulations, such as iotophoresis, sonophoresis, and electroporation [89].

Importance of correct characterization of drug release process lies to determine the necessary amount of active in the topic formulation and the dosage interval. The main drawbacks in-vivo research of permeation of topic formulations are unpredictability, inter individual variability, or tissue availability limitations. For these reasons, on the other hand, in-vitro evaluation of release rate of active substances formulated in topical delivery systems requires the use of non-biological permeable filter media [91], which mimics skin barrier function [92], but they do not present the inconveniences explained above. Membranes range in barrier function from negligible resistivity to a permeability similar to human skin (high resistivity). Tests to study the permeation process in artificial membranes are based on applying the formulation on the top of the membrane, and afterwards

the substance that cross the membrane is collected at different times. Then the concentration of the arriving drug is characterized as a function of time.

4.1.1. Skin structure and its barrier function

The skin is composed by two fundamental parts: the outer epidermis and the inner dermis [89]. The dermis contains capillaries, sebaceous and sweat glands, hair foricles and nerves. On the other hand, the epidermis has a multilamellar structure formed by cells in different phases of differentiation, which means different metabolic activity. As important remark, the outer cells of the epidermis, corneocytes, are surrounded by a multilamellar lipid bilayers and constitude the last layer (round 10-20 μm) of the dermis, named the stratum corneum (see figure 4.1).

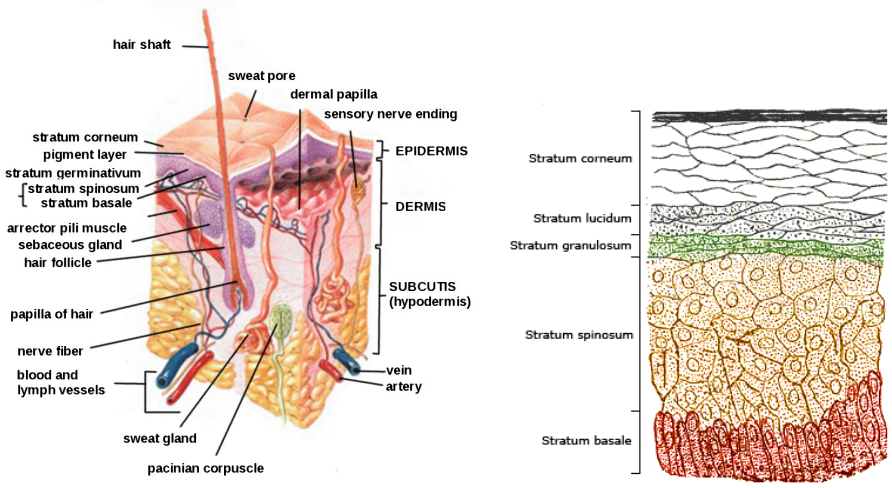

Figure 4.1: Layer structure of the skin. Two important layers forms the skin: epidermis and dermis. The stratum corneum (the outer layer in skin) is the main barrier function of skin, and its structure limits the pass of any substance.

The function of principal barrier in the mammalian skin is realized by the stratum corneum [93], whose properties are based on the specific content and composition of the lipids forming the layer, in particular, due to its arrangement structure matrix for intercellular lipids and the lipid's envelope surrounding the cells.

Regarding to skin permeation, there are two different pathways for the permeation of substances through skin [94], [89]: the diffusion through the intact epidermis and through the skin appendages; for example hair follicles and sweat glands. Nevertheless, the skin appendages represent the 0.1% of the human skin surface, and the contribution of these pathways is usually considered to be small.

In the case of the diffusion through the intact epidermis, the most important pathway is the intracellular lipid route between the corneocytes and the intervening lipids, (see figure 4.2). In any case the permeant have to diffuse through the intercellular lipid matrix, that determine the percutaneous transport rate.

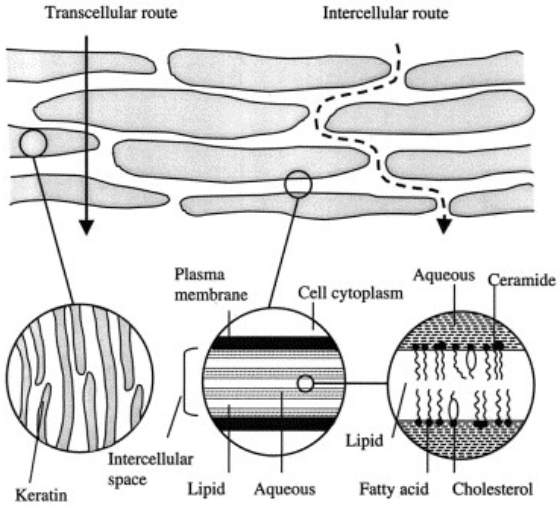

Figure 4.2: Different percutaneous routes: transcellular and intercellular pathways. Transcellular rout implies a direct pathway across the stratum corneum, while intercellular route happens in the plasma membrane.

4.1.2. Quantification of the permeation into artificial membranes and skin

Diffusion cell method [95], as depicted in figure 4.3, is one of the most extended technique to quantify the permeation of a topical formulation in-vitro skin or porous medias. It consist in a donor and a receptor compartment separate by membrane or skin sample. In the donor compartment is dropped the formulation under study, whereas the receptor collects the substance that cross the membrane. Measuring the amount of drug that permeates in the receptor chamber allows to determine the concentration profile as a function of time. For formulations composed by different actives and excipients, the diffusion cell method is typically combined with chemical analysis methods for the correct identification of each permeated substance, where the most used analysis method is the High-performance Liquid Chromatography (HPLC). In addition, this method is mostly used for study the effect of chemical enhancers in the formulation for increasing its permeation rate.

Otherwise, if one wants to characterize the diffusion in a contactless way, the main used technique is ATR-FTIR spectroscopy technique [96], [97]. This method

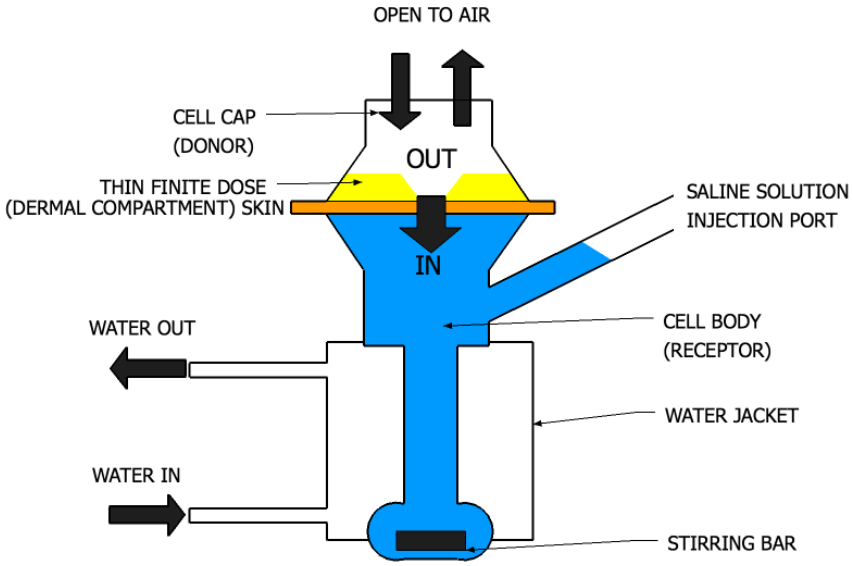

Figure 4.3: Scheme of a diffusion cell. In this experimental set-up the sample is sandwiched between topic formulation and the cell. The formulation is applied at the top of the sample, where its bottom is in contact with a saline solution, to remove any substance that diffuses in the whole sample and ensure homogeneity in the receptor compartment.

is based on the characterization of resonant absorption peaks in the infrared band. Because the stratum corneum is the main barrier that limits the rate of the percutaneous absorption and it lies directly between the donor and the skin layers, one can reasonably expect that the concentration of the drug in the stratum corneum should be related to the concentration of deeper layers. For this reason in ATR-FTIR, the skin sample is placed between a reflectance plate and a donor solution, where the diffusion of the permeant in the deeper layers is observed by the appearance and increase of characteristic absorption's peaks in the infrared band. The main drawback of ATR-FTIR spectroscpy is that only molecules with resonances in the infrared band can be characterized with this technique.

Finally Skin Stripping [97], [98] is one of most extended technique in the last decades and is used to measure the drug concentration and its profile through the stratum corneum in vitro and in vivo experiments . The donor is applied on the forearm of a patient and those layers that compose the stratum corneum are progressively removed by serial adhesive tapestripping. The determination of the drug amount and the size of the stratum corneum removed by each tape-strip allows to compute the diffusivity and the solubility of the topic formulation. For multicomponent formulations, this technique is combined with an analytical

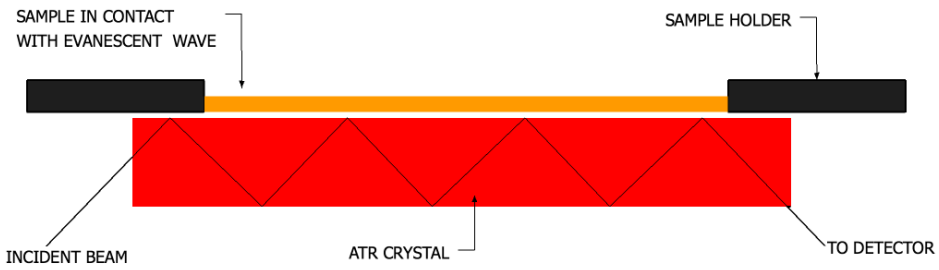

Figure 4.4: ATR-FTIR scheme. In this technique the sample is placed between an ATR crystal, on which infrared waves can cross it and a evanescent plate, where the waves are reflected. The detector collects the outer signal from the sample and the permeated substance in the inner layers describing the evolution of the detected absorbtion resonances and identify the substances besides.

method, such as HPLC in order to identify the compounds in the formulation and its release rate.

In-vivo and in-vitro characterization techniques of topic drugs permeation present two principal problems, the biological variability and the level of invasiveness of the technique. The differences in each individual tissues can just be solved with a large number of individuals in each clinical trial, whereas the level of invasiveness of a technique can be treated in different way, such as a non-contact technique. On the other hand, technical problems such as the price or the viability are present in the exposed techniques, which currently are the most used. For instance, the main drawback of the diffusion cell method is chemical analysis techniques are necessary for multicomponent formulations , like HLC and then increasing the cost. Despite ATR-FTIR allows a non- contact, direct identification and chemical analysis for each component, its applicability is restricted for substances with characteristic resonances in infrared band. In addition, this two techniques can only be applied in-vitro experiments. Finally tape stripping represents an easy and inexpensive technique that permits to characterize the concentration profile in different layers of the stratum corneum as a function of time, but, with high level of invasiveness.

In summary, the requirements for a good experimental approach in the permeation problem of topic formulation through skin are the unification between the

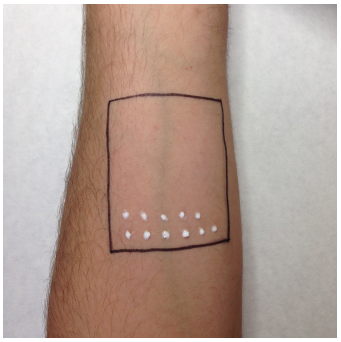

(a) The topic formulation is applied using a controlled volume.

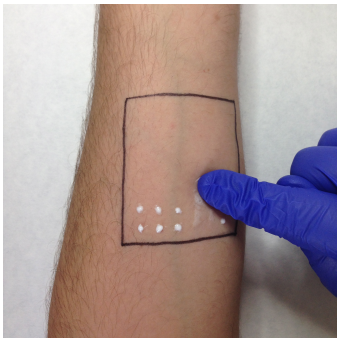

(b) Application of the topic formulation.

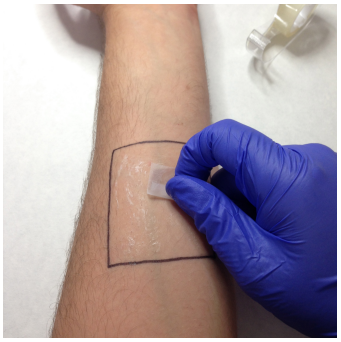

(c) Tape stripping for a sample.

Figure 4.5: Tape stripping method.

data acquisition and its analysis, in a way in which the system under study is not modified.

For these reasons, our proposal to study the diffusion problem into skin, is the use of non-invasive, non-ionizing and non-destructive electromagnetic radiation such as terahertz, based on a general methodology and non necessary that the formulation present absorption resonances in some electromagnetic band as in the case of the ATR-FTIR spectroscopy.

4.1.3. Terahertz radiation

The terahertz (T-rays or THz) band is the electromagnetic radiation spanning the 0.1 to 10 THz frequency (see figure 4.6) , between the millimeter and the infrared spectra. For example, 1 THz corresponds to a wavector of 33.3 cm^{-1}, an energy of 41.4 meV and a wavelength of 300 μm. For instance, THz frequencies are associated with intermolecular vibration and molecular rotations associated with the flexion of individual molecules or intermolecular interactions by strong hydrogen bonds or weaker Van der Waals forces[78], [99]. From a technological point of view, this band includes applications from electronics to photonics [100], [101], [102], [78].

THz band has been a forbidden part of the electromagnetic spectrum until the ninetieth decade, named the THz gap, and consequently without any relevant technical application. In the past, since THz lies between microwaves and infrared bands, several approaches have been tried to achieve coherent T-rays using well established techniques such as optical and high microwave frequencies generation techniques [103], but they presented poor results.

The different approaches to achieve coherent terahertz waves using electromag-

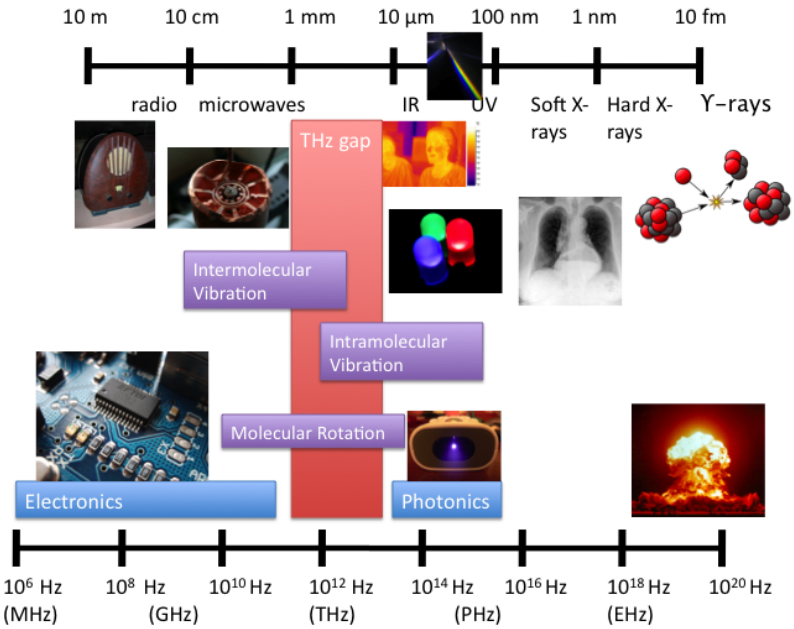

Figure 4.6: Position of the THz band in the electromagnetic spectra, which lies between the microwaves and the optic spectra.

netic sources based on optics, such as semiconductor laser diodes, extend down only to the order of tens THz [104]. In addition, the thermal energy at room temperature and the inhomogeneous broadening of the transition states makes the optical band structure a bad strategy to achieve T-rays. In contrast, in the region of low frequencies the power of the sources based on electronic devices, such as the used in mobile phones (transistors technology), generates a frequency beyond few hundreds of GHz but the circuits become unresponsive [105]. Although it is possible to use frequency multipliers, it has been demonstrate their low efficiency. Hence, THz band is an intermediate region where neither optical nor electrical mechanism can be used to its generation.

In the middle of the nineties THz band started to be able thanks to the introduction of stable, turn-key ultrafast lasers and improvements in the generation and detection of coherent THz radiation [78], [106]. THz radiation can be generated by the excitation of some material or patterned structure with a femto-laser pulse (laser that is capable to generate coherent pulses in approximately $\sim$ 100 fs), with a bandwidth that lies from 0.3 to 5 THz and an average output power that belongs from nW to few μW. It has been demonstrated that air plasma can be used as emitter and detector of THz radiation [107], [102], presenting a bandwidth larger than the one based on femto-laser methods.

In our experiments we used the femto-laser method because it is the most extended technology for generating and detecting THz frequencies [106]. In such methods, the excited material is typically a photoconductive antenna (PCAs) or an electro-optical crystal (EO), where the mechanism of THz generation are the transient generation of photo-carriers in the photoantena; or and second order nonlinear processes in electro-optical (EO) crystals. Since our experimental equipment for T-rays generation is based on PCAs this text only focuses the generation of THz waves by photoconductive emitters.

A photoconductive emitter consists of a small semiconductor crystal piece, normally Gallium Arsenide (GaAs), where two metallic electrodes , whose geometric design is that of an antenna, support a large electric field across its surface, and the ultrafast laser is focused onto the gap between the electrodes. Because the energy of the photons is higher than the band gap of GaAs semiconductor, consequently the emitted photon generates a fotogenerated electron-hole pair excited near to the surface of the crystal, which rapidly change the conductance of the GaAs (effectively closing the optical switch). The application of a bias voltage accelerates the electron-hole pairs and allows a fast change in the density current. The changing dipole produce a THz transient in the antenna that is emitted to free space. In addition, the polarization of the wave is parallel to the bias field, perpendicular to the gap between the electrodes. Thus the generation of the THz radiation is owing to the time variation of the density current, $J(t)$, generated in the surface of the crystal by the femto-laser, and the amplitude of the generated electric field can be expressed as [106]:

$$E_{THz} = \frac{Ae}{4\pi\epsilon_o c^2 z}\frac{\partial N(t)}{\partial t}\mu E_b \tag{4.1}$$

being A the iluminated surface by the laser, e the electron charge, ϵ_o the permitivity of free space, c the speed of light, z the depth of the laser inside the crystal, $N(t)$ the density of photo carriers, μ the mobility of the carriers, and E_b the bias field. In figure 4.7 is represented the generation of a THz wave with a fotoconductive antenna.

Usually the main aspects taking into account in the fabrication of a photoconductive antenna are:

- The semiconductor band gap must be smaller than the energy of the photons emitted by the laser, if not the photocarriers will not be generated, neither the THz wave.

- Semiconductor with carriers with short lifetime are preferable because they generate short THz pulses, thus they achieve broader THz spectra.

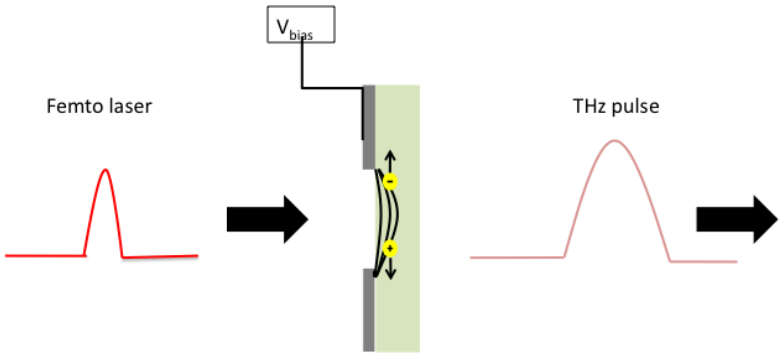

Figure 4.7: Photoconductive antenna method to generated THz radiation. The PCA is exited by a femtolaser, that generates a electron-hole pair. The applied bias filed generates oscillations in the density current promoting the emission of THz radiation to free space.

- Carriers with large mobility increase the efficiency for the THz emission, because they accelerate faster with less bias.

- Antenna gap: Narrow gap PCAs require minor bias but they are easier to damage, and also require an excellent alignment of the laser, to illuminate the entire gap efficiently. Therefore is preferred the use of broad PCAs, because typically they are capable to generate more intensive THz pulses.

- Bias field: The outer power of the THz signal increases with the bias field, but there is a maxim field before the material breaks down. This value depends on the gap size and the density of carriers.

As final remark, the correct illumination of the whole gap with the laser is important for the generation of THz radiation by PCAs. If entire gap is not illuminated with the laser, the active surface of generation of photo carriers is smaller. On the other hand if part of the laser illuminates an outside part of the semiconductor, a fraction of the laser's energy is lost. The better solution for control the spot size of the laser is mounting a focusing lens in an stage translation, in order to align the laser with the gap.

In addition, a number of detection techniques can be employed from bolometric measurements [108] and electro-optical sampling [109] to photoconductive emitters [110]. Using a PCA as detector is the most common method and involves measuring the photo current generated by the laser probe beam in the electrodes. If any electric field is applied across the gap, the photo-carriers generated by the prove beam diffuse randomly and do not generate any current. However, when a THz wave illuminates the gap, the associated electric field separated the electro-hole pairs and a net current is generated. This current is proportional to the amplitude of the electric field of the THz wave, $J(t) \propto E_{THz} N(t)$.

Commercial generator and analyzer of terahertz radiation from Zomega Terahertz corporation, Mini Z, has been used for our research as source radiation generator and analyzer. The equipment generates pulses of T-rays with a peak frequency at 1 THz and a bandwidth of 3 THz, and using a photoconductive antenna for their generation and a EO for detection. The equipment can perform reflexion or transmission measurements and in both cases it is detected the electric field in time domain range. Besides, for measurements in the frequency domain, the system computes the Fourier Transform of the time domain signal. Measuring a reference signal (usually without sample) and performing other measurement with the sample under study, the absorption spectra can be computed by direct division of both.

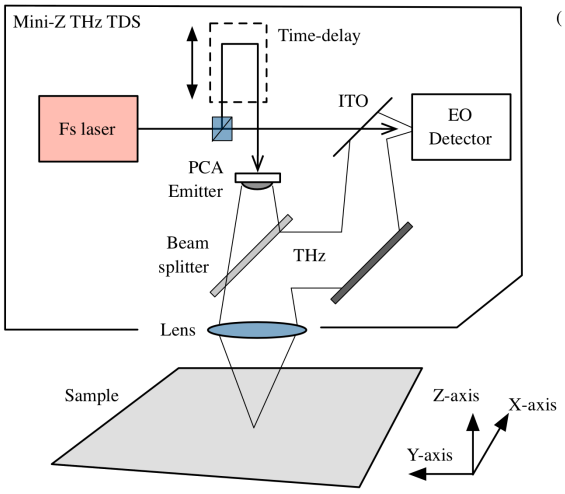

Figure 4.8: Scheme of Mini Z, working in reflection mode. A femtolaser exited the PCA generating the THz wave. The signal interacts with the sample and is collected by the equipment for its analysis in time domain.

4.2. Terahertz applications

Because THz frequencies are non-destructive ,in the last years a wide range of technological applications have been developed: detection of biohazards and explosives [111], art inspection [112], medical and pharmaceutical applications [113], and at low frequencies (ranging from 0.2 and 0.3 THz) the codification of relevant information in brands, which have been developed by our group work.

The most important applications in material inspection are those related in security [114]. [111], art inspection [115], [112] and material integrity inspection [79]. For example, in some airports, such as USA and Australians airports, have begun to use Terahertz scanners as new security method. The key concept in this new technology is the possibility to generate a safe and complete image of a person showing the content behind its clothes, since clothing is transparent in the THz range. Consequently, mapping the reflectivity at each point of the body of the inspected object a whole image can be performed. As clothings have low, and metals high reflectivity (knifes or guns), then hidden objects can be detected without having to register or exposing to dangerous radiations any passengers. Imaging techniques based on the different properties of T-rays can be applied successfully in art inspection, to verify the authority of the picture or to find different previous sketches behind the visible picture [112], or also to characterize the pigments.

4.2.1. Low THz frequencies application: Terahertz contactless tagging

Despite coherent T-rays are normally generated by PCAs or Eos, it is also possible to use microwave technology, e.g. frequency multipliers. These systems transform low frequencies, from 8 to 16 GHz, in a high frequency signal, between 0.1 and 0.3 THz, but the output power depends on frequency. In addition, the output signal is not achieved by a pulse that includes the spanning of a central frequency, rather each signal is generated in a frequency sweep ramp, for which the receptor's response is measured individually. Consequently, these systems are slower than conventional THz equipments, and have a resolution depending on the frequency. On the other hand, the main advantages that represent high microwave devices are their simplicity and the large penetration in materials for these frequencies, round 1 mm for 0.3 THz. In this work we have improved both the reception and reading of THz contactless tagging.nd lecture of THz contactless tagging. The main goal was to codify relevant information using THz waves ranging between 0.1 and 0.3 THz.

Barecodes represents one of the most useful and extended method to encapsulate and codify relevant information in order to recognize an item in unambiguous

way on any point of a logistics network. Typically they consist in a code of vertical and parallel black lines of different thickness and different separation between them, where each ensemble of bares and spacing represent an alphanumeric character. In traditional systems, the detection and interrogation of the code is achieved by red light, where a detector measure the reflectivity of the whole barcode along a line, it being maximum for a spacing and minimum for each bare. Therefore, the lecture of the information (interrogation of the code) is performed by the generation of a specific temporal or frequency footprint. These optical systems offer the advantage that are printable in substrates like paper or plastics, but they require and unobstructed path for a correct lecture and a manual reading stem from the response dependence of the incident radiation on the code [116]. On the other hand, systems using radiofrequencies (RFID systems) [116], [117] represent an advantageous alternative due to the reduction of the cost of the materials as well as the transmitter can be placed inside pockets or attached to vehicles, improving the security of the tag. Nowadays, there exist two microwave based barcodes [118]: active tags that need a power supply, and passive tags, which work without any battery. However, passive tags are the most used because their reduced cost, although they can only work for short range applications. For these reasons, THz technology can provide a miniaturization of the labels. In basis on currently optical and RFID technology, we have realized two approaches: imaging and spectroscopy, both based on transmission measurements as a proof of concept of THz tags. In the imaging approach the principle lecture was based on the different microwave transmission between the bares and the substrate of the tag. In the case of spectroscopy lecture principle the information was encapsulated by characteristic frequency resonances of the tag.

For both type of experiments, it was used the same kind of samples which were prepared using typical integrate circuits technology. The barcodes design was the same as the usual in optical devices. The tags were made using an integrated circuit board purchased on Repro Circuit ltd., and they are composed of a substrate of fiber glass covered with a thin layer of copper (35 μm). Besides, the copper layer is covered by a uv-photosensible resin, whose function is transfer any pattern printed on a transparency to the whole plate. A wide range of barcodes lengths and spacings between them were designed by computer, and printed in the transparencies, whose patterns were transfer to the plate by uv radiation, and a chemical treatment. In each barcode, copper lines constitutes the bare code, and the fiberglass between each line the spacing, such as optical barcodes. As interesting remark, the substrate did not have any ground plate, as contrary to currently chipless designs. The effective surface for plates for the optical lecture was 2x4.6 cm^2. On the other hand, the plates prepared for the spectroscopy method lecture, were made of 256 lines on a 8x7 cm^2 effective surface. This was done in order to

ensure sufficient absorption by the sample (the lecture principle was based on the detection of resonant frequencies as explained below). Finally the nominal size of such lines were between 0.57 and 2 mm, then opening the possibility to tune the resonant frequency.

Image and spectroscopy interrogation of THz tags were carried out using bistatic detection, such as in the experiments described on chapter 2. Both approaches used a microwave source (8360B Synthesized Sweeper from HP) providing microwaves with a frequency between 10 MHz and 20 GHz. The microwave source was connected to a frequency multiplier stage that upconvert the low frequency signal (ranging between 8 and 16 GHz in the experiments) up to 0.3 THz (represented in figure 4.9). The THz beam was emitted and detected by two horn antennas, where the receptor was attached to an multimeter for detecting the RMS voltage, and then, measure the bistatic coefficient S_{12}.

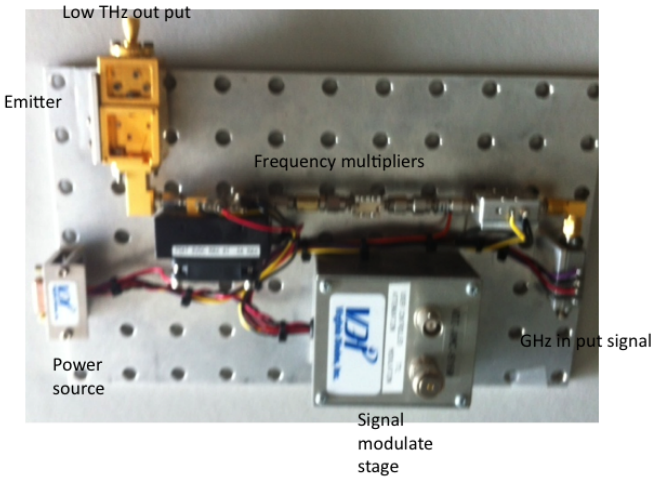

Figure 4.9: Multiplier stage. GHz signal passes in a sequence of frequency multipliers, of which the frequency is amplified 24 times. Emitter antenna is at the end of the amplifiers. Moreover the set-up posses a modulator stage for external signals.

In the image formation experimental set-up (see figure 4.10), the sample was placed between both antennas, emitter and receptor, at the top of a polyethylene plate, which is transparent in the used frequency range. Four parabolic mirrors focused the signal generated by the emitter antenna, and recollected the beam that cross the sample in the receptor antenna. For measuring the transmittance at each point of the sample (pixel formation), the sample holder was mounted onto two pass motors, in which both allow that the sample holder had a plenty movement in the x-y plane (1 mm of resolution). Therefore, the whole sample can be divided

in points (pixels), and an image was generated by the transmittance measurement. Finally, like optical and other microwave barcodes systems, our system works at fixed frequency: 0.27 THz. The data analysis was carried out normalizing the measured RSM voltage at each pixel by the transmission highest value measured on the whole sample. The result was an image, where the colorbar is: white for he highest transmission value, and black for the lowest value.

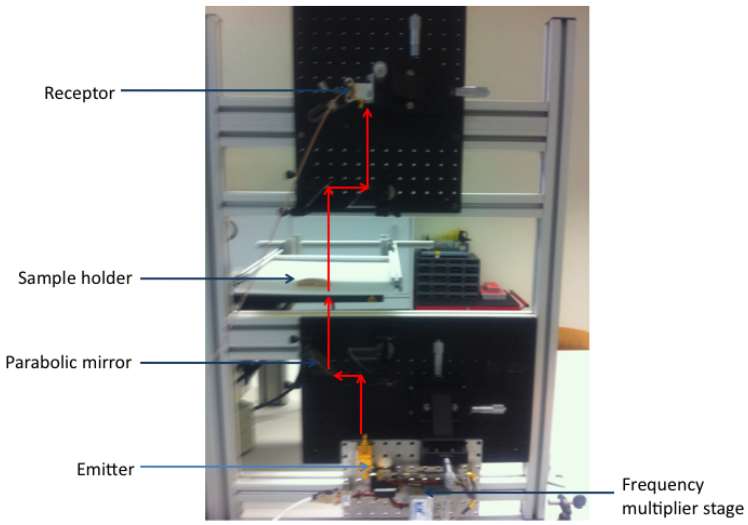

Figure 4.10: Image generation experimental set-up. The four parabolic mirrors focused the beam on each point of the barcode, and recollect the transmitted radiation to the receptor antenna.

Lecture principle in such system is the same as optical systems. Copper bares present low transmission at microwave radiation, and the fibber glass is quasi-transparent at microwave frequencies. Therefore, it is possible to construct a code such as in the case of optical systems. Optical image for one of the constructed barcode, its microwave image, and the principle of lecture for the image formation are represented in figure 4.11(a), 4.11(b), and 4.11(c), respectively.

As seen in figures 4.11(b) and 4.11(c), totally image using low terahertz frequencies was possible as well as the construction of bit codes. The transmittance measurement allows two bits, 0 for low and 1 for large transmittance. For real devices would be preferably use reflexion measurements. But taking into account $1 = R + T$, where R is the reflection and T the transmission coefficient, the transmission measurements are a proof of concept of the use of such technologies on tagging, because transmittance image will be the negative image of a reflection image. Finally, laterally scanning is the only requirement for such tags, then reduction of the axial dimension can be achieved for real applications decreasing

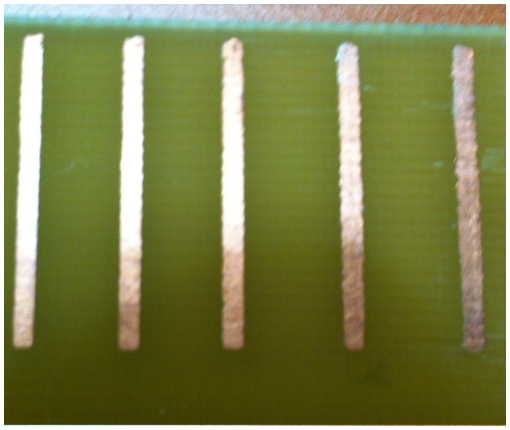

(a) Optical image obtained for barcodes with 1 mm width and 6 mm separation.

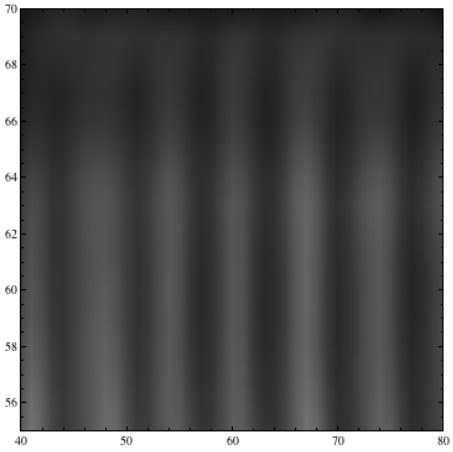

(b) Microwave image obtained for previous barcodes. The values of the transmittance are represented as a color-graph in the picture. Black corresponds to low transmitance and white corresponds to large transmittance as well.

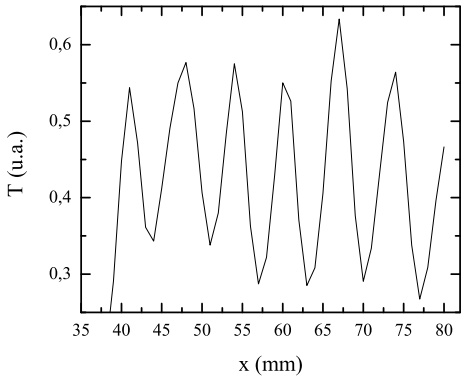

(c) Scan line of the bars. A final device will obtain this signal, where direct assignation of bits, 0 and 1, can be done.

Figure 4.11: Sample and results for optical principle lecture.

dramatically the surface of the whole tag. As interesting remark, the THz barcode can be behind any clothing or plastics, it complicating the subtraction or localization of the code, despite this operation principle mimics the basis of optical bare codes.

As counterpart, the spectroscopy detection system was based on the detection of characteristic resonances in the sample, and then do not need the pass motors, neither focus the beam on the sample. For these reasons, it is enpugh the use of a parabolic mirror to recollected the beam coming from the emitter antenna ensuring whole illumination onto the sample. A second parabolic mirror focused the emerged beam from the sample to the receptor, and the RMS voltage of the receptor was measured by the multimeter. The measurement protocol in this case consists in measuring a reference spectrum and, afterwards, the spectrum of the sample. Therefore the absorption spectrum of the sample becomes:

$$Abs = \frac{Transmittance\,(sample)}{Transmittance\,(reference)} \tag{4.2}$$

In this case the design of the bares were the type of dipole-like antennas, where each bare in the code should actuate as a resonator, whose characteristic resonant frequencies are:

$$f_R = \frac{n}{2L\sqrt{\epsilon\mu}} \tag{4.3}$$

where n is the order of the resonance, L is the length of the dipole antenna, and ϵ and μ are the permitivity and the permeability of the medium surrounding the antenna. If the antenna is in free-space, $1/\sqrt{\epsilon\mu} = 3 \cdot 10^8\ m/s$, then in basis on equation 4.3 an antenna with resonant frequency at 0.3 GHz should have a length around 0.5 mm. Consequently, thin bares, with appropriate length and sufficiently separate between them to prevent interactions, can be treated as dipole antennas where the information should be encrypted by their resonant frequencies. For this purpose, plates containing dipole-like antennas with different nominal length were placed in the spectroscopy set-up explained above, in all the cases ensuring whole illumination in the sample. To estimate the absorption spectrum in all measurements, it was used equation 4.2, where previously was set a reference with an empty fiber glass substrate. Figure 4.12(a), 4.12(b), and 4.12(c), depict a photograph of a sample containing 256 antennas with 0.57 mm of length, and the collected spectra for horizontal and vertical orientation for the samples in order to study the effect of polarization of the electromagnetic wave.

The results show that THz waves were polarized horizontally in agreement with the fact that in vertical orientation the electromagnetic field does not stimulate the antennas. The detected resonances are 236.7, 267.39, and 296.19 GHz. Fitting the measured resonances with equation 4.3 was found that they correspond to the

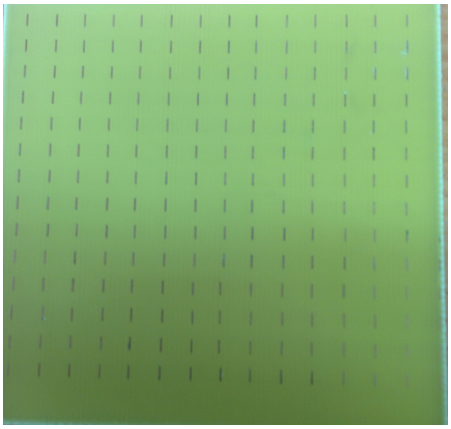

(a) Photograph for sample containing 256 antennas with a length of 0.57 mm

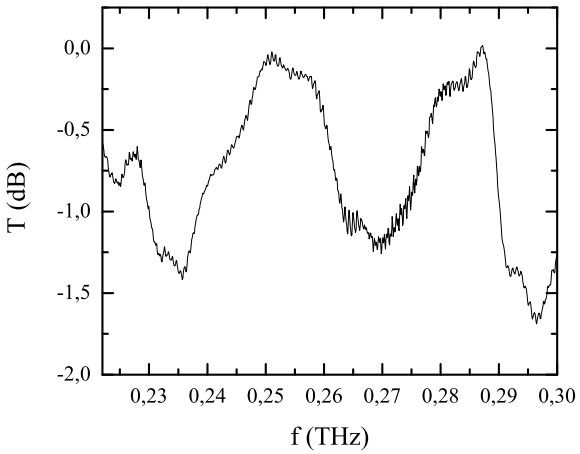

(b) Recorded spectra with the bares oriented horizontally.

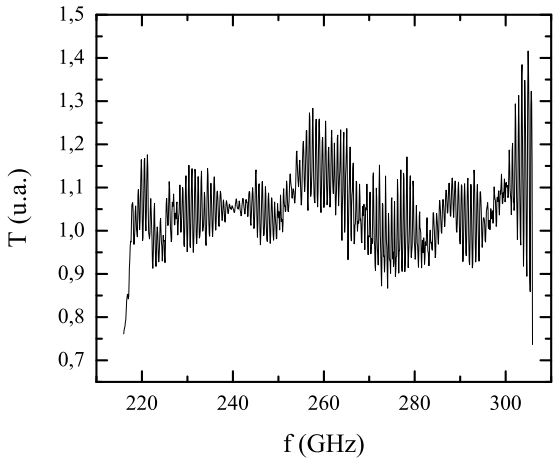

(c) Recorded spectra with the bares oriented vertically.

Figure 4.12: Sample and results for spectroscopy principle lecture.

$8th$, $9th$ and $10th$ order. For antennas for this size it was expected lower orders than the obtained in our experiments. The most plausible explanation for this experimental fact is that $\sqrt{\epsilon\mu}$ stem from the dipole antennas which are enveloped by fibber glass. Consequently the electrical and magnetic properties of the medium were different than in open air, with a lower velocity value (factor $\sqrt{\epsilon\mu}$). However, it is remarkable the possibility of measuring large orders of resonances, which allows correct encoding of the information. In table 4.2.1 are summarize the observed frequencies for the assessed dipole-like antennas.

Nominal length (mm)	**Resonant frequency** (THz)
0.57	0.237
	0.267
	0.296
1	0.229
	0.255
2	0.248
	0.270
	0.295
2.5	0.229
	0.245

Table 4.1: Resonance frequencies for barcodes with nominal length between 0.57 and 2.5 mm.

This method can be combined with image technique, consequently it will be obtained spatial and resonant encode. In addition, resonance measurements should allow a layer structure with different antennas size, increasing the resonant frequencies and improving the security of the system.

4.2.2. Studies of the layers thickness

Our group has also developed new interesting techniques in different fields as material inspection or detection of drugs by their characteristics resonances, it using femto-laser technology to achieve THz radiation. Such techniques were based on the characterization of crucial parameters of THz waves when they interact with matter. Measuring, for example, the flight time of the wave between the emitter/receptor and the sample, one can compute the distance belonging to the THz source and the sample. This simple operation is performed measuring the optical delay at the reflected signal is detected. Therefore, if the wave propagates in open air (refractive index, n, equals one) this distance, d, becomes:

$$d = \frac{ct}{2} \tag{4.4}$$

where c is the light's velocity, and t is the optical delay for which the reflected signal is detected. Layered structures, where each layer has a different refraction index , present multiple reflection peaks in the time domain spectra. Using equation 4.4 the width of each layer can be computed by:

$$d = \frac{c\Delta t}{2n} \tag{4.5}$$

where d is the width of the layer, Δt is the difference between optical delays of contiguous layers, and n the refractive index of the upper layer. As depicted in figure 4.13, for each interface, e.g., air-layer 1, layer 1-layer 2, layer 2-layer 3, and so on; a reflection peak is detected in the time domain analysis. Knowing the index of refraction of each layer, with an unique reflection measurement the structure of any layered material can be characterize.

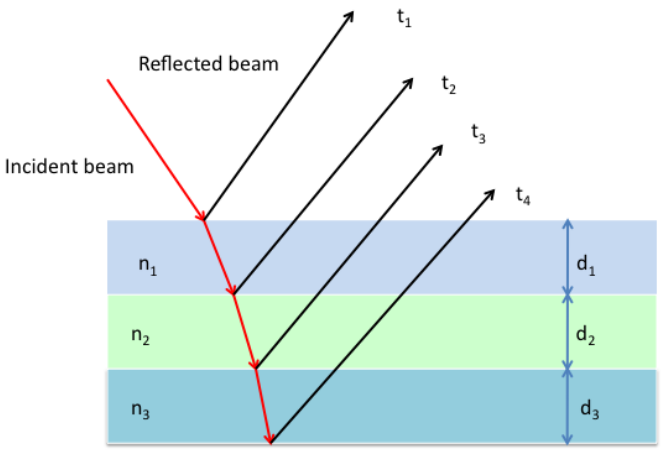

Figure 4.13: Layered system where each layer has different refraction index. For each interface a reflection occurs, detecting multiple peaks in the measurement. The difference between the opticals delays provides the width of the layers.

As early work, we have applied this methodology to determine the thickness of different layered peaces in vehicles. Furthermore, more aspects of Terahertz characterization will be discussed in the following sections.

Outer peaces of vehicles, e.g cars or ships, need different coatings in order to protect their integrity from weather, and ensure its functionality. Correct characterization in the formation of each paint or covering layer in the production phase,

is a crucial operation for the quality of the final product. These features involve a compromise between fast efficiency and large precision in the quality test. In the case of ships the coating importance lies in prevent the accumulation of mollusk or other aquatics. On the other hand, in the case of cars, it is to prevent the corrosion and ensure the correct protection of the chassis.

For these studies, it was used the information provided by reflection measurements, based on the optical delay analysis, it described by equation 4.5. Mini Z equipment can provide a large resolution, about 20 μm (corresponding to 0.1 ps resolution in the time domain), being an appropriate tool for layer analysis. The measurement protocol in the two cases was carried out as follows:

1. Mini Z equipment was placed at the top of the sample holder consisting of a metallic platform. This configuration was to work in reflection mode.

2. A metallic layer at the same position as the sample under study was placed. Because metallic materials present large reflection, this method allows to calibrate the position of the sample at the focal distance of the emitter as well as perform a reference measurement for the data analysis.

3. The sample was placed at the calibrate position and its reflection signal in the time domain was measured.

In all studied samples the time domain spectra showed different reflections peaks associated with each interface between layers. Nevertheless, the calculation of the width also depends on the diffraction index of the material where the THz wave travels. Hence a correct previous identification of this value should be necessary to obtain the thickness of inner layers that, in our case, ranged from 1.5 to 2.

Figure 4.14(a) depicts the time domain spectra for a hull of a ship and figure 4.14(b) for a piece of helm made with fiberglass. Data analysis, in the case of ship's peaces, has consisted in subtract the reference (metallic layer) to the measurement signal. A clean spectrum was obtained, in which different reflection peaks associated with the sample can be detected. The different layers found in the two systems were 0.79, 0.8 and 3.45 mm for sample 4.14(a) and 0.19, 0.558 and 3.49 mm for sample 4.14(b) in concordance with measured depths in the application of each paint.

As interesting remark, the first reflection peak, which was reflected by the first surface of the samples, had larger height than the other ones. This feature is due to the large difference between the refraction index of open air and the first surface.

On the other hand, results obtained for the car's chassis, with different coverings, revealed smaller layers than the previous case: 20 μm for sample 4.15(a) and 32.47 and 74.75 μm for sample 4.15(b). The experiments were carried on as the

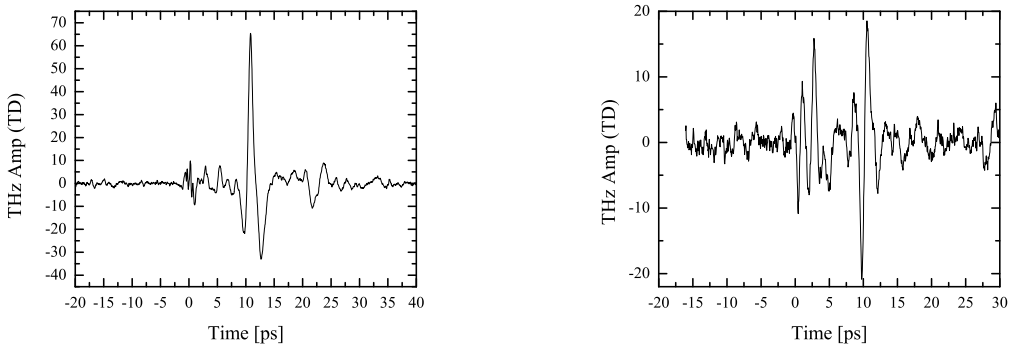

(a) Time domain spectra for a ship's hull.

(b) Time domain spectra for a helm' ship made with fiberglass.

Figure 4.14: Reflection peaks due to different coverings in ship peaces.

case of ship's peaces but the data analysis was more sophisticate due to the overlap between peaks, and an algorithm was needed to deconvolve the reflection signal of the samples with the reference signal of the metallic plate. This methodology was based on the fact that each reflection was a fraction of the total energy that emits the experimental equipment. Therefore, the deconvolution method computed the position of each layer and the fraction of the total energy that they reflect. Remarkably, the sum of all the computed reflection peaks equals to the total energy emitted by the terahertz source. The obtained x-axis in figures 4.15(a) and 4.15(b) corresponds to the optical delay referenced to the initial peak (associated with the first layer of the system), that is the value of Δt appearing in equation 4.5. As finally remark, the intensity of peak measured at zero optical delay (first reflection) showed a large reflection from the first layer, which indicated the metallic composition of the sample and a large difference in the refraction index between open air and the first surface, such as ship's peaces.

4.2.3. First approach to the permeation problem and medicals applications

In medical and pharmaceutical fields the main used T-rays techniques, are the Terahertz Pulsed spectroscopy (TPS) and imaging (TPI) [113], [81]. Particularly in pharmaceuticals, the strong vibrations and rotational modes of biomolecules can provide typical absorption resonances useful to the identification of active compounds present in the formulation [82], [119]; or in order to obtain information insight the structural dynamics of polymorphs [120] (crystallographic phases that a biomolecule can crystallized) and hydrates of crystalline materials [82]. TPS,

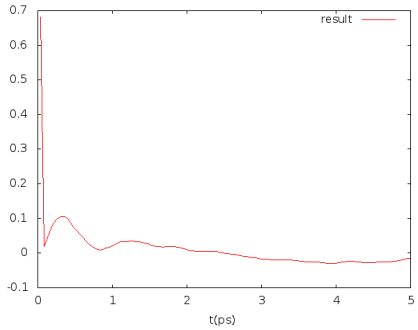

(a) Time domain spectra of a car's chassis, with two different layers, the inner chassis and the outer base.

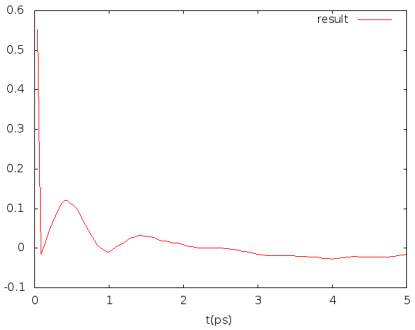

(b) Time domain spectra of a chassis car with three different layers: chassis, ktl and base.

Figure 4.15: Results for different car's chassis. In these measurements as the layers were thiner than the previous analized samples the reflection peaks overlap between them and a deconvolution algorithm was needed.The first peak at zero difference optical delay corresponds to the first reflection, revealing the metallic nature of both samples.

used in the cases mentioned before, consists in a transmission measurement of a THz pulse in a solid or liquid sample, it depending on the type of formulation. Solid samples usually are powders, and it is made a tablet of the formulation for the measurement. Then, the sample is placed in the sample holder between the emitter and the receptor (transmission measurement), and is applied the following protocol:

1. A reference measurement without sample is made in the time domain. Then, the Fourier Transform of the data is computed, between 0.3 and 3 THz.

2. The sample in the shape of a disk is placed in the sample holder, and a measurement in the time domain taken. The Fourier Transform is computed as the case of the reference measurement.

3. The absorption spectra between 0.3 and 3 THz is computed by the division of the frequency spectra of the sample and the reference.

Characteristic resonances are observed as maxima peaks, and their associated frequencies are the resonance frequency (frequency for which the sample absorbs the radiation). Furthermore, the measurement protocol for liquids is the same as for solids but using a special sample holder made with polyethylene, which is transparent in the THz band. In this sense, the study of characteristic resonances in drugs was our first step to consider the viability, and the usefulness of THz technology in the pharmaceutical field, using the techniques explained above. Figure

4.12 depicts real absorption spectra for three active molecules used in topic formulations, in addition to normal drugs: ibuprofen, 4.16(a), ketoconazol, 4.16(b), and methylglucamine, 4.16(c). The detected resonance frequencies were: 1.1 THz for ibuprofen, 1.9; 1.65, and 1.8 THz for ketoconazol , and 1.0 and 1.5 THz for methilglucamine. Therefore, the presence of such resonance frequencies in the absorption spectra of a multicomponent formulation inform us about those actives present in the formulation. Moreover, the height of the resonance peak can be associated with the amount of resonant compound taken part in the system. Hence, knowing the absorption spectra for different active molecules will be possible to identify the compound and its quantity in any formulation (as ATR-FTIR), in a clean way without any induced photochemical reaction. These properties are only achieved by THz radiation in front of actual characterization techniques , being a promise tool for medical and pharmaceutical applications.

Moreover, Terahertz medical applications have also been focused on clinical images of skin such as burn injures [121] and the detection of skin [122], [123] and lug tumors [83] by TPI. Traditional techniques for skin inspection are High Frequency Ultrasounds and Nuclear Magnetic Resonance with the following characteristics: high frequency ultrasounds present an axial and lateral resolution of 80 and 200 μm respectively, and a depth of 7 mm; but it do not provide chemical or lesions contrast. On the other hand, NMR only detects tumors bigger than 15 mm below the skin surface, although has better axial and lateral resolution than high frequency ultrasounds (19 and 78 μm) but lower penetration: 800 μm. Nevertheless, THz TPI on skin inspection [124] has 250 and 20 μm resolution laterally and axially correspondingly. Despite THz has a less penetration, its wavelengths are bigger than the dissipative structures conforming the different layers of skin, and is capable to differentiate injured tissues from normals providing spectroscopy information over 0.3 THz and 4 THz [125], [126], and less scatter than infrared and optical radiation.

The demonstration of medical applications of THz onto skin was started by E. Pickwell et al. where in their first works [127], by Finite difference Time Domain simulations (FDTD) demonstrated that skin can be interpreted by two layers, stratum corneum and dermis, differentiating between them by their water content (with different refraction index). This feature was corroborated in experiments with human skin [128]. The main conclusions of these experiments were that T-rays can penetrate the stratum corneum until the dermis, making possible the generation of images with TPI.

But the most important drawback for TPI and TPS is the presence of water as major component of biological tissues [129], and its high absorbency to THz radiation due to its six different vibration and libration modes [84]. For example in TPI is important to take into account the strong absorption by water, making

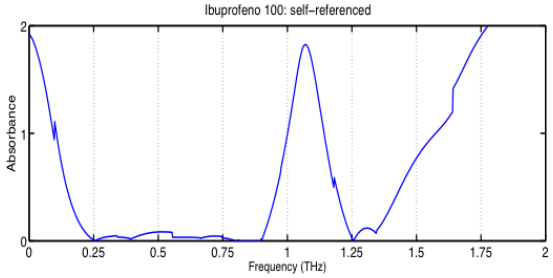

(a) Absorption spectra for ibuprofen.

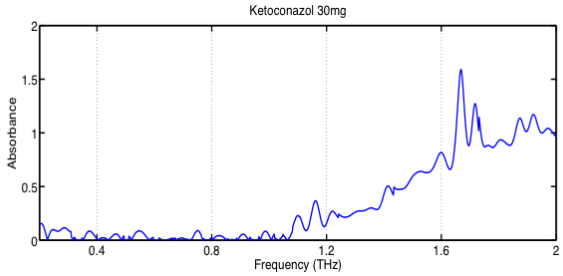

(b) Absorption spectra for ketoconazol.

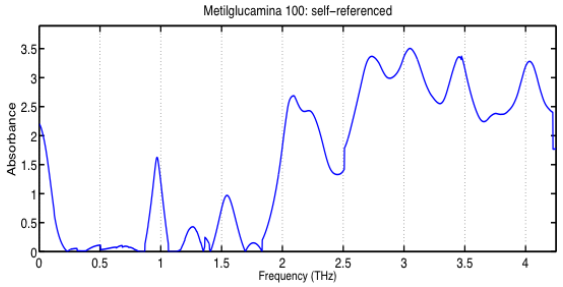

(c) Absorption spectra for metilglucamina.

Figure 4.16: Different resonance spectra for typical topic drugs.

whole-body imaging impossible. However the difference in the absorption due to water content makes a natural contrast to difference tissues, such as tumor and normal tissues [124].

4.3. Theoretical background of the diffusion process in porous medias

In this section, the theoretical basis of release mechanism will be exposed such as a thermodynamical process [130]. Let us assume the flux of a substance into a porous membrane, $\vec{j}$, is generated by a driven force such as a gradient pressure, or a gradient in the concentration of a diffusive substance applied on both sides of a porous medium. Such driven force generates a gradient in the chemical potential, μ, favoring the diffusion of the substance through the membrane, described as:

$$\vec{j} = \vec{\nabla}\mu \tag{4.6}$$

In a thermodynamical point of view, the chemical potential for a system with a pressure, and a concentration gradient becomes:

$$d\mu = RTd\ln(\gamma_i c_i) + v_i dP \tag{4.7}$$

being R the ideal gas constant, T the temperature,γ_i the activity coefficient, c_i the molar concentration, v_i the molar volume, and P the pressure. The chemical potential dependence on pressure and the solute's concentration makes possible to construct two different models: at uniform pressure or concentration gradient. For this reason it was performed two different experiments in the basis on the thermodynamic model: an active permeation process where the driven force was a pressure gradient, and a passive diffusion process, in which a gradient concentration was the driven force.

4.4. Experimental set-up for the study of diffusion processes with Terahertz radiation: materials and methods

Four pure excipients commonly used in the formulation of topical products were selected as simple cases in the experiments: propylene glycol, sweet almond oil, paraffin oil and PEG 400, which were purchased from Fargon Iberica. Their physical properties are summarized in table 4.4. A previous characterization of

the studied excipients was performed by spectroscopy analysis in order to detect possible absorption resonances. If a sample has resonance peaks, part of the received energy is absorbed and then the reflected signal would be attenuated. Spectroscopy results show that any excipient presented characteristic resonances in the frequency range used in the experiments, then energy was not missed in the interaction between the excipient and T-rays (as an example, in figure 4.17 it is showed the absorption spectra for sweet almond oil).

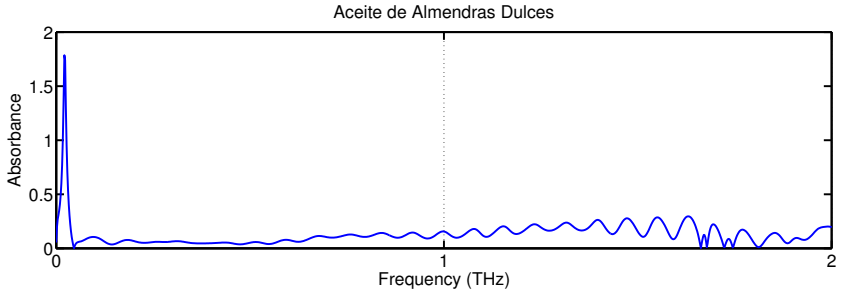

Figure 4.17: Absorption spectra for sweet almond oil. None representative resonances are observed in all the analyzed frequency range, except at low frequency (0.3 GHz).

Substance	**Density** g/cm^3	**viscosity** $mPa \cdot s$
Sweet almond oil	0.918	280
Propylene glycol	1.036	193.3
PEG 400	1.128	447.3
Paraffin oil	0.846	102.8

Table 4.2: Physical properties of the four excipients used in the experiments. Based on the magnitudes the substance with less viscosity is paraffin oil and, on the other hand, PEG 400 with the larger viscosity, then is expected that paraffin oil should be the substance that diffuse faster than the other three.

The permeation rates of the four selected substances were assessed in four different membrane materials: cellulose, PVDF, and nylon with a specific nominal porous size of 0.45 μm, and a additional membrane of nylon with a nominal porosity of 0.22 μm. The respective membrane thickness were 0.16, 0.14, 0.09, and 0.15 mm. At last, two single experiments with human abdominal skin were also conducted using abdominal human skin samples.

The principle of operation of using a THz time-domain system to measure the diffusion of a excipient through a membrane is based on measuring the changes in the position of the THz pulse reflected by the surface of the substance located on the donor side of the membrane. In the determination of the thickness of

layered systems, it was demonstrated that the distance between the emitter and the receptor followed equation 4.4. Let us assume that at the top of a porous media is placed a liquid, contained in a drop, whose reflected THz pulse is detected at optical delay t_1. During the experiment the drop transfer its mass to the porous media, reducing the height of the drop. This dimensional variation should be detected in the reflection time domain measurement as a change in the optical delay of the reflected signal, t_2, being $t_2 > t_1$. It is clearly seen by equation 4.4 that this change in the optical delay is associated with the dimensional variation of the drop, or in other words the distance between the emitter/receptor and the donor is increased as the mass is transfered. Therefore, using equation 4.5 is possible to compute at different times the height of the drop. Taking into account these features the measurement protocol for all the experiments is:

1. The position of the membrane is measured as reference in the absence of sample (optical delay t_1).

2. A controlled volume of sample is dropped on the membrane that shifts the position of the reflected pulse to a different optical delay, t_2. This fact reflected the shorter distance between the system and the surface of the sample.

3. As the volume of the donor diminishes because it permeates into the membrane, the optical delay of the pulse shifts accordingly.

4. Once the sample is completely absorbed into the membrane, the position of the pulse returned to the original position.

5. Data analysis is in the basis on equation 4.5.

With this experimental protocol three experiments were performed depending on the driven force that actuates on the excipient (based on the thermodynamical model): active, passive, and percutaneous permeation experiments. The driven force in the active permeation experiments was a pressure gradient, and they were tested the four excipients. In the passive permeation experiments, it was only studied propylene glycol and PEG 400 because they were soluble in the saline solution, and therefore compatible with the Franz cell set-up. Finally, in the percutaneous permeation experiments only propylene glycol was assessed on human skin in the Franz cell configuration.

To smear out error sources in the measurements of those excipients used in the lasting experiments (passive permeation experiments and percutaneous experiments), an assessment of the risk of evaporation of propylene glycol, PEG 400, and ethanol (as positive test) were performed. For these measurements, a cylindrical

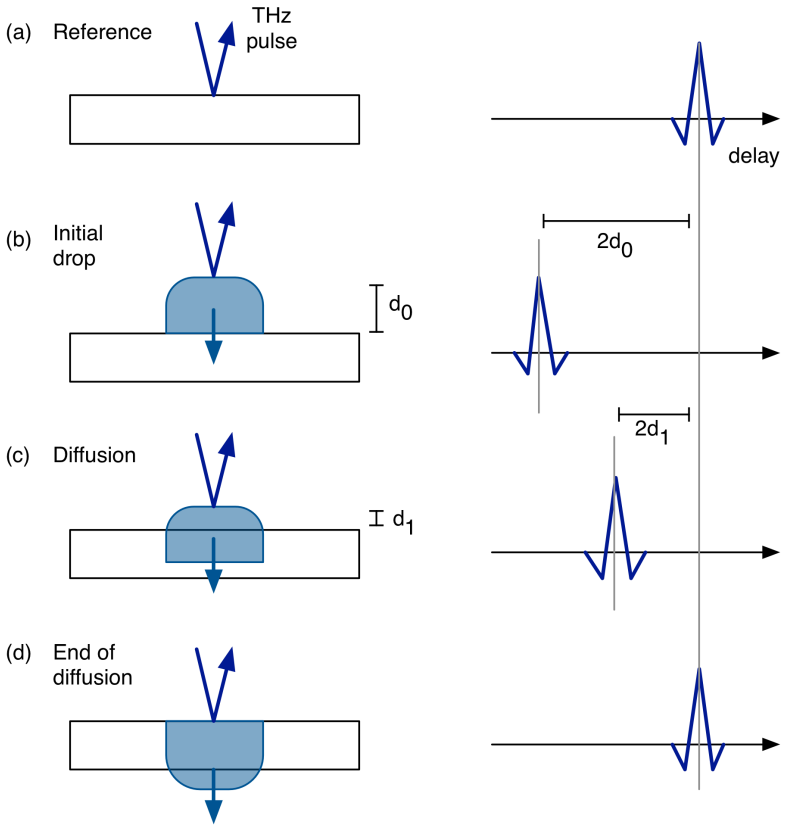

Figure 4.18: Principle of operation of the diffusion process of the excipients with a THz time-domain system. a) Reference measurement of the position of the membrane. b) Pulse position when the excipient is placed onto the membrane. c) Diffusion process as measured by the shift of the position of the THz pulse. d) End of the diffusion process in which the excipient has completely diffused, and the position of the THz pulse returns to the reference.

metallic bracket (20.7 mm) replaced the membrane below the Mini-Z at the same distance. The product of the computed height using equation 4.5, and the surface of the bracket provides the volume of the donor as a function of the time. The experiments started by placing 600 μL of sample inside the metallic beaker, and lasted for 30 hours or until sample exhaustion. The results of the evaporation test (see figure 4.19) suggest that neither propylene glycol nor PEG 400 evaporated significantly during our experiments. The positive control, ethanol, evaporated quickly with a rate of 1.5 $\mu L \cdot mm^{-2} \cdot h^{-1}$.

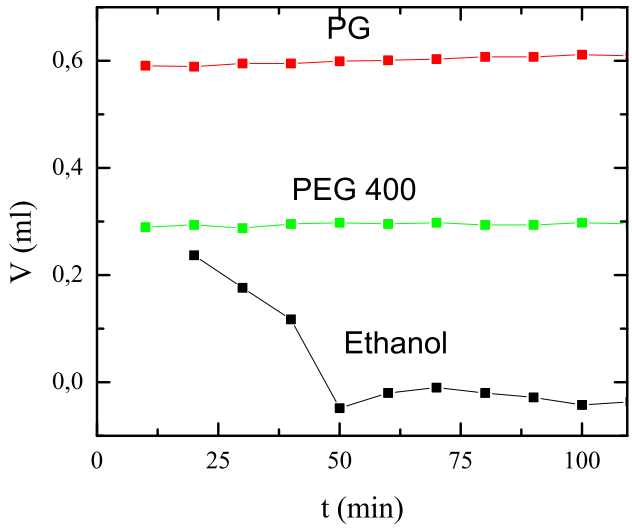

Figure 4.19: Evaporation changes in the volume profile of propylene glycol, Peg 400, and ethanol as positive control. In all the duration of the experiment, propylene glycol and PEG 400 do not evaporate. As counterpart, the reduction of ethanol by evaporation is detected.

4.5. Active permeation experiments

In the pressure-driven set-up (figure 4.20), a vacuum pump was connected to the receptor side of the membrane to create a differential pressure between both sides of the membrane. For each test, 200 μl of sample was placed on the donor side at atmospheric pressure, and forced to permeate through the membrane at different pressures ranging from 10 to 60 $mm\ Hg$.

The experimental protocol was the same explained before, and the data acquisition was carried out by a hand-made computer program, which recorded the evolution of the height of the drop every 6 seconds. In order to increase signal-to-noise ratio (SNR) 20 reflected signals were collected for each measurement, and the optical delay of the mean was used to compute the height of the drop. The height is expressed as the percentage with respect to the initial height to correct for a slight variation in the initial volume between different experiments. In figure 4.21 is shown the real evolution of the signal in a single experiment.

With the pressure driven set-up fifteen different experiments were performed. But for simplicity in this chapter we will only show the results for propylene glycol in the nylon membrane (figure 4.22). The rest of results are summarized in appendix B.

As first interesting fact, in some cases a bending of the membrane was observed

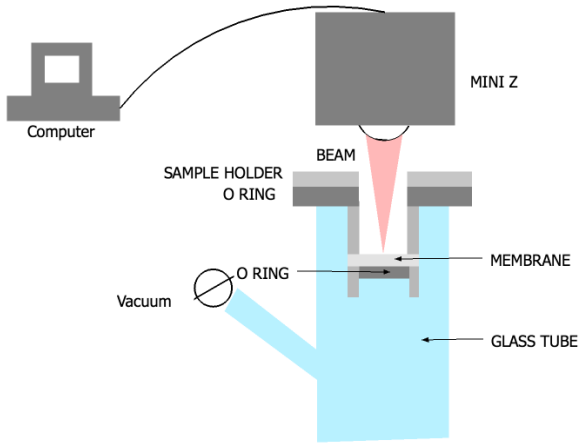

Figure 4.20: Scheme of the sample holder made for active permeation experiments. The sample holder consisted in a tube where at its top the membrane is placed. The bottom of the membrane is connected to a vacuum pump in order to apply a differential pressure on the two sides of the membrane.

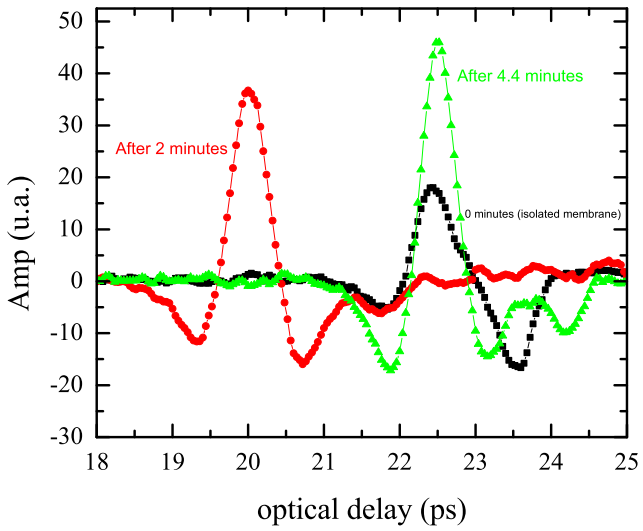

Figure 4.21: Real evolution of the reflected signal in one of the performed experiments. Black line represents the reflected signal of the isolated membrane, red line after 2 minutes of seeded the drop, and green line after 4.4 minutes, when the substance has passed through the whole membrane. As time passes the optical delay reached its initial value.

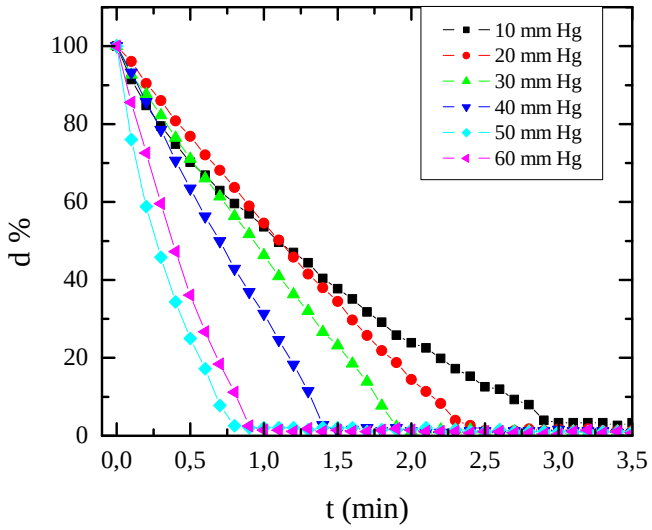

Figure 4.22: Distance profile of propylene glycol in nylon at different pressures. The y-axes is normalized as a function of the initial height of each drop in all the experiments, allowing a direct comparison between the assessed pressures.

at the end of the experiment, causing an offset between the starting and ending position of the THz pulse. This effect was corrected applying a baseline correction method. Secondly, typical permeation experiments, usually, present two regimes in the evolution of the concentration profile as a function of time: a sigmoid curve that corresponds to the membrane saturation by the donor, and a linear regime corresponding to the saturated permeation. But, in all the measured pressure regime, the height of the drop decreased linearly for most of the duration of the experiment suggesting only a saturate phase (as we will show later the flux corresponds a saturate phase). Therefore the excipient saturated the membrane in a lower time than the experimental time window, 6 seconds. Finally, the rate of each permeation process increases with rising the pressure and the duration of the diffusion process becomes shorter.

The flux of each substance (mass per surface and time unit) at the top of the membrane was computed using the thickness change rate that the height of the drop diminished, given by:

$$j = \frac{1}{A}\frac{dm\,(t)}{dt} \tag{4.8}$$

where j is the flux, A is the surface that the donor permeates, and dm is the mass that is transferring to the membrane. For an homogeneous donor, and an uniform, we use the density mass in equation 4.8, $\rho = \frac{dm}{dV}$, and a cylindrical shape

for the drop (with volume $V = A \cdot h$, where A is the surface of the cylinder and h is the height):

$$j = \frac{\rho}{A}\frac{dV}{dt} = \frac{\rho A}{A}\frac{dh\,(t)}{dt} \tag{4.9}$$

Taking into account that $dh\,(t)\,/dt$ is the velocity, which the drop diminish, v, equation 4.10 turns out in:

$$j = \rho v \tag{4.10}$$

Then, the slopes of the height profiles are related with the velocity of the process, v, considering that these velocities are constant. The flux, j, was obtained using equation 4.10.

Before presenting the computed fluxes as a function of the applied pressure, and in order to go deeper on the understanding of the results, first we will solve equation 4.6. In the studied case of the pressure driven force, the concentration gradient in the membrane was zero due to the fast initial saturation stage (deduced from the distance profile, figure 4.22) and then the whole system remained with a constant concentration. Consequently $d\ln(\gamma_i c_i) = 0$, and equation 4.6 becomes:

$$\vec{j} = -Lv_i\vec{\nabla}P \tag{4.11}$$

in the case of an uniform gradient of pressure and computing the integral for a membrane of thickness l, we obtain the so-called pore-flow model or Darcy's law:

$$j = \frac{k\Delta P}{\eta l} \tag{4.12}$$

where k is the Darcy's coefficient, ΔP is the applied pressure, η is the viscosity of the substance, and l is the thickness of the porous media. The introduction of the viscosity in equation 4.12 comes from hydrodynamics or the pore-flow model that describes in accurately way the flux of a substance through a porous media. In the model, each pore is assumed as a cylinder of radius r, where the flux of any substance through them is described by the Poiseuille flux, $j = \frac{\pi r^4}{8\eta}\frac{\Delta P}{l}$, where η is the viscosity of the substance, ΔP is the pressure gradient, and, l the height of the cylinder. Porous membranes are modeled by a distribution of pore sizes, $f\,(r)$, that is the probability that a pore has a radius between r and $r + \Delta r$. Then, the total flux for the membrane becomes:

$$J = \int_{r(\Delta P_{min})}^{r(\Delta P_{max})} j f\,(r)\,dr \tag{4.13}$$

where at this moment we distinguish between the total flux through the membrane J, and the flux through each pore, j. The limits in the integral are related

to the conviction that exists a minimum pressure to active the flux through the pore, for which below this pressure it is not possible establish the flux. Knowing the porous distribution a direct model for Darcy's coefficient can be extracted, but size distributions of currently membranes are difficult to obtain. Nevertheless, it is possible to introduce the dependence on the viscosity in equation 4.12, as seen in this last model.

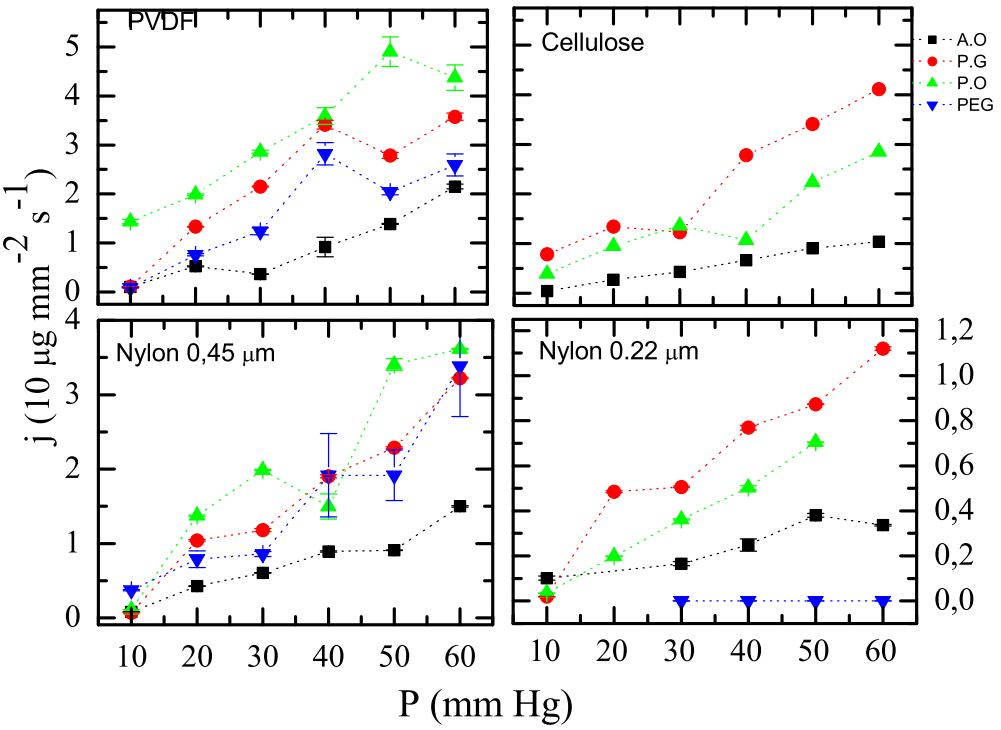

Figure 4.23: Flux deduced from each experiment as a function of the applied pressure. In all the cases the flux has a linear dependence on the differential pressure, as Darcy's law predicts. The fastest donors are paraffin oil and propylene glycol. On the other hand the slower PEG 400.

Figure 4.23 depicts the computed flux for each excipient and membrane (equation 4.10) as a function of the differential pressure. First, the inverse effect of the nominal porosity over the resulting flux is clearly shown in the case of the 22 μm nylon membrane: the obtained fluxes were lower than using the 0.45 μm nylon membrane. On the other hand, the results clearly show a linear relationship between flow rate and the vacuum pressure, fully compatible with Darcy's law (equation 4.12). Deviations of the Darcy's law may have their origin in physicochemical interactions between the excipient and the membrane, changes in the pathway such as tortuosity (effective length that cross the substance inside the membrane), or specific properties of the permeating excipient. As expected, ex-

cipients with low viscosity diffuse faster, paraffin oil. As counterpart, the excipient with large viscosity, PEG 400, presented the lowest flux values, even it did not flow through the smallest pore size membrane.

Because Darcy's coefficients provide the characteristic information of the diffusion process of a substance through a porous media, they were computed using a linear fit of the fluxes as a function of the differential pressure:

$$\sigma = \frac{k}{\eta l} \tag{4.14}$$

where σ is the slope of the fit, k is the Darcy's coefficient, η is the viscosity of the substance and l is the length of the membrane. The different deduced Darcy's coefficient are summarized on table 4.5.

Substance	**Membrane**	**Darcy's coefficient** (10^{-5} $\mu g\ mm^{-1}$)	10^{-5} **standard error**
Paraffin oil	Cellulose	3.0	0.4
	Nylon	8.0	0.1
	Nylon 0.22	1.9	0.4
	PVDF	8.9	0.2
Propilen nglycol	Cellulose	3.0	0.3
	Nylon	5.9	0.5
	Nylon 0.22	2.2	0.6
	PVDF	12.2	0.2
Sweet almond oil	Cellulose	3.8	0.3
	Nylon	7.3	0.9
	Nylon 0.22	1.5	0.7
	PVDF	4.5	0.1
PEG 400	Cellulose	-	-
	Nylon	12	1
	Nylon 0.22	-	-
	PVDF	30	2

Table 4.3: Values of the Darcy's coefficient extracted from the linear's fits of figure 4.23.

Based on our data, Darcy's coefficients for PEG 400 were higher than those for substances with lower viscosity. This result reflects the influence of the mass density on the flux (the flux is directly proportional to the mass density). As final interesting remark, representing the slope of each linear fit as a function of the viscosity, a $\frac{1}{\eta}$ law is founded (see figure 4.24). Consequently the computed transport coefficient followed the structure deduced from Darcy's law, equation 4.14, validating the results.

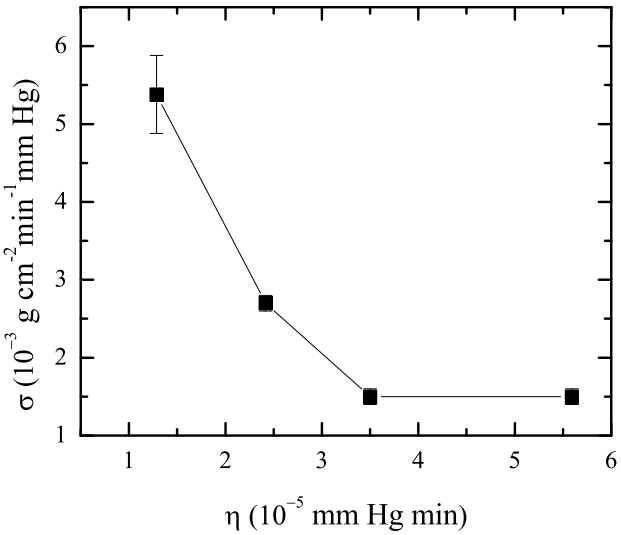

Figure 4.24: Transport coefficient (slope) extracted of the linear fit of the flux plotted as a function of the viscosity, in nylon membrane. In the graph is observed a $1/\eta$ law as described in Darcy's theory.

Therefore our system was capable to measure in a non-contact way the diffusive flux of a topical excipient through a membrane due to a negative pressure, and recreating the theoretical Darcy's law.

4.6. Passive permeation experiments

For the concentration-driven setup, figure 4.25, a vertical diffusion cell was employed, ensuring sink conditions. The membranes (only tested in this experiment PVDF, and 0.45 μm nylon membranes) were previously soaked in saline solution for half an hour to provide adequate flexibility and remove unexpected impermeabilities. After soaking, the membranes were carefully wiped before being mounted on top of the cell. The receptor compartment was filled with a physiological saline solution, and was continuously stirred to ensure that the solution was homogeneous. Only the hydrophilic excipients soluble in saline solution (propylene glycol and PEG 400) were used in order to comply with the sink conditions. In this case, large volumes of excipient (600 μL) were used, covering the entire effective diffusion area. This procedure ensured a constant diffusion regime throughout the entire duration of the experiment.

In figures 4.26(a), 4.26(b), 4.27(a) and 4.27(b) the results from the passive permeation of propylene glycol and PEG 400 onto nylon and PVDF are represented.

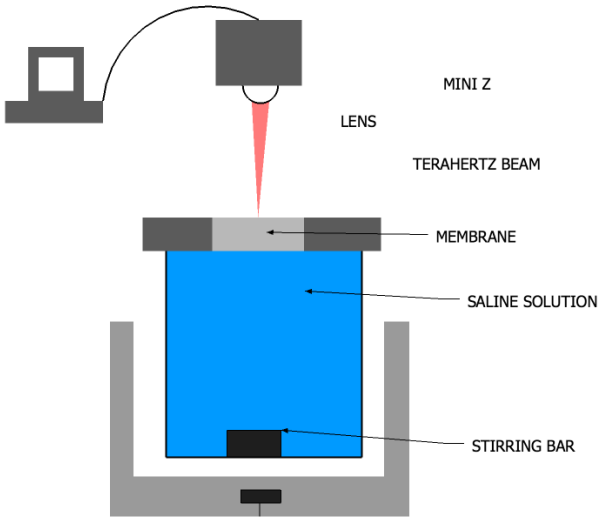

Figure 4.25: Scheme of the diffusion cell where the experiments of passive diffusion were carried out.

Two different regimes are observed in the figures: an earlier phase of penetration of the excipient into the membrane, and a quasi-linear diffusion phase that can be considered constant near the inflexion point.

The first regime can be explained as the saturation process of the membrane, and the second one may consist of the stationary permeation across the saturated system. To go deeper on the understanding of our experimental data, equation 4.6 was taken up again, considering that any gradient of pressure was applied in the system, $dP = 0$:

$$\vec{j} = -\frac{RTL}{c}\vec{\nabla}c \tag{4.15}$$

if the diffusion only occurs in one direction with uniform concentration gradient, $\vec{\nabla}c = cte$, equation 4.15 becomes in equation 4.16 (Fick's first law):

$$j = -\frac{D}{l}\Delta c \tag{4.16}$$

where D is the diffusion coefficient defined as $D \equiv \frac{RTL}{c}$, and l is the thickness of the membrane. Equation 4.16 is only restricted for the case on which the concentration gradient is constant. When the concentration gradient also depends on temporal variations, it is necessary to solve the general diffusion equation:

$$\frac{\partial c}{\partial t} - D\vec{\nabla}\vec{j} = 0 \tag{4.17}$$

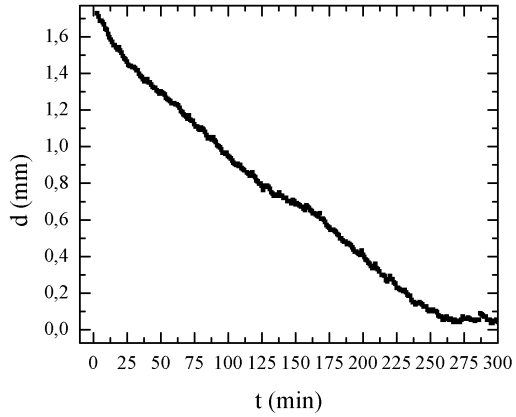

(a) Transfered mass of PEG 400 to a PVDF membrane as a function of time.

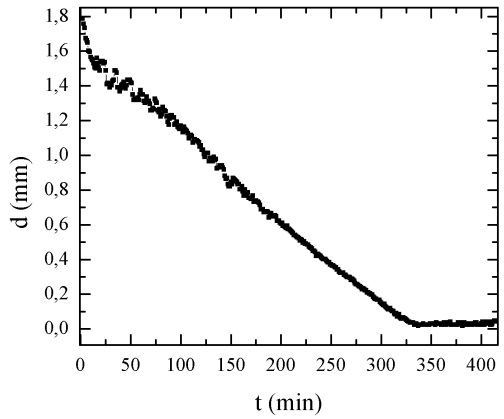

(b) Transfered mass of propylene glycol to a PVDF membrane as a function of time.

Figure 4.26: Distance profile for PEG 400 and propylene glycol into PVDF porous media. Two different regimes are clearly seen in the plots.

Using the general form of first Fick's law (equation 4.15) in equation 4.17 the second Fick's law is obtained:

$$\frac{\partial c}{\partial t} - D\vec{\nabla}^2 c = 0 \tag{4.18}$$

Nevertheless, Higuchi [131] demonstrated that in a drug release process the mass ratio at the receptor side from a semi-infinite medium, in saturation, can be described as:

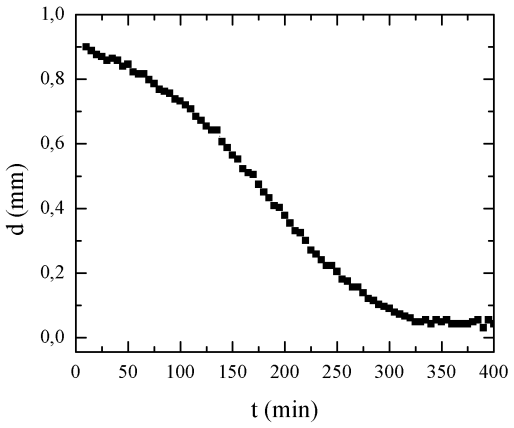

(a) Transfered mass of PEG 400 to a nylon membrane as a function of time.

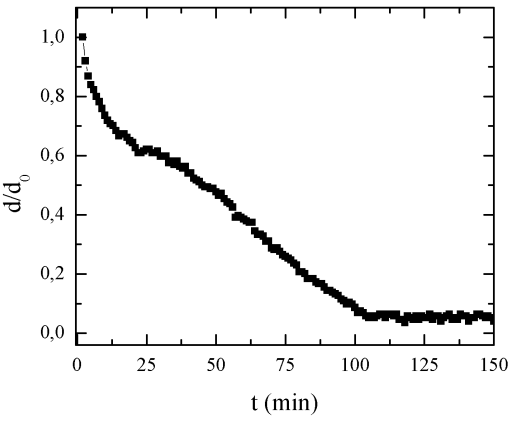

(b) Transfered mass of propylene glycol to a nylon membrane as a function of time.

Figure 4.27: Distance profile for PEG 400 and propylene glycol into PVDF porous media. Two different regimes are clearly seen in the plots.

$$\frac{M_R}{M_o} = 2\sqrt{\frac{Dt}{\pi d_o^2}} \tag{4.19}$$

where M_R is the mass of the substance at the receptor site, M_o is the initial mass of the donor, D is the diffusion coefficient, and d_o is the initial height of the volume of the donor. Consequently, this solution allows to obtain the diffusion coefficient only measuring the arriving mass at the receptor chamber in a permeation experiment. In our experiments, the dimensional changes can be related to the

changes in the amount of substance of the donor. In particular, the initial mass for a mono-component formulation is given by:

$$M_0 = d_o A \rho \tag{4.20}$$

being A the surface of diffusion and ρ the density of the excipient. Moreover, the mass at the receptor side can be computed by:

$$M_R(t) = M_o(t) - M_D(t) \tag{4.21}$$

where M_D is the amount of substance pending to pass the membrane. Therefore using equations 4.20 and 4.21 in equation 4.19, the mass rate at the receptor side becomes:

$$\frac{M_R(t)}{M_o} = 1 - \frac{d(t)}{d_o} = 2\sqrt{\frac{Dt}{\pi d_o^2}} \tag{4.22}$$

To sum up, equation 4.16 can only be applied to obtain the diffusion coefficient in the stationary state. In other regimes, equation 4.15 best describes the diffusion, and the saturation of the membrane. However, in a pharmaceutical point of view equation 4.19 is the best theoretical model to describe a permeation process, and for this reason, we used the adapted form (equation 4.22) to describe our experiments in basis on dimensional variations of the donor.

Consequently, the results exposed above were represented as relative dimensional variations respect the initial height as a function of the square of time, as seen in figures 4.28(a), and 4.28(b) for the PVDF membrane, and 4.29(a), and 4.29(b) for the nylon membrane.

As seen in figures 4.28(a), 4.28(b), 4.29(a), and, 4.29(b), the second regime observed in figures 4.26(a), 4.26(b), 4.27(a), and 4.27(b) fit the square root model with a regression coefficient of the 0.99. Therefore, fitting the data with equation 4.22 the diffusion coefficient for the four measured process can be extracted, they summarized in table 4.6.

Substance	**Membrane**	**Diffusion coefficient** $10^{-4}\ mm^2\ s^{-1}$	**Standard error**
PG	nylon	2.06	0.04
	PVDF	2.64	0.02
PEG 400	Nylon	1.23	0.03
	PVDF	4.425	0.007

Table 4.4: Computed diffusion coefficients for each excipient across PVDF and nylon membranes.

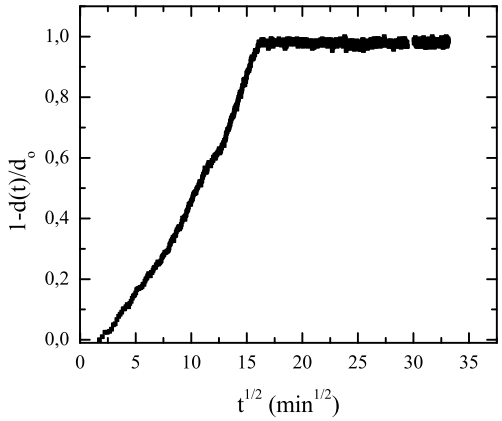

(a) Transfered mass of PEG 400 to a PVDF membrane as a function of the square root of the time. The results show a linear fit in the second regime, as equation 4.22 predicted

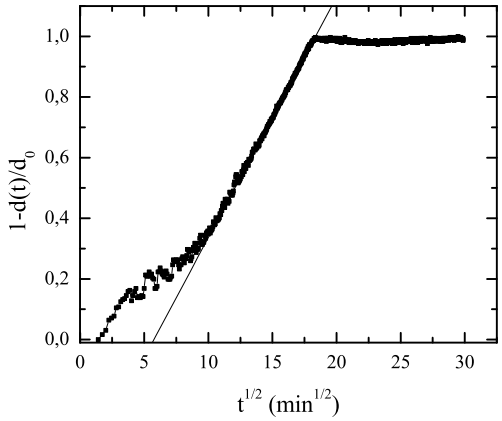

(b) Transfered mass of propylene glycol to a PVDF membrane as a function of the square root of the time. The results show a linear fit in the second regime, as equation 4.22 predicted

Figure 4.28: Fit of the results of PG and PEG 400 diffusion process represented in figure **??**. In the two cases the second regime detected in the permeation process of each substance fitted with equation **??**

Based on the results showed in table 4.6, PVDF membranes seem to be better for the diffusion than nylon membrane. These results could be used as the basis for the membrane selection test, and to predict the release properties of an excipient.

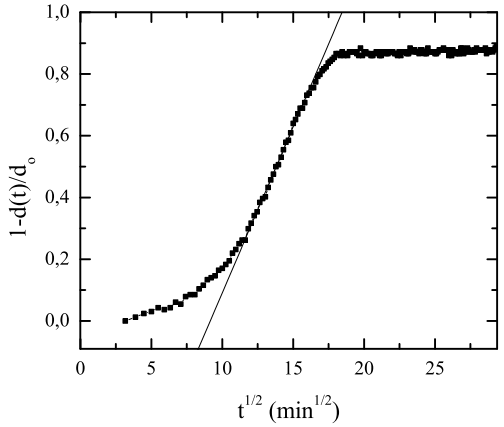

(a) Transfered mass of PEG 400 to a nylon membrane as a function of the square root of the time. The results show a linear fit in the second regime, as equation 4.22 predicted

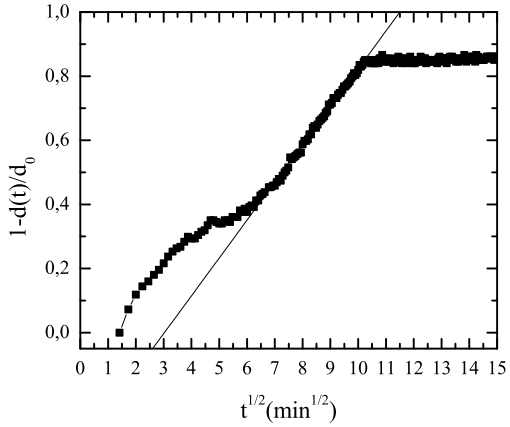

(b) Transfered mass of propylene glycol to a nylon membrane as a function of the square root of the time. The results show a linear fit in the second regime, as equation 4.22 predicted

Figure 4.29: Fit of the results of PG and PEG 400 diffusion process represented in figure **??**. In the two cases the second regime detected in the permeation process of each substance fitted with equation **??**

Finally, both studied release mechanisms are related between them, as reflect equation 4.6. At saturated regime, active and passive permeation occurred at constant concentration gradient, where the passive flux should also follow Darcy's law.

Using the transport coefficient of the pressure-driven permeation, we compute the equivalent driving force (in mm Hg) of the sink receptor of the diffusion cell across nylon and PVDF membranes. The results indicate an equivalent pressure of 0.22 and 0.07 $mm\ Hg$ for PG, and 0.28 and 0.21 and $mm\ Hg$ for PEG 400 across both membranes. These values fall below the range of pressures of the vacuum experiments, but they give an idea of the intensity of the diffusion dynamics associated with the concentration gradient experiments.

The main conclusion of the previous is: THz radiation can characterized with a large precision any in vitro diffusion process. This feature makes a simple and fast test to determine the selection of the best excipient for a preliminary in vivo test.

4.7. Percutaneous permeation experiments

Percutaneous permeation experiments were performed in two real skin samples in the Franz cell configuration. The samples were abdominal human skin obtained from plastic surgery, as seen in figure 4.30, and they have been dermatomed to 400 μm. Skin samples were thawed in isotonic saline solution at 25 ^{o}C for 6 h.

Figure 4.30: Skin sample used as native skin.

Due to the limited number of samples, we decided to only use one excipient, propylene glycol owing to its solubility in the saline solution, and its reduced viscosity. Two samples of skin, non-soaked (native skin) and soaked skin (pretreated

skin) were used in the experiments. As in the experiments of passive diffusion, 600 μl of propylene glycol were pipetted onto the skin. The results for native skin are presented in figure 4.31.

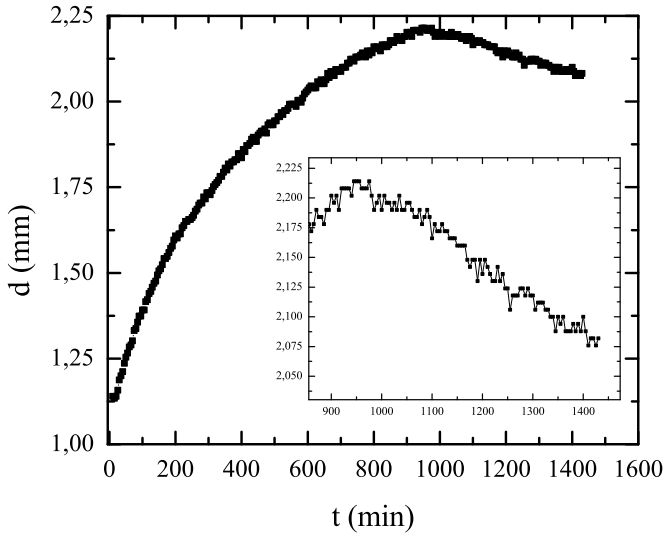

Figure 4.31: Measured distance profile for propylene glycol into skin. The data show two phases: firstly, skin and donor rises for 1000 minutes. Afterwards its height becomes smaller. In the inset is represented the dimensional variation in the phase detected by the experimental equipment.

Based on our data, the height of the donor volume unexpectedly rose for 1000 *minutes*. Afterwards a quasi-linear diffusion phase is observed. The most plausible explanation for this dramatic increase in the donor height could be that the skin swelled when entering into contact with the propylene glycol. In the previous experiments using synthetic membranes, the incoming amounts on the receptor side did not generate swelling because the simpler and thinner structure of the membrane. In addition, swelling of the epidermis membrane is a well-known effect [132], [133], although the extent of this swelling was unexpected. Nevertheless, after this initial swelling, the height variations evolved into a diffusive process similar to that observed with artificial membranes in the concentration gradient experiments.

As a confirmation of the skin-swelling hypothesis, an experiment was performed using skin previously soaked in propylene glycol for 6 hours. Afterwards, pretreated skin was mounted on the diffusion cell, and a donor formulation of 600 μL was seeded to observe the diffusion of propylene glycol; as shown in figure 4.32.

The results also show a first phase where the skin swell (the swelling phase

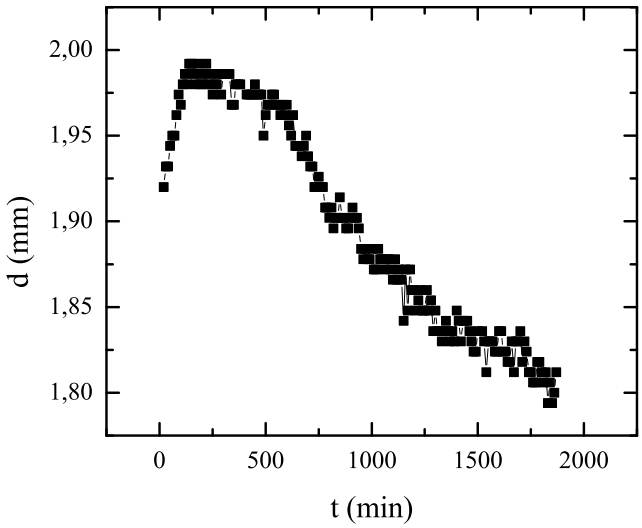

Figure 4.32: Distance profile for skin previously soaked in propylene glycol. Another time it was detected a first stage where the system increases its high respect to the emitter of THz radiation. After that, the donor started to diffuse in the same regime as detected for artificial membranes.

was around 0.1 mm) but with a lowest extension on time (round 300 minutes). The discrepancies should only be related to the previous treatment in the skin. When the soaked process was previously made into propylene glycol, skin has absorbed a certain amount of excipient, and saturated permeation should only be expected. When propylene glycol was dropped in the saturated skin another phase exist, little different from the saturation, where the exceed of donor should diffuse another time in the system. When the exes of donor is equilibrated, the diffusion process restart revealing a expected diffusion phase at constant flux.

Considering only the height decrease after the swelling, measured permeation rates for the intact and soaked skin samples are 317 μm per day and 180 μm per day, respectively. Sato et al. [134] measured a rat skin permeation level of propylene glycol of 65 mg/cm^2 per day. Using the density of propylene glycol, this permeation level corresponds a volume flux of 62 $\mu L/cm^2$, which represent a displacement of 617 μm per day. In addition Bowen et al. [135] obtained a similar result, 76 $mg/cm^2$of propylene glycol per day, which is equivalent to 760 μm per day. Those results are remarkably reliable assuming the known differences between human skin and rodent skin. Similarly, we have obtained a reliable permeation level of propylene glycol across human skin of 18.13 mg/cm^2. Therefore, values obtained in our experiments are consistent with the existing in the literature.

4.8. Conclusions

In this chapter new and interesting applications of terahertz radiation were presented in a wide range of fields like tagging, material inspection, drug identification and specially in the permeation problem of topic drugs into skin. Two properties were important in our studies, the potential spectroscopy due to the wide range of biomolecules that present different resonances in the Terahertz band, and the capability of detecting micrometric spatial variations. As interesting example, car's chassis and ship's peaces were studied using the optical delay method to determine the different layers that composed each sample. The importance of this application resided in the fast and precise method to ensure the quality of the final product.

In the pharmaceutical field, it has previously been examined the detection of current drugs used in topic formulations by their characteristic absorbance spectra in the THz band. Those resonances have their origin in vibrational and rotational molecular modes. On the other hand, actual techniques to characterize the permeation problem of topic drugs onto skin have been reviewed (Diffusion cell, ATR-FTIR, and skin stripping) , of which it was established their different usefulness and their drawbacks. In general these techniques are invasive and destructive, however, in the case of diffusion cell and ATR-FTIR, their applicability is only in vitro.

Our approach to the permeation problem with T-rays consisted in four different excipients typically found in topical formulations that were examined by terahertz radiation: propylene glycol, sweet almond oil, paraffin oil and PEG 400. The excipients present different densities and viscosities to study several fluids with different physical properties and without any characteristic resonance in the THz band, ensuring the compatibility in the combination of the detection of active molecules in future studies with topic formulations.

The first set of experiments focused on analyzing the diffusion process of all commented excipients in four different membranes as a function of a differential pressure applied at both sides of the membrane: PVDF, nylon, and cellulose with a mean porous size of 0.45 μm and another nylon membrane with 0.22 μm porous mean size. The results showed a linear decrease in the height of the excipient on the membrane. The diffusion process became shorter while the differential pressure was increasing. With this data, a flux was possible to compute having a linear relation with the applied pressure as Darcy's law predicted for this diffusion process.

Afterward, a more realistic experimental set-up was used, where a diffusion cell promoted a gradient of concentration as driven force. In this case, only the substances with larger and shorter viscosities were studied: propylene glycol and PEG 400, in PVDF and nylon membranes. Because the passive permeation was a slower process than the active permeation studied previously, a first regime was

detected where the substance saturates the membrane under study, whereas the second regime corresponds to the diffusion at constant concentration gradient. Studying the dependence of the second observed regime on time, it was possible obtain the diffusion coefficient of the two substances on the two studied membranes. The permeation results obtained in both studies have been compared in terms of equivalent driving force. We have shown that the driving force of the sink compartment is lower than the minimum vacuum that it was possible to apply in our setup.

Finally as a proof of concept, it was tested our measurement system in real human skin with propylene glycol. The main barrier in skin is the stratum corneum, a layer with 200 μm of thickness. Therefore, terahertz radiation is perfect to study, in real time, the permeation of topic drugs. Nevertheless, the data showed a first stage where skin swearing due to the effect of the propylene glycol. Afterwards a diffusion process was observed. Consequently, it was performed another experiment in which skin was previously soaked in propylene glycol to ensure its saturation. The data described another regime where the total height of the system increased, but it was shorter than in the previous experiment. As a consequence, not only the permeation process of a topic drug would be studied using terahertz radiation, but also how the substance interacts with skin.

In conclusion, the proposed technique provides a real-time, non-contact, and non-destructive method to measure the transport properties of an excipient through a membrane. Terahertz opens a new range of interesting applications and a new era in the pharmaceutical field, where in vitro and also in vivo permeation experiments will be achieved. These techniques provide a faster and more rational approach to assess the combination of excipient, and membrane that yields the best discriminant release conditions.

Chapter 5

General Conclusions

This thesis has shown new magnetic phenomena on magnetic and metallic nanoparticles due to finite size effects, their interaction with high frequency radiations, and new interesting, non-invasive, and non-ionazing applications in material science, pharmacy and medicine using the emerging terahertz technology. Our goal was to demonstrate how nanomagnetic systems interact with oscillating fields at kilohertz, gigahertz frequencies, and the role of finite-size effects on their magnetic response at DC and ac magnetic fields. Finally the proof of concept of future technological applications at terahertz frequencies has been shown.

In chapters 1, 2, and 3, was shown that finite size effects are crucial in the magnetic properties of magnetic nanoparticles as well as their interaction with high frequency radiations. First, the colossal reduction in the Curie temperature of $CoFe_2O_4$ nanoparticles (chapter 1) illustrates a new phenomenon related to finite size effects. The distortion observed in the crystallographic structure in nanoparticles with a mean size diameter below 3 nm modifies the interaction among the atoms forming the nanoparticles. Consequently, the Curie temperature reduces until 10 K that represents a reduction round the 90 % respect bulk material. In addition to all the experimental techniques used in this study, such as TEM, XRD or EDSX, one of the crucial experiments to understand this phenomenon was the study of the in-phase and out-phase component of the magnetization as a function of the frequency of an oscillating magnetic field (whose frequency was between 1 Hz and 1 kHz). It turns out that the interaction of magnetic nanoparticles with electromagnetic radiation or oscillating magnetic fields provides fundamental information of the magnetic properties of magnetic nanoparticles. Moreover, we have presented the new interesting case where the Curie and the blocking temperature of a ensemble of magnetic nanoparticles have a similar value.

Secondly, and to go deeper in the understanding of the interaction of magnetic nanoparticles with high frequencies, in chapter 2, it was studied the interaction of magnetite nanoparticles and manganite microparticles with microwaves on copla-

nar transmission lines. The use of this two different sizes relies upon study finite size effects, and the magnetization dynamics of magnetic systems at microwave frequencies. In the two systems, it was observed an absorption of the microwaves at zero field, and at different fields corresponding to the ferromagnetic resonance. This resonant absorption of the microwaves at zero field by the the magnetite nanoparticles was associated with the ac-susceptibility of the superparamagnetic nanoparticles in the broad size distribution that has the sample. On the other hand, in the case of manganite microparticles this absorption was associated with the movement of domain walls of the microparticles. It turns out that size effects determine the power absorption as well as the maximum frequency that a magnetic system can absorbs, as in the case of chapter 1. Therefore, finite size effects, such as the modification of the blocking temperature due to the reduction of the particle size can be detected using microwave transmission lines. This method provides a fast measurement system and the characterization of the magnetic properties of magnetic nanoparticles using the information that provides the ferromagnetic resonance and the ac-susceptibility at zero field. This union among microwave technology and fundamental science will open new applications as new materials for the screen of microwaves in electronic circuits, the construction of coherent bits based on these absorption properties, new hyperthermia treatments, or security tags working at microwave frequencies.

One of our goals is the proof of concept and the proposal of new applications (for example in medicine) based on high frequencies and magnetic nanoparticles (chapter 3). For this reason we have studied a new novel material of a great interest in basic science, medicine and solar cells: gold nanoparticles surface modified by different capping molecules. Pure gold is a diamagnetic material, but decorating the surface with SAM molecules a magnetic behavior is induced. In our case we have characterized three sets of gold nanoparticles having a mean size belong 3 and 6 nm: two sets with a capping molecule that does not bond to surface gold atoms with covalent bonds, and one with a Au-S covalent bond. The magnetic characterization of these three samples showed that the sample having the covalent bond behaved such as a ferromagnetic nanoparticle. In the other two cases this behavior was also observed, but they had a reduced magnetic moment. Consequently, the bond established between surface gold atoms and the capping molecule generates this magnetic behavior. The covalent Au-S bond localize surface conduction charges at the proximities of the bond that combined with the spin-orbit coupling creates a ferromagnetic shell at the surface of the nanoparticle enveloping a diagmanetic core. The size of the nanoparticle is another important feature in the magnetic properties of such systems, because it depending on the size the diamagnetic core predominates over the ferromagnetic shell (for sizes larger than 3 nm). On the other hand, the magnetic signal observed in the other set of

gold nanoparticles should also be related to the interaction among the decorating molecule and the surface of gold atoms.

Finally, it was reviewed, on chapter 4, the terahertz radiation and their emerging technological applications. These part of the electromagnetic spectra (between 0.3 and 3 THz), which is non-invasive, non-ionizaning, has been of interest in a wide range of applications such as spintronics, material science, pharmacy, and medicine. Because during this thesis we have worked with microwave technology, and systems with a large potential in medicine; we focus in the use of terahertz waves in non-invasive, and in medical applications . Furthermore, in this chapter we have described other interesting applications in security, such as product tagging, and inspection of the integrity of layered materials. Those studies were the base for us to generate the application of the characterization of the permeation process of topic drugs into skin. The traditional techniques used to study this problem represent an invasive method (skin stripping) to quantize the amount of drug at different layers of the skin. Nevertheless, our technique is carried out with terahertz radiation in a contactless method. Measuring the flight time of T-rays between the receptor and a layer of excipient onto an artificial membrane or human abdominal skin, it was demonstrated the capability of terahertz technology to fully characterize the permeation process of a substance. This work could be combined with spectroscopy technique at terahertz frequencies to detect the amount of active principle in the formulation or with nanomagnetic systems to improve the resolution of the system.

In conclusion, in this work we show new and interesting phenomena in nanomagnetism, new experimental techniques and characterization of magnetic nanoparticles at microwave frequencies as well as their medical applications such as the non-invasive characterization of the permeation process of a topic drug into skin.

Appendix A

Samples A and B of $CoFe_2O_4$ nanoparticles

In this appendix the results for the samples A and B of chapter 1 are showed. As can be seen the behavior of these samples was similar to the sample depicted in chapter 1.

A.1. Sample A

Sample A consisted in a bimodal size distribution of $CoFe_2O_4$ with mean diameter of 2 nm for small particles and mean diameter of 5 nm for large particles. The magnetic characterization of the sample was the same that the exposed in chapter 1. The peak at low temperature was observed at 8.5 K, and the high temperature peak at 120 K. Besides the difference on the position of the peaks, the other relevant difference was the broadness of the size distribution, being larger in this case. Finally, the larger value of the blocking temperature of this sample respect to the results exposed in chapter 1, made that the isothermal curves resulted in an overlapping of paramangetic and magnetically blocked particles. The results were:

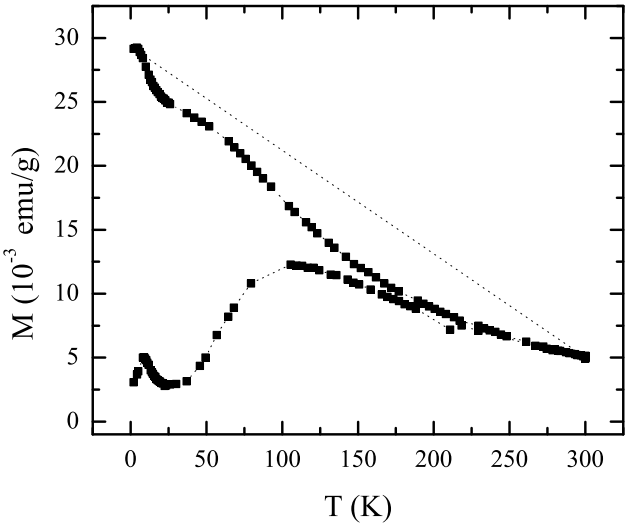

Figure A.1: ZFC-FC for sample A. In the picture two peaks at 8.5 and 120 K are clearly seen.

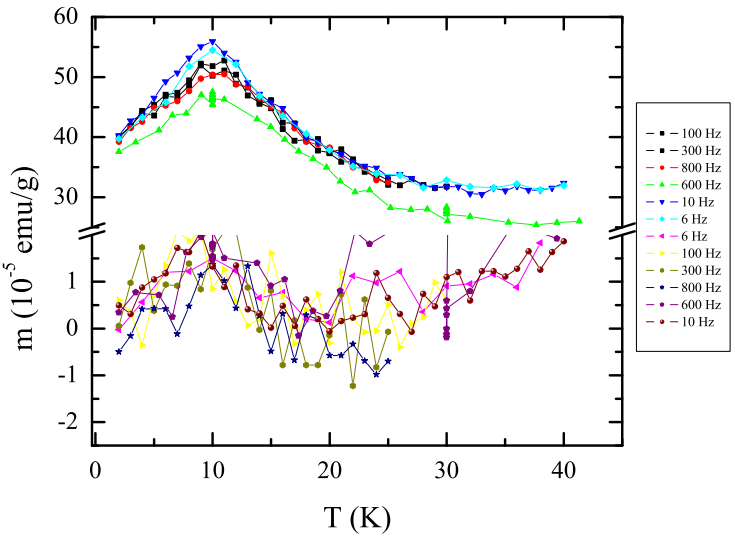

Figure A.2: Measured ac-susceptibilty for sample A. Neither the in-phase nor the out-phase component depend on the frequency of the oscillating field.

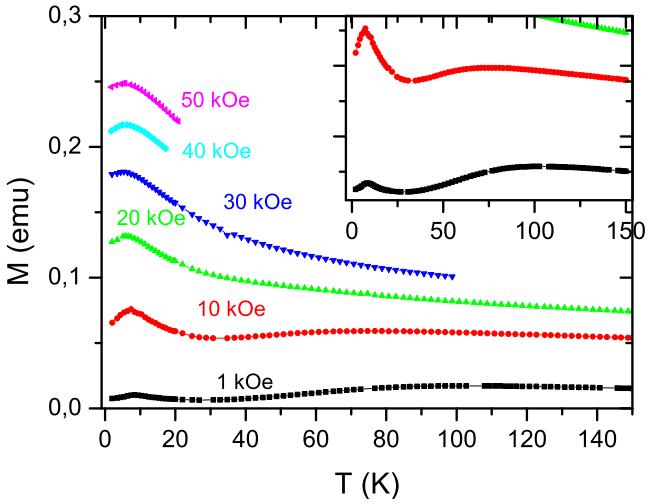

Figure A.3: ZFC at different fields for sample A. As in the case of the sample analyzed in chapter 1, the peak at low temperature did not depend on the field.

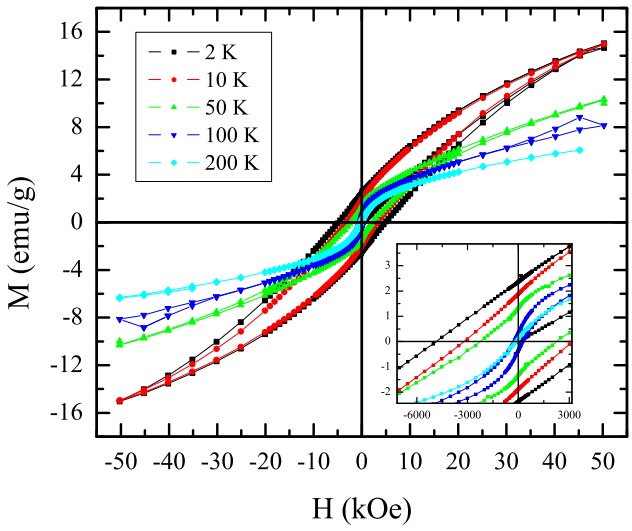

Figure A.4: Isothermal curves for sample A. In this case an overlap between a paramagnetic and a superparamagnetic signal is also see.

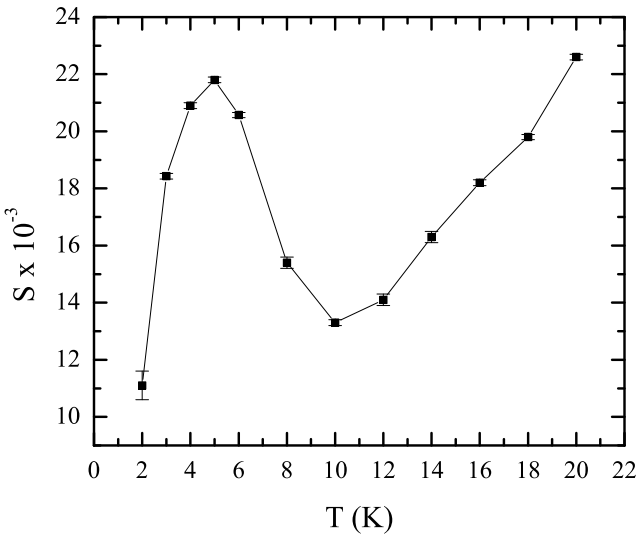

Figure A.5: Magnetic viscosity for sample A extracted from the zero field relaxation curves. In this case the peak associated with small particles is clearly seen.

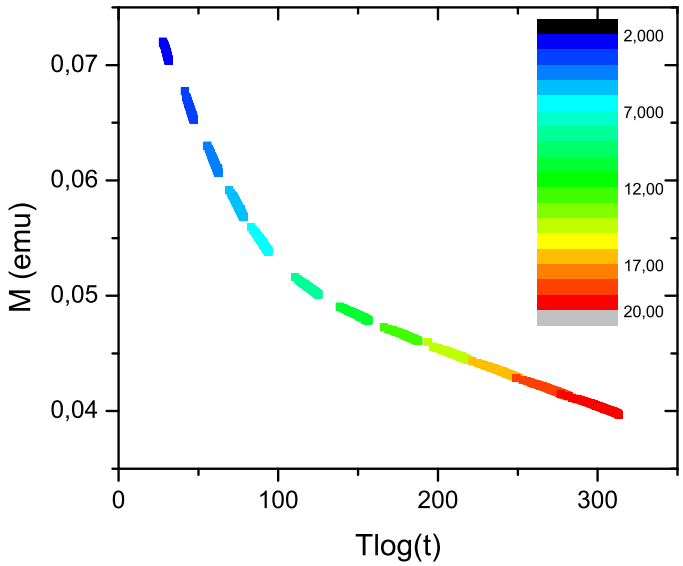

Figure A.6: $T \log(t)$ fit of the relaxation curves at zero field for sample A. The two thermal regimes associated with the two peaks observed in the ZFC-FC curves are clearly seen.

A.2. Sample B

Sample B consisted in a bimodal size distribution of $CoFe_2O_4$ with mean diameter of 2.5 *nm* for small particles and mean diameter of 6.5 *nm* for large particles. The magnetic characterization of the sample was the same that the exposed in chapter 1. The peak at low temperature was observed at 7.5 and the high temperature peak at 150 K. The main difference was the position of the peak at high temperature and its broadness, being smaller in this last case:

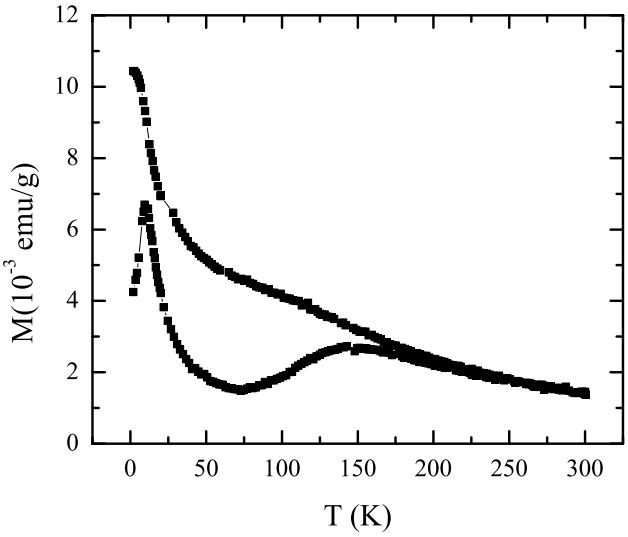

Figure A.7: ZFC-FC magnetization curves for sample B. In this case the peak at low temperature was observed at 7.5 and the peak at high temperature at 150 K.

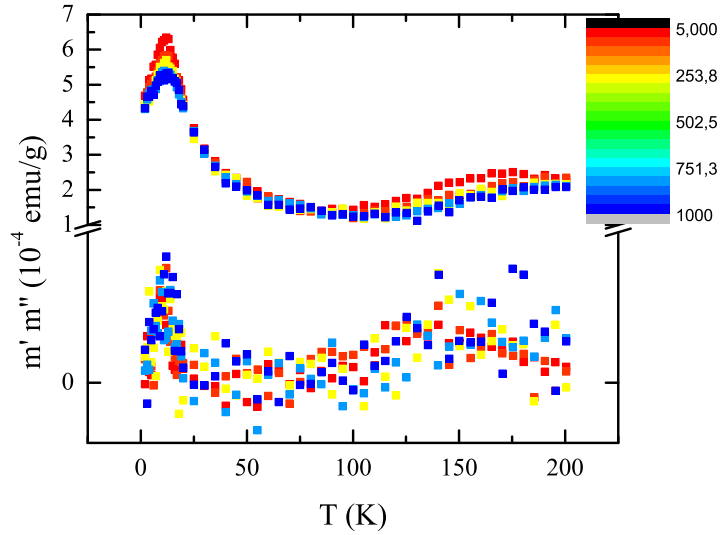

Figure A.8: Ac-susceptibilty for sample B between 1 Hz and 1 kHz. The peak at high temperature depended logarithmically on the frequency of the oscillating field. Nevertheless the peak at low temperature was independent on the ac-frequency.

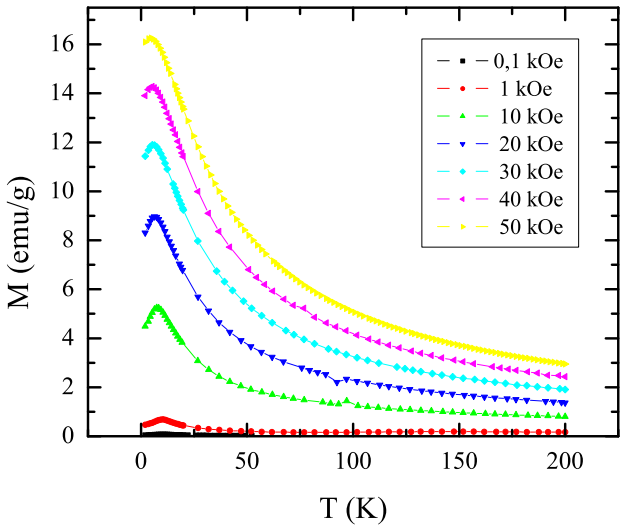

Figure A.9: ZFC magnetization curves of sample B at different fields. Like samples A and B the peak at low temperature did not depend on the applied field.

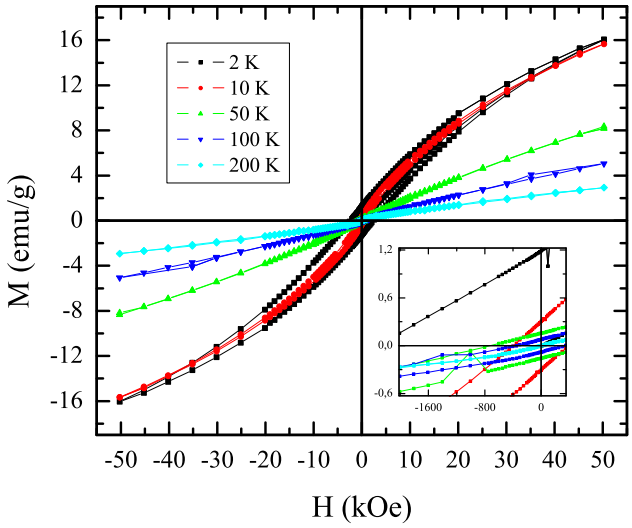

Figure A.10: Isothermal curves for sample B. For temperatures between the transition temperature and the blocking temperature a paramagnetic signal is clearly seen. Furthermore for temperatures higher than the blocking temperature of large particles an overlap between a paramagnetic and a superparamagnetic signal are observed.

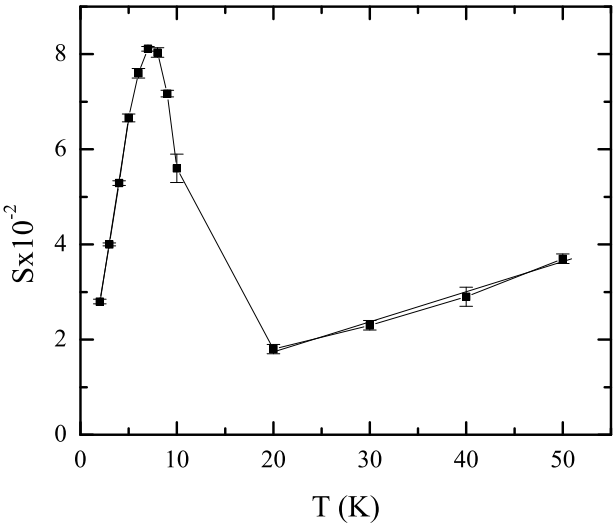

Figure A.11: Magnetic viscosity for sample B extracted from the relaxation experiments at zero field. Another time a peak at low temperature is observed.

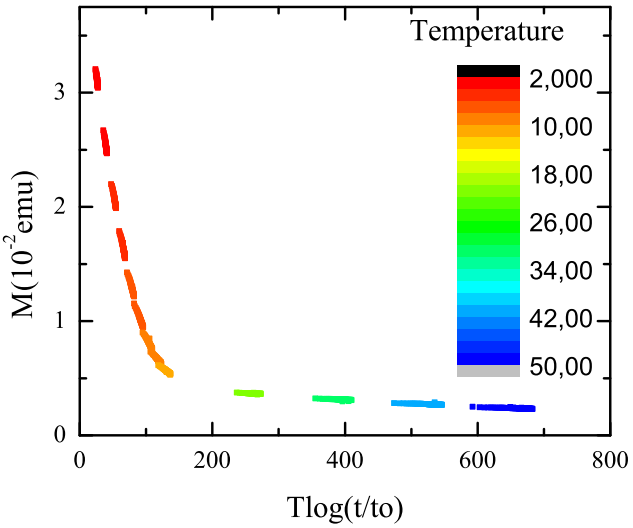

Figure A.12: $T \log(t)$ fit for the relaxation experiments of sample B. The fit was accomplished by an attempt time of 10^{-12} s. Moreover, the two thermal regimes are clearly seen.

Appendix B

Results of active permeation experiments

In this appendix is showed the distance profiles as a function of time for the four excipients assessed in the active permeation experiments. Like in the case of propylene glycol, the results showed a linear profile of the height of the drop. Finally, in different cases a base correction line had to be applied.

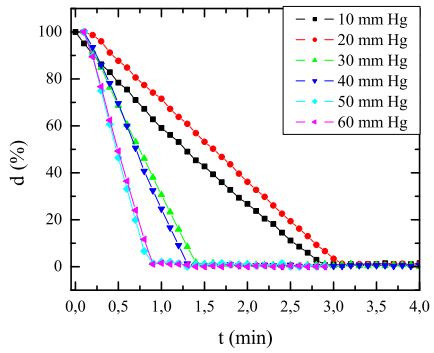

(a) Propylene glycol.

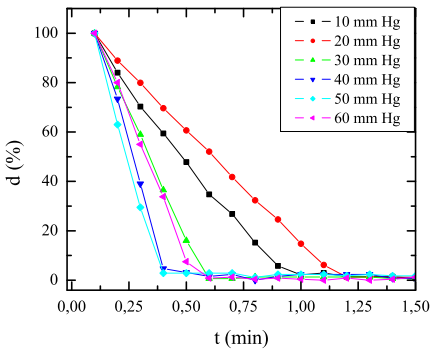

(b) Paraffin oil.

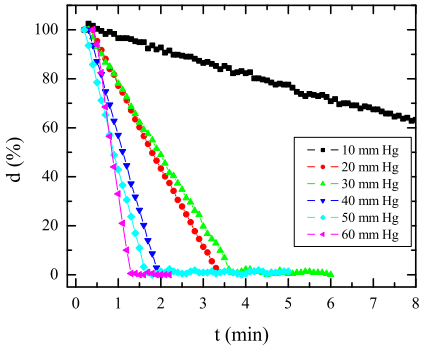

(c) Sweet almond oil.

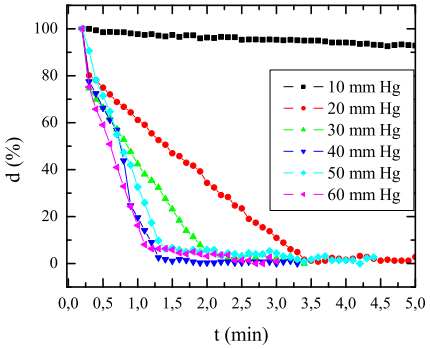

(d) PEG 400.

Figure B.1: Distances profiles for the four assessed excipients on PVDF membrane. In the four cases, the distance profile depended linearly on time.

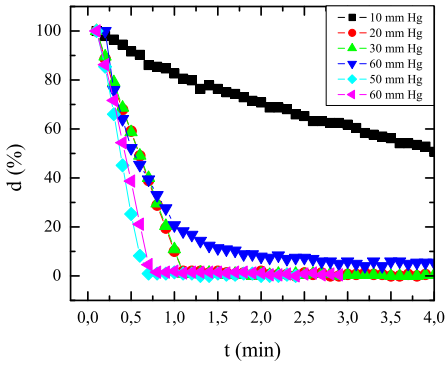

(a) Paraffin oil.

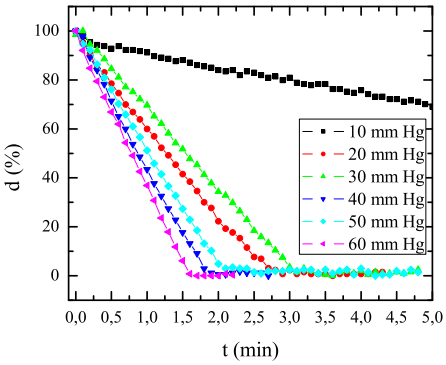

(b) Sweet almond oil.

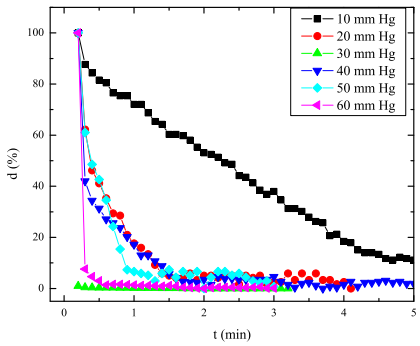

(c) PEG 400.

Figure B.2: Distances profiles for three assessed excipients on nylon membrane (propylene glycol is omitted because it was shown in chapter 4). In the four cases, the distance profile depended linearly on time.

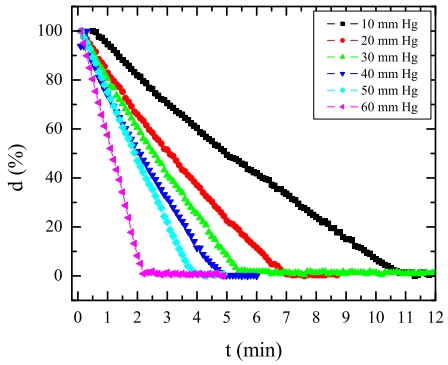

(a) Propylene glycol.

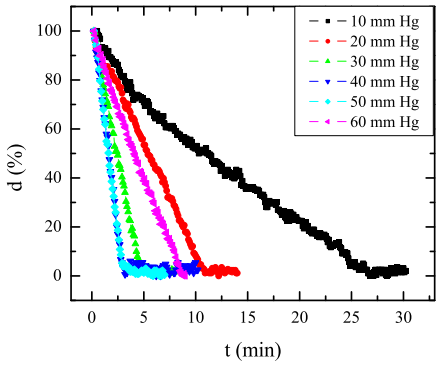

(b) Paraffin oil.

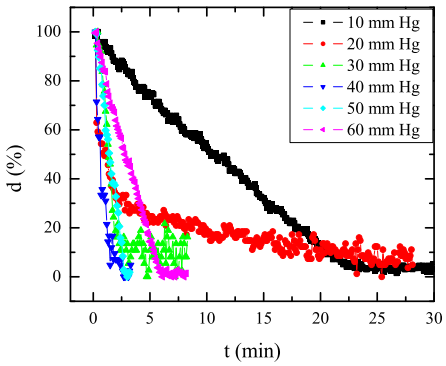

(c) Sweet almond oil.

Figure B.3: Distances profiles for the three assessed excipients in nylon membrane of 0.22 μm of pore radius. In the table it is not shown the results of PEG 400 because it did not flow through that membrane. In the three cases, the distance profile depended linearly on time.

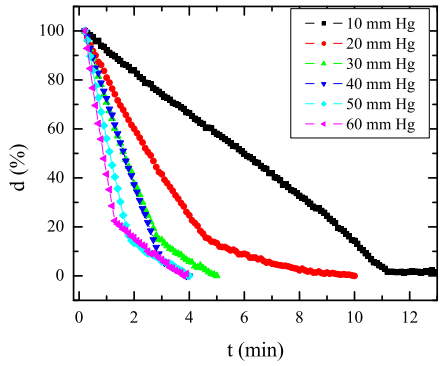

(a) Propylene glycol.

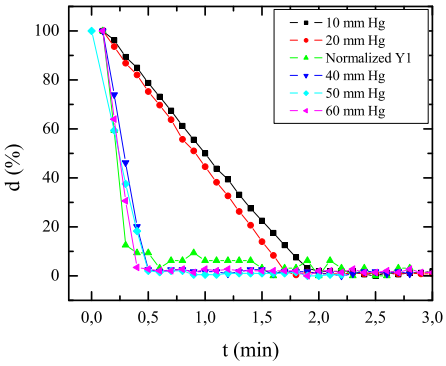

(b) Paraffin oil.

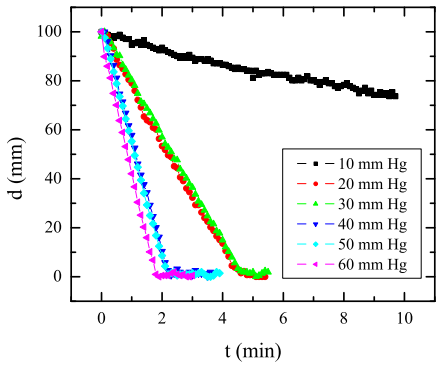

(c) Sweet almond oil.

Figure B.4: Distances profiles for the three assessed excipients on cellulose membrane. PEG 400 was not tested on cellulose membrane due to its chemical incompatibility.

Bibliography

[1] E. de Biasi, C. Ramos, and R. Zysler. "Size and anisotropy determination by ferromagnetic resonance in dispersed magnetic nanoparticle systems". In: *Journal of Magnetism and Magnetic Materials* 262.2 (2003), pp. 235–241. DOI: 10.1016/S0304-8853(02)01496-8.

[2] F. Gazeau, J. Bacri, F. Gendron, R. Perzynski, Y. Raikher, V. Stepanov, and E. Dubois. "Magnetic resonance of ferrite nanoparticles:: evidence of surface effects". In: *Journal of Magnetism and Magnetic Materials* 186.2 (1998), pp. 175–187. DOI: 10.1016/S0304-8853(98)00080-8.

[3] S. Oh, J. Kang, I. Maeng, J. Suh, Y. Huh, S. Haam, and J. Son. "Nanoparticle-enabled terahertz imaging for cancer diagnosis". In: *Opt. Express* 17 (2009), pp. 3469–3475.

[4] S. Oh et al. "Nanoparticle-enabled terahertz imaging for cancer diagnosis". In: *Opt. Express* 19 (2011), pp. 4009–4016.

[5] J. Y. Park, H. J. Choi, G. Nam, K. S. Cho, and J. H. Son. "In Vivo Dual-Modality Terahertz/Magnetic Resonance Imaging Using Superparamagnetic Iron Oxide Nanoparticles as a Dual Contrast Agent". In: *Terahertz Science and Technology, IEEE Transactions on* 2.1 (2011), pp. 93–98. DOI: 10.1109/TTHZ.2011.2177174.

[6] V. B. Bregar. "Nanoparticle-enabled terahertz imaging for cancer diagnosis". In: *Magnetics, IEEE Transactions on* 40.3 (2004), pp. 1679–1684. DOI: 10.1109/TMAG.2004.826622.

[7] M. Babincová, P. Čičmanec, V. Altanerová, Č. Altaner, and P. Babinec. "AC-magnetic field controlled drug release from magnetoliposomes: design of a method for site-specific chemotherapy". In: *Bioelectrochemistry* 55 (2002), pp. 17–19. DOI: 10.1016/S1567-5394(01)00171-2.

[8] B. Gleich and J. Weizenecker. “Tomographic imaging using the nonlinear response of magnetic particles”. In: *Nature* 435 (2005), pp. 1214–1217. DOI: 10.1038/nature03808.

[9] A. Hernando, P. Crespo, and M. A. Garc´. “Origin of Orbital Ferromagnetism and Giant Magnetic Anisotropy at the Nanoscale”. In: *Phys. Rev. Lett.* 96 (5 2006), p. 057206. DOI: 10.1103/PhysRevLett.96.057206.

[10] J. L. Dorman and D. Fiorani. “Proceeding of the interantional Workshop on studies of Magnetic Properties of Fine Particles and Their Revelance to Materials Science”. In: *Eds.* (1991).

[11] J. Tejada, R. F. Ziolo, and X. X. Zhang. “Quantum Tunneling of Magnetization in Nanostructured Materials”. In: *Chemistry of Materials* 8.8 (1996), pp. 1784–1792. DOI: 10.1021/cm9602003. eprint: http://pubs.acs.org/doi/pdf/10.1021/cm9602003.

[12] R. Sappey, E. Vincent, N. Hadacek, F. Chaput, J. P. Boilot, and D. Zins. “Nonmonotonic field dependence of the zero-field cooled magnetization peak in some systems of magnetic nanoparticles”. In: *Phys. Rev. B* 56 (22 1997), pp. 14551–14559. DOI: 10.1103/PhysRevB.56.14551.

[13] E. Chudnosky and J. Tejada. “Macroscopic Quantum tunneling of the Magnetic Moment”. In: *Cambrige studies in Magnetism (No. 4); Cambrige University Press: Cambrige U.K.* (1998).

[14] C. Ross. “PATTERNED MAGNETIC RECORDING MEDIA”. In: *Annual Review of Materials Research* 31.1 (2001), pp. 203–235. DOI: 10.1146/annurev.matsci.31.1.203. eprint: http://www.annualreviews.org/doi/pdf/10.1146/annurev.matsci.31.1.203.

[15] T. Hyeon. “Chemical synthesis of magnetic nanoparticles”. In: *Chem. Commun.* (8 2003), pp. 927–934. DOI: 10.1039/B207789B.

[16] Q. A. Pankhurst, J. Connolly, S. K. Jones, and J. Dobson. “Applications of magnetic nanoparticles in biomedicine”. In: *Journal of Physics D: Applied Physics* 36.13 (2003), R167.

[17] R. E. Rosensweig. “Magnetic Fluids”. In: *Annual Review of Fluid Mechanics* 19.1 (1987), pp. 437–461. DOI: 10.1146/annurev.fl.19.010187.002253. eprint: http://www.annualreviews.org/doi/pdf/10.1146/annurev.fl.19.010187.002253.

[18] A.-H. Lu, E. L. Salabas, and F. Schüth. “Magnetic Nanoparticles: Synthesis, Protection, Functionalization, and Application”. In: *Angewandte Chemie*

International Edition 46.8 (2007), pp. 1222–1244. DOI: 10.1002/anie.200602866.

[19] R. H. Kodama, A. E. Berkowitz, E. J. McNiff Jr., and S. Foner. "Surface Spin Disorder in $NiFe_2O_4$ Nanoparticles". In: *Phys. Rev. Lett.* 77 (2 1996), pp. 394–397. DOI: 10.1103/PhysRevLett.77.394.

[20] R. Kodama. "Magnetic nanoparticles". In: *Journal of Magnetism and Magnetic Materials* 200.1–3 (1999), pp. 359–372. DOI: 10.1016/S0304-8853(99)00347-9.

[21] J. Tejada, R. D. Zysler, E. Molins, and E. M. Chudnovsky. "Evidence for Quantization of Mechanical Rotation of Magnetic Nanoparticles". In: *Phys. Rev. Lett.* 104 (2 2010), p. 027202. DOI: 10.1103/PhysRevLett.104.027202.

[22] X. Batlle and A. Labarta. "Finite-size effects in fine particles: magnetic and transport properties". In: *Journal of Physics D: Applied Physics* 35.6 (2002), R15.

[23] Q. Dai, M. Lam, S. Swanson, R.-H. R. Yu, D. J. Milliron, T. Topuria, P.-O. Jubert, and A. Nelson. "Monodisperse Cobalt Ferrite Nanomagnets with Uniform Silica Coatings". In: *Langmuir* 26.22 (2010), pp. 17546–17551. DOI: 10.1021/la103042q. eprint: http://pubs.acs.org/doi/pdf/10.1021/la103042q.

[24] C. N. Chinnasamy, B. Jeyadevan, K. Shinoda, K. Tohji, D. J. Djayaprawira, M. Takahashi, R. J. Joseyphus, and A. Narayanasamy. "Unusually high coercivity and critical single-domain size of nearly monodispersed CoFe2O4 nanoparticles". In: *Applied Physics Letters* 83.14 (2003), pp. 2862–2864.

[25] E. Chudnovsky and J. Tejada. "Lectures on Magnetism". In: *Rinto Press: Princeton* (2006).

[26] R. Sappey, E. Vincent, N. Hadacek, F. Chaput, J. P. Boilot, and D. Zins. "Nonmonotonic field dependence of the zero-field cooled magnetization peak in some systems of magnetic nanoparticles". In: *Phys. Rev. B* 56 (22 1997), pp. 14551–14559. DOI: 10.1103/PhysRevB.56.14551.

[27] S. Sun and H. Zeng. "Size-Controlled Synthesis of Magnetite Nanoparticles". In: *Journal of the American Chemical Society* 124.28 (2002), pp. 8204–8205. DOI: 10.1021/ja026501x. eprint: http://pubs.acs.org/doi/pdf/10.1021/ja026501x.

[28] G. Baldi, D. Bonacchi, M. C. Franchini, D. Gentili, G. Lorenzi, A. Ricci, and C. Ravagli. "Synthesis and Coating of Cobalt Ferrite Nanoparticles: A First Step toward the Obtainment of New Magnetic Nanocarriers". In: *Langmuir* 23.7 (2007). PMID: 17335257, pp. 4026–4028. DOI: 10.1021/la063255k. eprint: http://pubs.acs.org/doi/pdf/10.1021/la063255k.

[29] E. Skoropata, R. D. Desautels, B. W. Southern, and J. van Lierop. "Comment on "Colossal Reduction in Curie Temperature Due to Finite-Size Effects in CoFe2O4 Nanoparticles"". In: *Chemistry of Materials* 25.9 (2013), pp. 1998–2000. DOI: 10.1021/cm303893h. eprint: http://pubs.acs.org/doi/pdf/10.1021/cm303893h.

[30] G. F. Goya, T. S. Berquó, F. C. Fonseca, and M. P. Morales. "Static and dynamic magnetic properties of spherical magnetite nanoparticles". In: *Journal of Applied Physics* 94.5 (2003), pp. 3520–3528.

[31] D. Peddis, F. Orrù, A. Ardu, C. Cannas, A. Musinu, and G. Piccaluga. "Interparticle Interactions and Magnetic Anisotropy in Cobalt Ferrite Nanoparticles: Influence of Molecular Coating". In: *Chemistry of Materials* 24.6 (2012), pp. 1062–1071. DOI: 10.1021/cm203280y. eprint: http://pubs.acs.org/doi/pdf/10.1021/cm203280y.

[32] N. Moumen, P. Bonville, and M. P. Pileni. "Control of the Size of Cobalt Ferrite Magnetic Fluids: Mössbauer Spectroscopy". In: *The Journal of Physical Chemistry* 100.34 (1996), pp. 14410–14416. DOI: 10.1021/jp953324w. eprint: http://pubs.acs.org/doi/pdf/10.1021/jp953324w.

[33] J. Barker and E. Schmamiloglu. *High-power microwave sources technologies*. IEE, 2001.

[34] S. Caorsi, A. Massa, M. Pastorino, and A. Rosani. "Microwave medical imaging: potentialities and limitations of a stochastic optimization technique". In: *Microwave Theory and Techniques, IEEE Transactions on* 52.8 (2004), pp. 1909–1916. DOI: 10.1109/TMTT.2004.832016.

[35] C.-C. Chao, J.-M. Yang, and W.-Y. Jen. "Determining technology trends and forecasts of {RFID} by a historical review and bibliometric analysis from 1991 to 2005". In: *Technovation* 27.5 (2007), pp. 268–279. DOI: http://dx.doi.org/10.1016/j.technovation.2006.09.003.

[36] M. Pardavi-Horvath. "Microwave applications of soft ferrites". In: *Journal of Magnetism and Magnetic Materials* 215–216 (2000), pp. 171–183. DOI: http://dx.doi.org/10.1016/S0304-8853(00)00106-2.

[37] V. K. Sharma and F. Waldner. “Superparamagnetic and ferrimagnetic resonance of ultrafine Fe3O4 particles in ferrofluids”. In: *Journal of Applied Physics* 48.10 (1977), pp. 4298–4302.

[38] F. Mazaleyrat and L. Varga. “Ferromagnetic nanocomposites”. In: *Journal of Magnetism and Magnetic Materials* 215–216 (2000), pp. 253–259. DOI: http://dx.doi.org/10.1016/S0304-8853(00)00128-1.

[39] C. Chappert, A. Fert, and F. Van Dau. “The emergence of spin electronics in data storage”. In: *Nature Materials* 6.11 (2007), pp. 813–823.

[40] T. Neuberger, B. Schöpf, H. Hofmann, M. Hofmann, and B. von Rechenberg. “Superparamagnetic nanoparticles for biomedical applications: Possibilities and limitations of a new drug delivery system”. In: *Journal of Magnetism and Magnetic Materials* 293.1 (2005). ¡ce:title¿Proceedings of the Fifth International Conference on Scientific and Clinical Apllications of Magnetic Carriers¡/ce:title¿, pp. 483–496. DOI: http://dx.doi.org/10.1016/j.jmmm.2005.01.064.

[41] A. Ito, M. Shinkai, H. Honda, and T. Kobayashi. “Medical application of functionalized magnetic nanoparticles”. In: *Journal of Bioscience and Bioengineering* 100.1 (2005), pp. 1–11. DOI: http://dx.doi.org/10.1263/jbb.100.1.

[42] R. Hergt, R. Hiergeist, I. Hilger, W. Kaiser, Y. Lapatnikov, S. Margel, and U. Richter. “Maghemite nanoparticles with very high AC-losses for application in RF-magnetic hyperthermia”. In: *Journal of Magnetism and Magnetic Materials* 270.3 (2004), pp. 345–357. DOI: http://dx.doi.org/10.1016/j.jmmm.2003.09.001.

[43] E. de Biasi, C. Ramos, and R. Zysler. “Size and anisotropy determination by ferromagnetic resonance in dispersed magnetic nanoparticle systems”. In: *Journal of Magnetism and Magnetic Materials* 262.2 (2003), pp. 235–241. DOI: http://dx.doi.org/10.1016/S0304-8853(02)01496-8.

[44] S. Eustis and M. A. el-Sayed. “Why gold nanoparticles are more precious than pretty gold: noble metal surface plasmon resonance and its enhancement of the radiative and nonradiative properties of nanocrystals of different shapes”. In: *Chem Soc Rev* 35.3 (2006), pp. 209–17. DOI: 10.1039/b514191e.

[45] C. J. Zhong and M. M. Maye. “Core–Shell Assembled Nanoparticles as Catalysts”. In: *Advanced Materials* 13.19 (2001), pp. 1507–1511. DOI: 10.1002/1521-4095(200110)13:19.

[46] P. K. Jain, K. S. Lee, I. H. El-Sayed, and M. A. El-Sayed. "Calculated Absorption and Scattering Properties of Gold Nanoparticles of Different Size, Shape, and Composition: Applications in Biological Imaging and Biomedicine". In: *The Journal of Physical Chemistry B* 110.14 (2006). PMID: 16599493, pp. 7238–7248. DOI: 10.1021/jp057170o. eprint: http://pubs.acs.org/doi/pdf/10.1021/jp057170o.

[47] J. Kuhl, H. Giessen, and S. Linden. "Controlling the Interaction between Light and Gold Nanoparticles: Selective Suppression of Extinction". In: *Physical Review Letters* 86 (2001), pp. 4688–4691.

[48] J. W. M. Chon, C. Bullen, P. Zijlstra, and M. Gu. "Spectral encoding on Gold Nanorods Doped in a Silica Sol–Gel Matrix and Its Application to High-Density Optical Data Storage". In: *Advanced Functional Materials* 17.6 (2007), pp. 875–880. DOI: 10.1002/adfm.200600565.

[49] S. I. Khondaker, K. Luo, and Z. Yao. "The fabrication of single-electron transistors using dielectrophoretic trapping of individual gold nanoparticles". In: *Nanotechnology* 21.9 (2010), p. 095204.

[50] U. C. Coskun et al. "Single-electron transistors made by chemical patterning of silicon dioxide substrates and selective deposition of gold nanoparticles". In: *Applied Physics Letters* 93.12 (2008), pages. DOI: 10.1063/1.2981705.

[51] J.C. Ramos, A. Ledezma Ivana Moggio Eduardo Arias R.A. Vazquez Carlos A. Martínez J.R. Torres Ronald F. Ziolo Perla E. García S. Sepulveda Miguel José-Yacamán A. Olivas. "Composites of Bromobenzenethiol Functionalized Gold Nanoparticles and the Fluorescent Poly(Phenylene Ethynylene) pPET3OC12-sqS for Optical Biosensors". In: *Journal of Nano Research* 5 (2009), pp. 36–37.

[52] L. Moriggi, C. Cannizzo, E. Dumas, C. R. Mayer, A. Ulianov, and L. Helm. "Gold Nanoparticles Functionalized with Gadolinium Chelates as High-Relaxivity MRI Contrast Agents". In: *Journal of the American Chemical Society* 131.31 (2009). PMID: 19722661, pp. 10828–10829. DOI: 10.1021/ja904094t. eprint: http://pubs.acs.org/doi/pdf/10.1021/ja904094t.

[53] P. Ghosh, G. Han, M. De, C. K. Kim, and V. M. Rotello. "Gold nanoparticles in delivery applications". In: *Advanced Drug Delivery Reviews* 60.11 (2008). ¡ce:title¿Inorganic Nanoparticles in Drug Delivery¡/ce:title¿, pp. 1307–1315. DOI: 10.1016/j.addr.2008.03.016.

[54] H. Huang and X. Yang. "Synthesis of Chitosan-Stabilized Gold Nanoparticles in the Absence/Presence of Tripolyphosphate". In: *Biomacromolecules* 5.6 (2004). PMID: 15530050, pp. 2340–2346. DOI: 10.1021/bm0497116. eprint: http://pubs.acs.org/doi/pdf/10.1021/bm0497116.

[55] M. Hasan, D. Bethell, and M. Brust. "The Fate of Sulfur-Bound Hydrogen on Formation of Self-Assembled Thiol Monolayers on Gold: 1H NMR Spectroscopic Evidence from Solutions of Gold Clusters". In: *Journal of the American Chemical Society* 124.7 (2002). PMID: 11841257, pp. 1132–1133. DOI: 10.1021/ja0120577. eprint: http://pubs.acs.org/doi/pdf/10.1021/ja0120577.

[56] G. Leitus, R. Naaman, S. Reich, Z. Vager, and J. Carmelli. In: *Journal of Chemistry Physics* 118 (2003), p. 10372.

[57] Y. Yamamoto et al. "Direct Observation of Ferromagnetic Spin Polarization in Gold Nanoparticles". In: *Phys. Rev. Lett.* 93 (11 2004), p. 116801. DOI: 10.1103/PhysRevLett.93.116801.

[58] H. Hori, Y. Yamamoto, T. Iwamoto, T. Miura, T. Teranishi, and M. Miyake. "Diameter dependence of ferromagnetic spin moment in Au nanocrystals". In: *Phys. Rev. B* 69 (17 2004), p. 174411. DOI: 10.1103/PhysRevB.69.174411.

[59] P. Zhang and T. K. Sham. "X-Ray Studies of the Structure and Electronic Behavior of Alkanethiolate-Capped Gold Nanoparticles: The Interplay of Size and Surface Effects". In: *Phys. Rev. Lett.* 90 (24 2003), p. 245502. DOI: 10.1103/PhysRevLett.90.245502.

[60] A. P. Alivisatos. "Semiconductor Clusters, Nanocrystals, and Quantum Dots". In: *Science* 271.5251 (1996), pp. 933–937. DOI: 10.1126/science.271.5251.933. eprint: http://www.sciencemag.org/content/271/5251/933.full.pdf.

[61] R. J. Magyar, V. Mujica, M. Marquez, and C. Gonzalez. "Density-functional study of magnetism in bare Au nanoclusters: Evidence of permanent size-dependent spin polarization without geometry relaxation". In: *Phys. Rev. B* 75 (14 2007), p. 144421. DOI: 10.1103/PhysRevB.75.144421.

[62] N. Ashcroft and N. D. Mermin. *Solid state physics*. Saunders College, 1976.

[63] J. Tejada and E. Chudnovsky. *Lectures on Magnetism*. Cambrige.

[64] P. Crespo, E. Guerrero, M. Muoz-Marquez, A. Hernando, and A. Fernandez. "Influence of the Capping Molecule on the Magnetic Behavior of Thiol-

Capped Gold Nanoparticles". In: *Magnetics, IEEE Transactions on* 44.11 (2008), pp. 2768–2771. DOI: 10.1109/TMAG.2008.2001990.

[65] J. Zhou, J. Ralston, R. Sedev, and D. A. Beattie. "Functionalized gold nanoparticles: Synthesis, structure and colloid stability". In: *Journal of Colloid and Interface Science* 331.2 (2009), pp. 251–262. DOI: 10.1016/j.jcis.2008.12.002.

[66] R. Popovtzer, A. Agrawal, N. A. Kotov, A. Popovtzer, J. Balter, T. E. Carey, and R. Kopelman. "Targeted Gold Nanoparticles Enable Molecular CT Imaging of Cancer". In: *Nano Letters* 8.12 (2008). PMID: 18983199, pp. 4593–4596. DOI: 10.1021/nl8029114. eprint: http://pubs.acs.org/doi/pdf/10.1021/nl8029114.

[67] R. Popovtzer, A. Agrawal, N. A. Kotov, A. Popovtzer, J. Balter, T. E. Carey, and R. Kopelman. "Targeted Gold Nanoparticles Enable Molecular CT Imaging of Cancer". In: *Nano Letters* 8.12 (2008). PMID: 18983199, pp. 4593–4596. DOI: 10.1021/nl8029114. eprint: http://pubs.acs.org/doi/pdf/10.1021/nl8029114.

[68] P. Crespo et al. "Permanent Magnetism, Magnetic Anisotropy, and Hysteresis of Thiol-Capped Gold Nanoparticles". In: *Phys. Rev. Lett.* 93 (8 2004), p. 087204. DOI: 10.1103/PhysRevLett.93.087204.

[69] A. Hernando, P. Crespo, and M. A. García. "Origin of Orbital Ferromagnetism and Giant Magnetic Anisotropy at the Nanoscale". In: *Phys. Rev. Lett.* 96 (5 2006), p. 057206. DOI: 10.1103/PhysRevLett.96.057206.

[70] P. Crespo, M. A. García, E. Fernández Pinel, M. Multigner, D. Alcántara, J. M. de la Fuente, S. Penadés, and A. Hernando. "Fe Impurities Weaken the Ferromagnetic Behavior in Au Nanoparticles". In: *Phys. Rev. Lett.* 97 (17 2006), p. 177203. DOI: 10.1103/PhysRevLett.97.177203.

[71] F. Michael, C. Gonzalez, V. Mujica, M. Marquez, and M. A. Ratner. "Size dependence of ferromagnetism in gold nanoparticles: Mean field results". In: *Phys. Rev. B* 76 (22 2007), p. 224409. DOI: 10.1103/PhysRevB.76.224409.

[72] T. Chady, R. Sikora, G. Psuj, M. Enokizono, and T. Todaka. "Fusion of electromagnetic inspection methods for evaluation of stress-loaded steel samples". In: *Magnetics, IEEE Transactions on* 41.10 (2005), pp. 3721–3723. DOI: 10.1109/TMAG.2005.854918.

[73] M. Benedetti, M. Donelli, A. Martini, M. Pastorino, A. Rosani, and A. Massa. "An Innovative Microwave-Imaging Technique for Nondestructive Evaluation: Applications to Civil Structures Monitoring and Biological Bod-

ies Inspection". In: *Instrumentation and Measurement, IEEE Transactions on* 55.6 (2006), pp. 1878–1884. DOI: 10.1109/TIM.2006.884287.

[74] Y. Lu, G. L. Liu, J. Kim, Y. X. Mejia, and L. P. Lee. "Nanophotonic Crescent Moon Structures with Sharp Edge for Ultrasensitive Biomolecular Detection by Local Electromagnetic Field Enhancement Effect". In: *Nano Letters* 5.1 (2005), pp. 119–124. DOI: 10.1021/nl048232. eprint: http://pubs.acs.org/doi/pdf/10.1021/nl048232\%2B.

[75] S.-A. Zhou and A. Brahme. "Development of phase-contrast X-ray imaging techniques and potential medical applications". In: *Physica Medica* 24.3 (2008), pp. 129–148. DOI: 10.1016/j.ejmp.2008.05.006.

[76] J. Beutel, H. L. Kundel, and R. L. V. Metter, eds. *Handbook of Medical Imaging, Volume 1. Physics and Psychophysics*. Vol. 1. 2000.

[77] D. P. R. Koningsberger. *X-ray absorption: Principles, applications, techniques of EXAFS, SEXAFS and XANES*. 1987.

[78] Y.-S. Lee. *Principles of Terahertz Science and Technology Principles of Terahertz Science and Technology Principles of Terahertz Science and Technology Principles of Terahertz Science and Technology*. Springer Publishing Company, 2008.

[79] P. H. Siegel. "Terahertz Technology". In: *IEEE TRANSACTIONS ON MICROWAVE THEORY AND TECHNIQUES* 50.3 (2002), pp. 910–928.

[80] B. Ferguson and X.-C. Zhang. "Materials for terahertz science and technology". In: *Nat Mater* 1.1 (2002), pp. 26–33.

[81] J. Lougran, M. Gradziel, W. Lanigan, T. Ward, J. Murphy, C.O'Sullivan, and K. Humphereys. "Medical applications of Terahertz Imaging: a Review of Current technology and Potential Applications in Biomedical Engineering". In: *Proceeding of the 26th Annual International Conference of the IEEE EMBS* (2004).

[82] J. A. Zeitler, P. F. Taday, D. A. Newnham, M. Pepper, K. C. Gordon, and T. Rades. "Terahertz pulsed spectroscopy and imaging in the pharmaceutical setting–a review". In: *J Pharm Pharmacol* 59.2 (2007), pp. 209–23. DOI: 10.1211/jpp.59.2.0008.

[83] A. J. FITZGERALD, E. PICKWELL, R. J. PYE, P. F. TADAY, N. FLANAGAN, T. HA, and V. P. WALLACE. "Terahertz Pulsed Spectroscopy of Human Basal Cell Carcinoma". In: *Applied Spectroscopy* 60.10 (2006), pp. 1127–1133.

[84] D. M. Mittleman, M. C. Nuss, and V. L. Colvin. "Terahertz spectroscopy of water in inverse micelles". In: *Chemical Physics Letters* 275.3–4 (1997), pp. 332–338. DOI: 10.1016/S0009-2614(97)00760-4.

[85] K. L. Nguyen, T. Friscic, G. M. Day, L. F. Gladden, and W. Jones. "Terahertz time-domain spectroscopy and the quantitative monitoring of mechanochemical cocrystal formation". In: *Nat Mater* 6.3 (2007), pp. 206–209.

[86] J. Kono. "Spintronics: Coherent terahertz control". In: *Nat Photon* 5.1 (2011), pp. 5–6.

[87] K. J. Chau, M. Johnson, and A. Y. Elezzabi. "Electron-Spin-Dependent Terahertz Light Transport in Spintronic-Plasmonic Media". In: *Phys. Rev. Lett.* 98 (13 2007), p. 133901. DOI: 10.1103/PhysRevLett.98.133901.

[88] J. Hadgraft and W. J. Pugh. "The Selection and Design of Topical and Transdermal Agents: A Review". In: *J Invest Derm Symp P* 3.2 (1998), pp. 131–135.

[89] K. Moser, K. Kriwet, A. Naik, Y. N. Kalia, and R. H. Guy. "Passive skin penetration enhancement and its quantification in vitro". In: *European Journal of Pharmaceutics and Biopharmaceutics* 52.2 (2001), pp. 103–112. DOI: 10.1016/S0939-6411(01)00166-7.

[90] R. B. Walker and E. W. Smith. "The role of percutaneous penetration enhancers". In: *Advanced Drug Delivery Reviews* 18.3 (1996). ¡ce:title¿The Skin as a Site for Drug Delivery: the Liposome Approach and its Alternatives¡/ce:title¿, pp. 295–301. DOI: 10.1016/0169-409X(95)00078-L.

[91] G. Ottaviani, S. Martel, and P.-A. Carrupt. "Parallel Artificial Membrane Permeability Assay: A New Membrane for the Fast Prediction of Passive Human Skin Permeability". In: *Journal of Medicinal Chemistry* 49.13 (2006). PMID: 16789751, pp. 3948–3954. DOI: 10.1021/jm060230. eprint: http://pubs.acs.org/doi/pdf/10.1021/jm060230\%2B.

[92] F. Barbato, B. Cappello, A. Miro, M. L. Rotonda, and F. Quaglia. "Chromatographic indexes on immobilized artificial membranes for the prediction of transdermal transport of drugs". In: *Il Farmaco* 53.10–11 (1998), pp. 655–661. DOI: 10.1016/S0014-827X(98)00082-2.

[93] A. Naik, Y. N. Kalia, and R. H. Guy. "Transdermal drug delivery: overcoming the skin's barrier function". In: *Pharmaceutical Science & Technology Today* 3.9 (2000), pp. 318–326. DOI: 10.1016/S1461-5347(00)00295-9.

[94] B. Barry. “Drug delivery routes in skin: a novel approach”. In: *Advanced Drug Delivery Reviews* 54, Supplement (2002). ¡ce:title¿Human skin: the Medium of Touch¡/ce:title¿, S31–S40. DOI: 10.1016/S0169-409X(02)00113-8.

[95] D. R. Friend. “In vitro skin permeation techniques”. In: *Journal of Controlled Release* 18.3 (1992), pp. 235–248. DOI: 10.1016/0168-3659(92)90169-R.

[96] S. G. Kazarian and K. L. A. Chan. “Applications of ATR-FTIR spectroscopic imaging to biomedical samples”. In: *Biochim Biophys Acta* 1758.7 (2006), pp. 858–67. DOI: 10.1016/j.bbamem.2006.02.011.

[97] E. Touitou, V. M. Meidan, and E. Horwitz. “Methods for quantitative determination of drug localized in the skin”. In: *Journal of Controlled Release* 56.1–3 (1998), pp. 7–21. DOI: 10.1016/S0168-3659(98)00060-1.

[98] C. Herkenne, I. Alberti, A. Naik, Y. Kalia, F.-X. Mathy, V. Préat, and R. Guy. “In Vivo Methods for the Assessment of Topical Drug Bioavailability”. In: *Pharmaceutical Research* 25.1 (2008), pp. 87–103.

[99] M. Walther, P. Plochocka, B. Fischer, H. Helm, and P. U. Jepsen. “Collective vibrational modes in biological molecules investigated by terahertz time-domain spectroscopy”. In: *Biopolymers* 67.4-5 (2002), pp. 310–313. DOI: 10.1002/bip.10106.

[100] E. Ozbay. “Plasmonics: Merging Photonics and Electronics at Nanoscale Dimensions”. In: *Science* 311.5758 (2006), pp. 189–193. DOI: 10.1126/science.1114849. eprint: http://www.sciencemag.org/content/311/5758/189.full.pdf.

[101] E. Özbay, J. Bostak, D. M. Bloom, E. Michel, G. Tuttle, R. Biswas, and K. M. Ho. “Terahertz spectroscopy of three-dimensional photonic bandgapcrystals”. In: *Opt. Lett.* 19.15 (1994), pp. 1155–1157. DOI: 10.1364/OL.19.001155.

[102] M. Tonouchi. “Cutting-edge terahertz technology”. In: *Nat Photon* 1.2 (2007), pp. 97–105.

[103] J. M. Chamberlain. “Where optics meets electronics: recent progress in decreasing the terahertz gap”. In: *Philosophical Transactions of the Royal Society of London. Series A: Mathematical, Physical and Engineering Sciences* 362.1815 (2004), pp. 199–213. DOI: 10.1098/rsta.2003.1312. eprint: http://rsta.royalsocietypublishing.org/content/362/1815/199.full.pdf+html.

[104] M. Beck, D. Hofstetter, T. Aellen, J. Faist, U. Oesterle, M. Ilegems, E. Gini, and H. Melchior. "Continuous Wave Operation of a Mid-Infrared Semiconductor Laser at Room Temperature". In: *Science* 295.5553 (2002), pp. 301–305. DOI: 10.1126/science.1066408. eprint: http://www.sciencemag.org/content/295/5553/301.full.pdf.

[105] C. Sirtori. "Applied physics: Bridge for the terahertz gap". In: *Nature* 417.6885 (9, 2002), pp. 132–133.

[106] N. Laman, T. Tongue, and A. Redo-Sanchez. *The Terahertz Wave Book: Tecnical Overview*. Zomega Terahertz Corporation, 2012.

[107] X. Xie, J. Dai, and X.-C. Zhang. "Coherent Control of THz Wave Generation in Ambient Air". In: *Phys. Rev. Lett.* 96 (7 2006), p. 075005. DOI: 10.1103/PhysRevLett.96.075005.

[108] A. J. Kreisler and A. Gaugue. "Recent progress in high-temperature superconductor bolometric detectors: from the mid-infrared to the far-infrared (THz) range". In: *Superconductor Science and Technology* 13.8 (2000), p. 1235.

[109] Q. Wu and X. Zhang. "Freespace electrooptic sampling of terahertz beams". In: *Applied Physics Letters* 67.24 (1995), pp. 3523–3525.

[110] P. U. Jepsen, R. H. Jacobsen, and S. R. Keiding. "Generation and detection of terahertz pulses from biased semiconductor antennas". In: *J. Opt. Soc. Am. B* 13.11 (1996), pp. 2424–2436. DOI: 10.1364/JOSAB.13.002424.

[111] A. G. Davies, A. D. Burnett, W. Fan, E. H. Linfield, and J. E. Cunningham. "Terahertz spectroscopy of explosives and drugs". In: *Materials Today* 11.3 (2008), pp. 18–26. DOI: 10.1016/S1369-7021(08)70016-6.

[112] C. Seco-Martorell, V. López-Dom´nguez, G. Arauz-Garofalo, A. Redo-Sanchez, J. Palacios, and J. Tejada. "Goya’s artwork imaging with Terahertz waves". In: *Opt. Express* 21.15 (2013), pp. 17800–17805. DOI: 10.1364/OE.21.017800.

[113] V. W. E. Pickwell. "Biomedical applications of terahertz technology". In: *Journal of physics D: Applied Physics* 39.R301 (2006).

[114] H.-B. Liu, H. Zhong, N. Karpowicz, Y. Chen, and X.-C. Zhang. "Terahertz Spectroscopy and Imaging for Defense and Security Applications". In: *Proceedings of the IEEE* 95.8 (2007), pp. 1514–1527. DOI: 10.1109/JPROC.2007.898903.

[115] K. Fukunaga, Y. Ogawa, S. Hayashi, and I. Hosako. "Terahertz spectroscopy for art conservation". In: *IEICE Electronics Express* 4.8 (2007), pp. 258–263.

[116] A. Juels. "RFID Security and Privacy: A Research Survey". In: *IEEE Journal on Selected Areas in Comunications* 24.2 (2006), pp. 381–392.

[117] V. Pavel, S. F. Nikitin, K. V. Lam, and R. Seshagiri. "Antenna Design for UHF RFID Tags: A Review and a Practical Application". In: *IEEE TRANSACTIONS ON ANTENNAS AND PROPAGATION* 53.12 (2005), pp. 3870–3876.

[118] P. Nikitin and K. Rao. "Theory and measurement of backscattering from RFID tags". In: *Antennas and Propagation Magazine, IEEE* 48.6 (2006), pp. 212–218. DOI: 10.1109/MAP.2006.323323.

[119] Y.-C. Shen. "Terahertz pulsed spectroscopy and imaging for pharmaceutical applications: A review". In: *International Journal of Pharmaceutics* 417.1–2 (2011). ¡ce:title¿Advanced characterization techniques¡/ce:title¿, pp. 48–60. DOI: 10.1016/j.ijpharm.2011.01.012.

[120] P. Taday, I. Bradley, D. Arnone, and M. Pepper. "Using terahertz pulse spectroscopy to study the crystalline structure of a drug: A case study of the polymorphs of ranitidine hydrochloride". In: *Journal of Pharmaceutical Sciences* 92.4 (2003), pp. 831–838. DOI: 10.1002/jps.10358.

[121] R. S. Singh, M. O. Culjat, J. Y. Suen, W. S. Grundfest, H. Lee, E. R. Brown, and Z. D. Taylor. "Reflective terahertz imaging of porcine skin burns". In: *Optics Letters* 22.11 (2008), pp. 1258–1260.

[122] B. E. Cole, V. P. Wallace, R. J. Pye, D. D. . Arnone, E. H. Linfield, R. M. Woodward, and M. Pepper. "Terahertz pulse imaging in reflection geometry of human skin cancer and skin tissue". In: *PHYSICS IN MEDICINE AND BIOLOGY* 47 (2002), pp. 3853–3863.

[123] V. Wallace, D. Arnone, E. Linfield, M. Pepper, and R. Woodward. "Terahertz Pulsed Imaging of Skin Cancer in the Time and Frequency Domain". In: *Journal of Biological Physics* 29 (2003), pp. 275–261.

[124] V. P. Wallace, R. J. Pye, B. E. Cole, D. D. Arnone, E. H. Linfield, M. Pepper, and R. M. Woodward. "Terahertz Pulse Imaging of ex vivo Basal Cell Carcinoma". In: *Journal of investigative Dermatology* 120 (2003), pp. 72–78.

[125] A. J. Fitzgerald et al. “Optical properties of tissue measured using terahertz pulsed imaging”. In: *Proceedings of SPIE: Medical Imaging 2003* 5030 (2003), pp. 459–470.

[126] J.-H. Son. “Terahertz electromagnetic interactions with biological matter and their applications”. In: *Journal of Applied Physics* 105.102033 (2009).

[127] B. E. Cole, A. J. Fitzgerald, E. Pickwell, M. Pepper, and V. P. Wallace. “Simulation of terahertz pulse propagation in biological systems”. In: *Applied Physics Letters* 84.12 (2004).

[128] B. E. Cole, A. J. Fitzgerald, M. Pepper, V. P. Wallace, and E. Pickwell. “In vivo study of human skin using pulsed terahertz radiation”. In: *PHYSICS IN MEDICINE AND BIOLOGY* 49 (2004), pp. 1595–1607.

[129] R. S. Singh et al. “THz Medical Imaging: in vivo Hydration Sensing”. In: *IEEE Transactions on Terahertz Science and Technology* 1.1 (2011), pp. 201–210.

[130] J. Wijmans and R. Baker. “The solution-diffusion model: a review”. In: *Journal of Membrane Science* 107.1–2 (1995), pp. 1–21. DOI: 10.1016/0376-7388(95)00102-I.

[131] T. Higuchi. “Physical chemical analysis of pecutaneous absorption process from creams and ointments”. In: *J. Soc. Cosmet. Chem.* 11 (1960), pp. 85–97.

[132] A. Boix, C. Peraire, R. Obach, and J. Domenech. “Estimation of Transdermal Permeation Parameters in Non-stationary Diffusion experiments”. In: *Pharm. Res.* 22 (2005), pp. 94–102.

[133] G. Maghraby, A. Williams, and B. Barry. “Skin hydratation and possible hunt route penetration in controlled estradiol delivery from ultradeformable and standard liposomes”. In: *J. Pharm. Pharmacol.* 53 (2001), pp. 1311–1322.

[134] K. Sato, K. Sugibayashi, and Y. Morimoto. “Effect and mode of action of aliphatic esters on the in vitro skin permeation of nicorandil”. In: *International Journal of Pharmaceutics* 43.1–2 (1988), pp. 31–40. DOI: http://dx.doi.org/10.1016/0378-5173(88)90055-5.

[135] J. L. Bowen and C. M. Heard. “Film drying and complexation effects in the simultaneous skin permeation of ketoprofen and propylene glycol from simple gel formulations”. In: *International Journal of Pharmaceutics* 307.2

(2006), pp. 251–257. DOI: http://dx.doi.org/10.1016/j.ijpharm.2005.10.014.

Related articles to the thesis

Published

- **Colossal Reduction of the Curie temperature due to finite-size effets in $CoFe_2O_4$ Nanoparticles**, Victor Lopez-Dominguez, Joan Manel Hernandez, Javier Tejada, Ron Ziolo, Chemistry of Materials (2012), Vol. 25, No.1, pp. 6-11.

- **Reply to Comment on "Colossal Reduction of the Curie temperature due to finite-size effets in $CoFe_2O_4$ Nanoparticles"**, Javier Tejada, Joan Manel Hernandez, Victor Lopez-Dominguez, Ron Ziolo, Chemistry of Materials (2012), Vol.21, No.0, pp. 2001-03.

Under Revision

- **Measurement of the permeation of topical excipients throught artificial membranes with non-invasive Terahertz time-domain system**, Victor Lopez-Dominguez, Antoni Boix, Albert Redo, Javier Tejada, Journal of Controlled Release.

- **Synthesis of Gold Nanoparticles/pPET3OC12-sqS composites and their application in hybrid solar cells**, A. de Leon, R. Flores, Ivana Moggio, A. Ponce, Victor Lopez-Dominguez, Javier Tejada, Ron Ziolo, In preparation.

- **Terahertz targgeting**, Victor Lopez-Dominguez, Javier Tejada, Albert Redo, IEE transactions, In Preparation.

Other articles

- **Goya's artwork imaging with Terahertz waves**, Cristina Seco, Victor Lopez-Dominguez, Gianliuca Arauz, Albert Redo, J. Palacios, Javier Tejada, Optic Express (2013), Vol.21, pp. 17800-05.

- **Microwave Spectrometry for the evaluation of the Structural Integrity of Metallic Stents**, Gianluca Arauz, Victor Lopez-Dominguez, Joan Manel Hernandez, Oriolm Rodriguez-Leor, Antoni Bayes-Genis, Juan M. O' Callaghan, Antoni Gracia-Santiago, Javier Tejada, Medical Physics (2014) Vol 41, No. 4, pp. 041902.
- **RF Monitoring of Commercial Vascular Stents with Dipole Scattering Resonances**, Gianluca Arauz, Victor Lopez-Dominguez, Joan Manel Hernandez Oriol Rodriguez-Leor, Antoni Bayes-Genis, J.M. Rius, Juan M. O'Callaghan, Antoni Garcia-Santiago, Javier Tejada, IMS 2014, Accepted.